TUM School of Engineering and Design

Theoretical Analysis on Applications of Near-field Acoustic Levitation: Positioning, Bearing, and Transportation Systems

Yuanyuan Liu

Vollständiger Abdruck der von der TUM School of Engineering and Design der Technischen Universität München zur Erlangung des akademischen Grades eines

Doktors der Ingenieurwissenschaften (Dr.-Ing.)

genehmigten Dissertation.

Vorsitz:	Prof. Dr.-Ing. Michael F. Zäh
Prüfer*innen der Dissertation:	Prof. Dr.-Ing. Steffen Marburg
	Prof. Su Zhao

Die Dissertation wurde am 13.12.2021 bei der Technischen Universität München eingereicht und durch die TUM School of Engineering and Design am 15.06.2022 angenommen.

大学之道，在明明德，在亲民，在止于至善。

——《大学》

The way of great learning consists in manifesting one's bright virtue, consists in loving the people, consists in stopping in perfect goodness.

——《Great Learning》

Abstract

Near-field acoustic levitation (NFAL) is a new suspension technique that has been rapidly developed recently. The positioning and transportation systems based on the NFAL have the benefits of compact structure, easy control, and without physical contacts. Therefore, these systems are able to handle and transfer the wafer or component of the microelectromechanical system in semiconductor manufacturing and micro-assembly. In addition, squeeze film bearings based on the NFAL have the advantages of frictionless, low maintenance cost, and high speed. However, there are still some problems existing in these applications, such as the levitation stability of the floating object and the dynamic performance of the squeeze film bearing. Moreover, the transportation system based on the NFAL is still not available for cylindrical objects. Therefore, to solve these problems, three applications of the NFAL are theoretically studied in this work, including positioning systems, squeeze film bearings, and contactless transportation systems. This work has two significant contributions. On the one hand, it provides the theoretical analysis foundation for these applications. On the other hand, the guidance for these applications is acquired to enhance their operating performance. The main research content and achievements are stated as follows.

First of all, this work presents an air lubrication theory-based numerical analysis for the positioning system to evaluate the restoring force. The film pressure distribution between the reflector and the radiator is governed by the Reynolds equation, which is calculated by the eight-point discrete method because of the film thickness discontinuity. In addition, an experimental setup for measuring the restoring force is constructed to validate the proposed theoretical model. The numerical results indicate that the restoring force is increasing with the increment of the eccentricity, which is consistent with the experimental results. In addition, numerical calculation results show that a greater restoring force is acquired in the larger radiator vibration amplitude or the heavier levitator, indicating the higher stability of the system.

Secondly, to study the running performances of the squeeze film bearing, this work presents an analytical model for a bearing with three separate pads and calculates its dynamic performance. The balance position of the rotor is determined by combining the steady Reynolds equation and the Newton-Raphson iteration method. Considering the variation of the film thickness caused by the continuous vibration of the bearing pads, a theoretical method is presented to obtain the bearing dynamic coefficients. The calculated results show excellent agreement with experimental results. The dynamic analysis results show that the direct dynamic coefficients increase with a decrement in the rotation speed of the rotor or with an increment in the vibration amplitude of the bearing pad.

In the last part of this work, a non-contact transportation system for cylindrical objects is designed based on the investigation of the stability mechanism in the positioning system. This transport performance is realized by engraving one groove on the concave surface of the Langevin transducer, which leads to an asymmetric pressure distribution. Therefore, a thrusting force arising from this asymmetric pressure field drives the horizontal movement of the levitator. The thrusting force is computed by the integration of the pressure gradient over the solving domain. The theoretical calculation results show that the greatest thrusting force is acquired by reasonably designing the depth and arc length of the groove. In addition, the thrusting force is increased by increasing the groove width, the radiator vibration amplitude or the levitator weight.

Acknowledgement

At first, I would like to express my deepest gratitude to my supervisor, Prof. Dr.-Ing. Steffen Marburg. Thanks for giving me an opportunity to work with you and offering me the possibility to work in a liberal environment. You are an experienced and insightful guider. Without your patient and careful guidance, this work would be hard for me to finish. It gives me a deep impression that we discussed my work via E-mail on the night, even at the weekend. Your help and guidance will be highly appreciated and remembered forever.

I sincerely thank Prof. Su Zhao for his interest in my work and his time and effort in reviewing my dissertation. I am grateful to Prof. Michael Zäh for chairing the board of examiners.

I would like to thank the China Scholarship Council (CSC) (File No. 201808340068) for providing the financial support to allow me to live and study in Germany.

I would like to thank all members of the Chair of Vibroacoustics of Vehicles and Machines at TUM. I had a really great time with you guys. Special thanks go to Dr.-Ing. Kian K. Sepahvand, Xiaodong Sun, Zhe Liu, Martin Eser, Sourav Chandra, Andreas Beinstingel, Bettina Chocholaty, and Dr.-Ing. Marcus Maeder for helping me correct the academic writing and giving me helpful suggestions about my research.

My appreciation goes to Prof. Kai Feng and Dr. Minghui Shi at State Key Laboratory of Advanced Design and Manufacturing for Vehicle Body, Hunan University, for their support on the measurement of the restoring force by experiment. Also, the author would like to thank Dr. Su Zhao, Professor at Ningbo Institute of Materials Technology and Engineering, Chinese Academy of Sciences, for providing the experimental data about the squeeze film journal bearing.

I am grateful to my girlfriend Tianai Zhang for her accompany and support. You have always been my relief during the toughest time.

Finally, I want to thank my parents. Without your constant love, support, understanding, and encouragement, I wouldn't have reached this goal.

谁言寸草心，报得三春晖，感谢我的父母给我无私的关爱，支持我走到今天。

Appended Publications

A Y. Y. Liu, M. H. Shi, K. Feng, K. K. Sepahvand, S. Marburg. Stabilizing near-field acoustic levitation: Investigation of non-linear restoring force generated by asymmetric gas squeeze film. *The Journal of the Acoustical Society of America* 148 (3), 2020, 1468-1477.

Author contribution statement:

Yuanyuan Liu: Conceptualization, Methodology, Investigation, Validation, Visualization, Data Curation, Writing – Original Draft. **Minghui Shi**: Methodology, Validation, Writing – Review & Editing. **Kai Feng:** Resources, Supervision. **Kian K. Sepahvand:** Supervision, Writing –review & editing. **Marburg Steffen:** Resources, Supervision, Writing –review & editing.

B Y. Y. Liu, X. D. Sun, K. K. Sepahvand, S. Marburg. Theoretical analysis on the static and dynamic performances of a squeeze film air journal bearing with three separate pads structure. *International Journal of Mechanical Sciences* 200, 2021, 106442.

Author contribution statement:

Yuanyuan Liu: Conceptualization, Methodology, Data curation, Validation, Writing – original draft. **Xiaodong Sun:** Methodology, Writing –review & editing. **Kian K. Sepahvand:** Supervision, Writing –review & editing. **Steffen Marburg:** Supervision, Writing –review & editing.

C Y. Y. Liu, M. Eser, X. D. Sun, K. K. Sepahvand, S. Marburg. Theoretical analysis of a contactless transportation system for cylindrical objects based on ultrasonic levitation. *The Journal of the Acoustical Society of America* 150 (3), 2021, 1682-1690.

Author contribution statement:

Yuanyuan Liu: Conceptualization, Methodology, Investigation, Validation, Visualization, Data Curation, Writing – Original Draft. **Martin Eser:** Investigation, Writing –review & editing. **Xiaodong Sun:** Methodology, Writing –review & editing. **Kian K. Sepahvand:** Supervision, Writing –review & editing. **Steffen Marburg:** Supervision, Writing –review & editing.

Publications not appended to this work

- Y.Y. Liu, K. K. Sepahvand, K. Feng, S. Marburg. Numerical analysis on transportation characteristics of a self-running sliding stage based on near-field acoustic levitation. Fortschritte der Akustik - DAGA : 45. Jahrestagung für Akustik, Rostock, Germany, 2019.
- Y. Y. Liu, M. H. Shi, K. K. Sepahvand, S. Marburg. Numerical analysis of the nonlinear restoring force based on near-field acoustic levitation. Proceedings of the 23rd International Congress on Acoustics, integrating 4th EAA Euroregio, DEGA, Aachen, Germany, 2019.
- Y.Y. Liu, K. K. Sepahvand, S. Marburg. Static performances study on a three-pad air journal bearing based on near-field acoustic levitation. Fortschritte der Akustik - DAGA : 46. Jahrestagung für Akustik, Hannover, Germany, 2020.
- Y.Y. Liu, K. K. Sepahvand, S. Marburg. Comparison of static characteristics between three and four-pad squeeze film air journal bearings. The 27th International Congress on Sound and Vibration, Prague, Czech, 2021.

List of Figures

List of Tables

Contents

Part I Summary and Overview

1 Introduction

Handling and transporting components of the microelectromechanical systems or semiconductors is difficult owing to their fragile and surface-sensitive nature [1]. Traditional contact handling and transport techniques, such as clamps [2] and conveyor belts [3], are not suitable [4]. This is because the mechanical contact will easily cause abrasion and scratches on the contact part. Then, the tiny particles produced by abrasion will also cause damage to the processing equipment. There is no physical contact between the manipulator and the component in the contactless levitation system. Consequently, these systems have the benefits of nearly no wear, no friction, and being environmentally friendly. In addition, they can achieve high resolution and motion accuracy by avoiding stick-slip effects [5]. Traditional non-contact levitation techniques mainly include magnetic levitation [6] and air cushions [7-9]. The magnetic levitation uses the magnetic force generated by the magnetic field to levitate the object. However, it produces a redundant magnetic field, which influences adjacent electric equipment. Further, the magnetic levitation system requires floating objects having an electromagnetic characteristic [10]. For the air cushion, the high-pressure air flows upwards through several holes and creates a repulsive levitation force. Yet, the air cushion is noisy and energy-intensive because it requires an extra air compressor to supply pressurized clean air [11].

Acoustic levitation is another contactless levitation technique that has been developed rapidly in recent years, which can be divided into standing wave acoustic levitation (SWAL) and near-field acoustic levitation (NFAL) [1, 4]. In the SWAL, small particles or small living animals can be levitated in the pressure node of a standing wave acoustic field between the radiator and the reflector [12-15]. Nevertheless, the NFAL uses suspension objectors as reflectors and generates a much greater levitation force than the SWAL, which allows it to support much heavier objects [16].

One of the first researchers who observed the NFAL was Whymark [17] in 1975. He found that a flat disc hovers above a piston running at a vibration frequency of 20 kHz. Since then, many researchers have investigated the mechanism of the NFAL and proposed different models to predict the levitation force. One method is to calculate the acoustic radiation pressure based on the acoustic theory to obtain the levitation force. The acoustic radiation pressure is the average forward pressure generated on an obstacle when an acoustic wave propagating in a fluid medium encounters the obstacle [18]. For example, based on the acoustic radiation pressure formulation deduced by Chu and Apfel [19], Hashimoto *et al.*[20, 21] found that the levitation force has a close relationship with the suspension height and the vibration amplitude. Zhao and Wallaschek [22] presented a mathematical model which considers the non-linear absorption effect to calculate the levitation force.

Another method treats the fluid film in the NFAL phenomenon as a squeeze film. The levitation force originates from the high-pressure fluid generated by the squeezing action [23, 24]. Based on the piston-like model, Nomura *et al.* [25] used MacCormack's finite-difference scheme to numerically solve the basic governing equations in fluid dynamics. They pointed out that the equation derived by Hashimoto *et al.*[20] overestimates the levitation force. The difference between these two observations was attributed to energy leakage in the peripheries of the levitated object [26]. Moreover, most researchers used the non-linear Reynolds equation to describe the NFAL phenomenon [27-30]. The analytical solution methods of the Reynolds equation were presented in Refs. [26] and [31]. The numerical solution method of the Reynolds equation is various, which mainly contains the Finite Difference Method (FDM) [10, 32, 33], the Eight-point Discrete Method (EDM) [27, 34], and the Finite Element Method (FEM) [35-37].

To improve the accuracy of the numerical result, several variables, such as air inertia [38-41], edge effect [42, 43], and roughness [44-46], were considered in the theoretical model. If the Reynolds number approaches 1, the inertia effect is significant and needs to be considered [47]. The edge effect occurs when air enters into the squeeze film. Consequently, the pressure near the film edge immediately becomes lower than the ambient pressure [48]. The edge effect can be neglected if the squeeze action is slow since the pressure change near the film edge is very tiny. The roughness should be considered when it has the same magnitude as the film thickness. However, in most cases, there is no need to consider these variables [10, 27, 49-51].

With the development of computational techniques, Computational Fluid Dynamics (CFD) commercial software was also applied to calculate the levitation force [52-54]. For example, Brunetière and Wodtke [55] used the *CFX package* [56] to build a squeeze film model. They chose the Finite Volume Method (FVM) to discretize and solve 3D conservation equations for the transient flow of compressible fluids.

Outline of this work

In section 1, the state of the art towards the three application fields of the NFAL, i.e., positioning system, squeeze film bearing (SFB), and contactless transportation system, is presented, followed by a summary that gives insight into the contributions of this work. In section 2, the governing equations for the different applications are discussed. Section 3 presents the applied methods, which include numerical and experimental methods. A summary of the appended publications is the content of section 4, and the results are then discussed among the available references in section 5. This work finishes with a conclusion in section 6. All the appended publications are found in the second part of this work.

1.1 State of the art

According to the nature of propagating vibration wave, it is divided into two types: traveling wave and standing wave [57]. Correspondingly, the NFAL is classified into the traveling wave-based NFAL and the standing wave-based NFAL. Furthermore, the application of the NFAL mainly includes positioning systems [58-62], squeeze film bearings (SFBs) [63-65], and contactless transportation systems [11, 66, 67]. In the traveling wave, there is energy propagating along the direction of the wave, resulting in horizontal motion or rotational motion of the levitator [51, 68, 69]. In the standing wave, there is on average no net propagation of energy. The positioning system and SFB mainly use the standing wave-based NFAL. The traveling wave-based NFAL and the standing wave-based NFAL are both applied in the contactless transportation system. The following subsection focuses on reviewing the state of the art with respect to these three application fields.

1.1.1 Positioning system

Although many researchers did a lot of work on the application of the NFAL [70-74], there are still two important weaknesses that restrict its industrial applications. One is the magnitude of the load-carrying capacity, and the other is the levitation stability of the floating object. In order to enhance the load-carrying capacity, there are four methods available. The most direct method is using multiple transducers, as seen in Refs. [67, 75]. However, this method has the drawback of reducing the stability of the levitation system. Li *et al.* [27] tried to introduce another method. They added grooves on the bottom surface of the reflector to increase the load-carrying capacity. According to the results of the experiment and numerical calculation, the circumferential grooves have a positive effect on the load-carrying capacity, whereas the radial grooves have a negative effect. The third method is increasing the vibration amplitude by reasonably designing the transducer, e. g. geometry [76-78] and material [79-83]. The fourth method couples the NFAL with other no-contact levitation technology. For example, based on Ref. [68], Liu *et al.* [84] proposed a non-contact transportation system that added the aerostatic suspension into the NFAL system to transport heavy load objects.

The stability of the suspending object is affected by many factors in the positioning system based on the NFAL. For example, surface roughness can affect the airflow around the suspending object and slightly change the sound field between the radiating surface and the suspending object [4]. Moreover, manufacturing and installation errors also can generate an acoustic viscous force that influences the stability of the suspending object. In the NFAL, two approaches are usually utilized to produce an acoustic viscous force [85, 86]. The first approach is to use the traveling wave acoustic field between the radiator and the suspending object [11, 87], which is applied in the traveling wave-based NFAL. The second approach is to use the gradient of the fluid pressure distribution [66], which is mainly applied in the standing wave-based NFAL.

For a suspending object in the positioning system, experimental results revealed that its stability highly depends on the vibration amplitude and the vibration distribution of the radiating surface [16]. Ueha *et al.* [67] also proved this conclusion. They found that the Tshaped cross-section of a vibration plate guarantees more stable transportation than a uniform cross-section plate. Based on the near-boundary acoustic flow theory, Koike *et al.* [58] employed the block-spring model to estimate the stability of the suspending object and the acoustic viscous forces in both directions. Based on the block-spring model, Hu *et al.* [85] took the influence of acoustic flow outside the boundary layer into account when computing the acoustic viscous force. Kim and Ih [88] used the time-averaged acoustic potential around the levitated object to predict its moving direction and wobbling frequency. In the case of small floating objects, Yoshimoto *et al.* [89] used the CFD method to study the restoring force produced by a radiating surface vibrating at ultrasonic frequencies. Later, Li *et al.* [90] indicated that the block-spring model could only handle small amplitude oscillation due to its linear assumption. They employed the acoustic radiation potential method and the Stokes micro-continuum theory to obtain the restoring force.

1.1.2 Squeeze film bearing

With the development of rotating machinery, the demands on high accuracy and high rotation speed for bearings have increased [91]. Hence, air-lubricated bearings are developed to meet these demands. Owing to the low viscosity of air, these bearings have the benefits of ultra-high speed, low heat emission, and low cost [92-94]. Moreover, their oil-free feature avoids pollution caused by liquids such that makes them environmentally friendly [95, 96]. These properties enable their usage in turbo-compressors, inertial gyroscopes, and turbochargers, etc [97-100]. In general, aerodynamic, aerostatic, and squeeze effects are used to produce a high-pressure air film in an air bearing [101]. In the case of pure aerodynamic bearings [102-104], friction and wear occur between the rotor and the bearing during start-up and shutdown because the aerodynamic effect does not operate at a low speed [105]. This problem can be addressed by using aerostatic bearings [106-108] since they provide an additional force at a low rotation speed to counterbalance the weight of the rotor. Nevertheless, aerostatic bearings need an extra air compressor to supply high-pressure air, which makes the bearing noisy and costly. Consequently, SFBs have been developed to satisfy the demands of low friction and high accuracy by introducing the NFAL technique into the air-lubricated bearing. This is because the NFAL has some inherent benefits, such as the compact structure and no material restriction of the levitator [4, 67].

The SFB is a type of hybrid air film bearing. In the case that the rotation speed is zero, the rotor is supported by the levitation force produced by the pure squeeze effect [109-111]. At a given rotation speed, the air film pressure is simultaneously affected by the squeeze effect and the aerodynamic effect [112]. Since Salbu [23] proposed the SFB models in 1964, the research of the SFB has attracted much awareness [113-115]. For example, Ha *et al.* [116] presented a united SFB with three piezoelectric plates and elastic hinges. They numerically and experimentally investigated the effect of the excitation frequency and the vibrating amplitude on the load-carrying capacity of the bearing. However, this study only took the squeeze effect into consideration and ignored the aerodynamic effect. Following this, some different SFB constructions, such as the three-lobe [117], the flexure pivot-tilting pad bearings [118], and the tubular [119], have been designed. Stolarski *et al.* [120] examined the load-carry capacity of three SFBs with different configurations. The experimental results indicate that the configuration of the bearing has a significant influence on its working performance. In addition, the operating mode [121], mounting location [118], and material [122, 123] of the bearing are extra factors that influence its load-carrying capacity. Nevertheless, a common drawback of these bearings [116-123] is the low load-carrying capacity.

In the study of the NFAL, the load-carrying capacity is increased with increasing the vibration amplitude of the structure [124, 125]. The vibration amplitude generated by the Langevin ultrasonic transducer is higher than that generated by the piezoelectric plate [116-123]. This is because the Langevin transducer has high input power and excellent electroacoustic transformation efficiency [126]. Therefore, Zhao *et al.* [126, 127] presented a new active contactless journal bearing that uses three Langevin transducers to constitute the construction of the bearing. Two advantages can be observed in this structure. Firstly, it has a greater load-carrying capacity (more than 51 N) than the above-mentioned bearings (maximum 5 N) [116-123] which use the piezoelectric plate as the vibration source. Secondly, the vibration of each Langevin transducer can be controlled individually, making it possible to adjust the position of the rotor. Nevertheless, this research [127] did not investigate the static and dynamic characteristics of the bearing, which is significant for the application and design of this type of SFB.

Many researchers have investigated the static characteristic of SFBs [116, 118, 128]. To study the dynamic characteristic of SFBs, many researchers employed the orbit simulation method [129-133]. For example, Stolarski [134] numerically and experimentally studied the motion trajectory of a rotor at a low rotation speed based on the SFB model introduced by Ha *et al.* [116]. The results indicate that the squeeze effect not only increases the bearing capacity but also improves the critical speed of the bearing. Moreover, the results also show that the bearing stability is enhanced by the increment of the external load. Feng *et al.* [135] discovered similar results through theoretical calculation. Furthermore, they indicated that for heavy external loads, the squeeze effect has less influence on the threshold speed of the rotor-bearing system. Stolarski and Miyatake [136] reported that the SFB with flexible configuration exhibits better performance according to the experimental results. Compared to other analytical methods, the orbit simulation method has higher computational costs since it is performed by coupling the fluid governing equations and the motion equations of the rotor [134]. For instance, Beck and Strodtman [137] applied numerical and variational methods to study the stability of SFBs. Yet, their theoretical model only considered one freedom degree.

Furthermore, in air-lubricated bearings, a group of stiffness and damping coefficients is used to investigate the bearing dynamic performances [138-141]. Calculation of dynamic coefficients and their application to compute the critical speed and unbalance response are based on the hypotheses of linearized bearing forces [138, 142]. The major difference between the SFBs and other kinds of air bearings [143-145] is that the structure of the SFBs vibrates continuously in a steady state. Therefore, it is necessary to consider the variation of the pressure and film thickness distributions of the SFBs caused by the vibration of the structure.

1.1.3 Contactless transportation system

In the NFAL-based transportation system, the acoustic viscous force is used to drive the motion of the levitator. As mentioned in subsection 1.1.1, the generation mechanisms of the acoustic viscous force are different for the two types of NFAL [85]. In the traveling wave-based NFAL, the acoustic viscous force arises from the traveling wave acoustic field between the radiator and the suspending object. For example, Hashimoto *et al.* [68] utilized two Langevin transducers to stimulate the traveling wave along a vibrating plate. A small thin plate was successfully transported by using this system. Hereafter, based on this system, other researchers investigated its transportation performances [51, 146] or extended its application range [147, 148]. Li *et al.* [149] investigated the effect of the grooves engraved on the bottom surface of the levitator on transportation performance. They found that the direction of the groove length perpendicular to the propagation direction of the rail's vibration waves can achieve better levitation and transport performance. These traveling wave-based transportation systems [51, 68, 146-149] have the same feature, i.e., they need a guide rail to generate a traveling wave vibration. On the contrary, Koyama *et al.* [11] designed a self-running transport platform that generates its own traveling wave vibration. This platform not only generates self-suspension but also produces a thrusting force that propels forward motion.

In the standing wave-based NFAL, the acoustic viscous force originates from the gradient of the fluid pressure distribution produced by the asymmetrical standing wave acoustic field. For example, Hu *et al.* [66] utilized a wedge-shaped stator to produce a standing wave vibration pattern. Due to the uneven distribution of the stator vibration amplitude along its length direction, the levitator can be propelled along the horizontal direction. Based on this study, Hu *et al.* [150] proposed a board-shaped stator with triangular grooves to construct a transport system to meet the long-distance non-contact transportation requirement. However, these two transportation systems [66, 150] only have a single source of vibration, which cannot guarantee a uniform moving speed of the levitator. This is because the vibration amplitude varies along the length direction of the stator. Wei *et al.* [151] utilized two longitudinal vibration transducers to construct a standing wave-based transportation system. The pressure gradient exists in two non-parallel squeeze films generated by these two transducers. Similar to Ref. [11], Chen *et al.* [152] introduced a self-suspending and self-moving vibrator based on the standing wave-based NFAL. The coupled resonant vibration of this actuator is used to produce an asymmetrical standing wave acoustic field. Based on this vibrator, Yang *et al.* [153] analyzed its levitation and driving performances and proposed a closed-loop system to control its motion trajectory. Aono *et al.* [154] found that if the levitator was inserted between two opposing vibration transducers, the restoring force of the system will increase. In this way, this method can be applied to standing wave-based transportation systems to obtain a high thrusting force. However, the load capacity of the system will be weakened since one of the levitation forces is in the same direction as gravity. Thus, this system is only appropriate for suspending light objects.

Another kind of contactless transportation system based on the standing wave-based NFAL is proposed by Hashimoto *et al.* [155]. They added a conventional pulse motor actuator to move the entire suspension system. This system cannot be called a standing wave-based transportation system because the driving force is not produced by the squeeze film. The above-mentioned transportation systems [11, 51, 66, 68, 146-152, 155] are only available for objects with planar surfaces, whereas some components in the industry have cylindrical surfaces [156, 157].

1.2 Contribution of this work

The main application fields of the NFAL are positioning systems, squeeze film bearings, and contactless transportation systems. The contribution of this work is to present the corresponding numerical methods to study the working performance of these applications. The following questions are raised based on the scientific state of the art and the author's previous work [10, 27, 118]:

1. If the floating object is misaligned with the radiator, how can the pressure distribution representing the airflow in the squeeze film be determined?
2. How to obtain the dynamic coefficients of the squeeze film journal bearings used to study its dynamic characteristic?
3. How to transport the precision component with the cylindrical surfaces using the NFAL?

These three questions are answered by the three publications appended to this dissertation, respectively. In Publication A, the generation mechanism of the instability phenomenon for the positioning system is revealed. Publication B discussed the static and dynamic characteristics of the SFBs. In Publication C, the NFAL-based non-contact transportation system for the cylindrical objects is presented.

Publication A

If the centers of the reflector and the radiator are not concentric, the area of the radiator is divided into an overlapping area and a remaining area. The remaining area is also referred to as the no-squeeze domain because there is no squeeze effect. Since the film thickness in the no-squeeze domain is infinite, this domain can be considered as grooved to guarantee that the film thickness can be expressed in the whole solution domain. The pressure distribution is acquired by solving the Reynolds equation in a cylindrical coordinate system. The shear stress acting on the bottom surface of the reflector originates from the asymmetrical fluid pressure profile, which is integrated as a restoring force. Moreover, an experimental setup is built for the measurement of the restoring force. The numerical results of the restoring force match well with the experimental results at various eccentricities.

Publication B

For a squeeze film bearing which consists of three Langevin ultrasonic transducers, an analytical model is proposed. Each Langevin transducer is simplified to a pad with the same vibration characteristics in this model. The pressure distribution is expressed by the steady-state dimensionless Reynolds equation that takes into account both the squeeze and aerodynamic effects. Therefore, the bearing forces are calculated by the integration of the pressure over the whole bearing inner surface. The Newton-Raphson iteration method is applied to determine the attitude angle in steady conditions. Based on the calculated static performance, the film pressure and thickness are modified by using the infinitesimal perturbation method. Combining the static results with the dynamic Reynolds equation that takes into account the perturbation motion of the rotor, the eight dynamic coefficients are obtained. The proposed calculation methods are verified by comparing the numerical results with experimental data.

Publication C

Based on the research results of Publication A, it is known that an asymmetrical pressure distribution will be produced due to the existence of the groove. Based on the air lubrication theory, a thrusting force is generated from the asymmetrical pressure field. In Publication B, the levitation force is produced from the squeeze air film between the rotor and the Langevin transducer. Therefore, both the thrusting force and the levitation force will be generated by engraving a groove on the cylindrical concave of the Langevin transducer. In this way, a contactless transportation system using the NFAL can be designed to transport cylindrical objects. In order to meet the long-distance transportation and transporting heavy object requirements, multiple modified Langevin transducers are utilized in this transportation system.

2 Governing Equations

This section is dedicated to the presentation of the governing equations used in the three application fields, namely positioning systems, SFBs, and contactless transportation systems. At first, the Reynolds equation describing the pressure distribution of the squeeze film is presented. The boundary conditions have a great effect on the accuracy of the calculation results of the Reynolds equation. In addition, the film thickness is a key parameter to solve the Reynolds equation. Therefore, the boundary conditions and expression of the film thickness are subsequently discussed. Notably, the Reynolds equation, boundary conditions, and film thickness are discussed separately in the different application fields. Moreover, the main parameters of each analytical model and its operating conditions are also given.

2.1 Positioning system

In the case that the reflector is eccentric relative to the radiator, the analytical model of the NFAL in the cylindrical coordinate system is presented in Figure 1. The radiuses of the radiator and the reflector are the same and are defined as L. The centers of the radiator and the reflector are represented by O and O_1, respectively. The component of the distance between O and O_1 in the r-direction is defined as eccentricity e. When the center of the reflector coincides with the center of the radiator, the reflector is stable in the r-direction [27]. Otherwise, the reflector will exhibit a damped oscillation until it achieves a balance position. However, if the eccentricity is too large, the reflector will fall directly. Notably, this model neglects the effect of the inclination of the reflector since the eccentricity is small [85, 90].

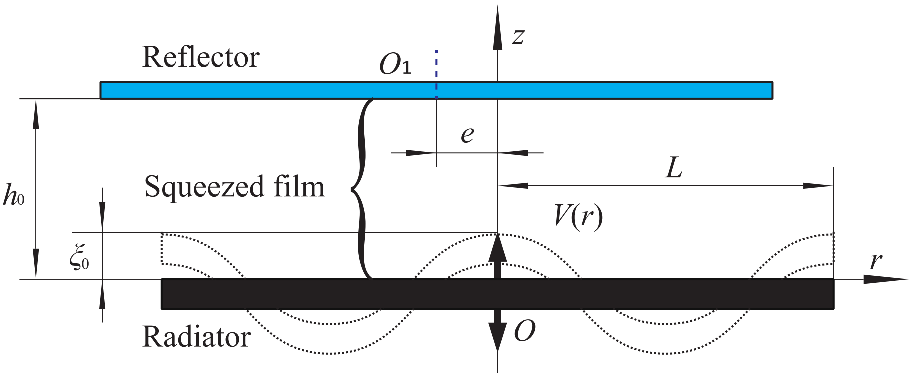

Figure 1: Misaligned squeeze film model in the cylindrical coordinate, see Publication A.

2.1.1 Reynolds equation

The Reynolds equation is based on the Navier-Stokes equations and the continuity equation

[94], which was formulated by Osborne Reynolds [158]. Several assumptions are adopted here to simplify the Navier-Stokes momentum equations, as

a. The fluid is air in this work, which is compressible;

b. The air is a Newtonian fluid, and the airflow is treated as laminar flow;

c. This work neglects the pressure gradient in the direction of the film thickness [51];

d. The squeeze film is considered to be isothermal because of the small film thickness [159];

e. This work neglects the air inertia force and body force [59];

f. No relative slip at the interface, which means the fluid velocity on the surface is the same as the surface velocity [160].

Notably, assumption (c) is reasonable when the film thickness (most of the cases in the level of microns) is much smaller than the film width and length (typically in the level of millimeters). However, if the film thickness is in the same order of magnitude as the film width or length, the pressure gradient in the direction of the film thickness cannot be neglected [161]. Additionally, the expression of the Reynolds equation is varied for different application fields, where the details will be introduced in the corresponding analytical models.

Based on the above-mentioned assumptions (a-e), the Navier-Stokes momentum equations in the *θ*- and *r*-directions are simplified as [162]

$$\rho\left(\frac{\partial v_\theta}{\partial t}\right)=-\frac{1}{r}\frac{\partial p}{\partial \theta}+\mu_a\frac{\partial^2 v_\theta}{\partial z^2}, \tag{2.1}$$

$$\rho\left(\frac{\partial v_r}{\partial t}\right)=-\frac{\partial p}{\partial r}+\mu_a\frac{\partial^2 v_r}{\partial z^2}, \tag{2.2}$$

where v_θ and v_r are the airflow velocity in the *θ*- and *r*-directions, respectively. The air pressure and air density in the squeeze film are p and ρ, respectively. The dynamic air viscosity is expressed by μ_a. Referring to assumption (f) and Refs. [51, 163], the corresponding velocity expressions in the *θ*- and *r*-directions are represented as

$$v_\theta=\frac{z}{2\mu_a r}\frac{\partial p}{\partial \theta}(z-h)+\dot{\varphi}\frac{zr}{h}+\ddot{\varphi}\frac{\rho z r}{6\mu_a h}\left(z^2-h^2\right), \tag{2.3}$$

$$v_r=\frac{z}{2\mu_a}\frac{\partial p}{\partial r}(z-h)+\dot{u}\frac{z}{h}+\ddot{u}\frac{\rho z}{6\mu_a h}\left(z^2-h^2\right), \tag{2.4}$$

in which φ and u are relative rotation in radian and relative horizontal displacement of the reflector, respectively. The film thickness is $h=h(r,\theta,t)$. Integration of the continuity equation over the whole film thickness yields [94]

$$\int_0^h \left[\frac{\partial \rho}{\partial t} + \frac{\partial \left(r \rho v_r \right)}{r \cdot \partial r} + \frac{\partial \left(\rho v_\theta \right)}{r \cdot \partial \theta} + \frac{\partial \left(\rho v_z \right)}{\partial z} \right] dz = 0 \, , \tag{2.5}$$

in which v_z is the airflow velocity in the z-direction. According to above-mentioned assumption (c), v_z equals zero. Substituting the airflow velocities expressed by equations (2.3) and (2.4) into equation (2.5), a dimensionless Reynolds equation in the cylindrical coordinate can be stated as

$$\begin{aligned} \frac{\partial}{\partial R}\left(RPH^3 \frac{\partial P}{\partial R} \right) + \frac{1}{R} \cdot \frac{\partial}{\partial \theta}\left(PH^3 \frac{\partial P}{\partial \theta} \right) &= \sigma R \cdot \frac{\partial \left(PH \right)}{\partial T} + \Lambda_1 \dot{U} \frac{\partial \left(RPH \right)}{\partial R} \\ &+ \Lambda_1 \dot{\varphi} \frac{\partial \left(RPH \right)}{\partial \theta} + \Lambda_2 \ddot{U} \frac{\partial \left(RP\Lambda_1 H^3 \right)}{\partial R} + \Lambda_2 \ddot{\varphi} \frac{\partial \left(RP\Lambda_1 H^3 \right)}{\partial \theta} \, , \end{aligned} \tag{2.6}$$

here, $\sigma = 12 \mu_a \omega L^2 / p_a h_0^{\ 2}$, $\Lambda_1 = 6 \mu_a L^2 / p_a h_0^{\ 2}$ and $\Lambda_2 = -\rho_a L^2 / 2 p_a$. The squeeze number is known as σ, which represents the squeeze film pressure produced by the periodic vibration of the radiator. The mean film thickness and the dimensionless relative horizontal displacement are h_0 and U, respectively. The normalized parameters are expressed as

$$R = r / L \, , \; P = p / p_a \, , \; H = h / h_0 \, , \; T = \omega \cdot t \, , \; U = u / L \, , \text{ and } \Lambda_1 = \rho / \rho_a \, ,$$

where p_a and ρ_a are surrounding air pressure and air density, respectively. The frequency and angular frequency of the vibration are expressed by f and $\omega = 2\pi f$, respectively.

2.1.2 Boundary conditions and film thickness

Boundary conditions are essential to solve the non-linear Reynolds equation. For the NFAL, the squeeze film has not yet been generated at the initial moment. Thus, the film pressure equals the surrounding air pressure, and the film thickness is zero, as follows

$$P \,|_{T=0} = 1, \quad H \,|_{T=0} = 0 \, . \tag{2.7}$$

The film pressure and thickness are periodic functions in the time domain when the squeeze system achieves a steady state, which means [134, 164]

$$P \,|_T = P \,|_{T+2\pi} \, , \quad H \,|_T = H \,|_{T+2\pi} \, . \tag{2.8}$$

Apart from the above-mentioned initial boundary conditions (equation (2.7)) and periodic boundary conditions (equation (2.8)), there are also contact boundary conditions. The pressure on the boundary of the squeeze film is equal to the environmental pressure because of the continuity of the pressure at the interface with the surrounding air.

The schematic diagram of the positioning system is shown in Figure 2. The pressure on the boundary Γ_r equals the ambient air pressure, which means

$$P|_{\Gamma_r(R=1)}=1\,. \tag{2.9}$$

In addition, the pressure gradient at the center O is zero, which represents

$$\frac{\partial P}{\partial R}(R=0,T)=0\,. \tag{2.10}$$

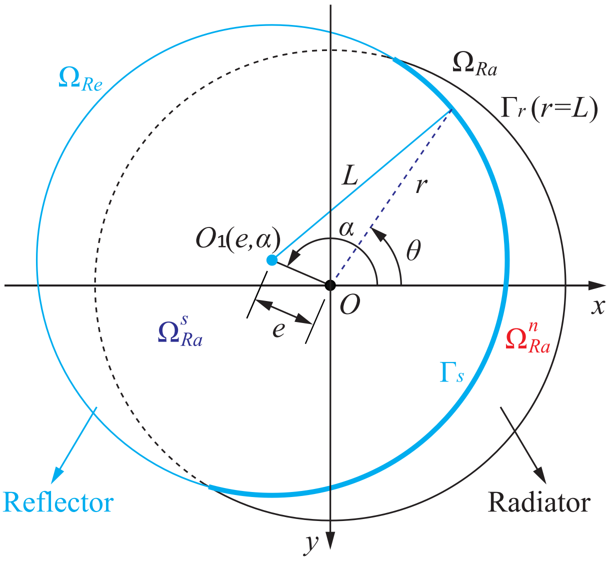

Figure 2: Schematic diagram of the boundary conditions for the positioning system, see Publication A.

In the piston-like model of the NFAL [21], the film thickness only considers the levitation height of the floating object. This is because the vibrating plate has great rigidity in the longitudinal direction. Therefore, its deformation is assumed to be uniform. In most cases, especially for thin plates, the deformation of the vibrating plate has the same order of magnitude as the film thickness. Therefore, the vibration amplitude distribution of the plate should be taken into account in the expression of the film thickness [49].

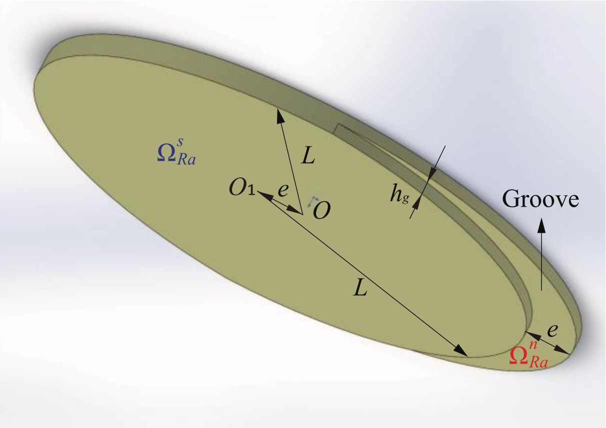

Figure 3: The imaginary reflector with groove, see Publication A.

In Figure 2, the solution domain Ω_{Ra} is equivalent to the area of the radiator. The area of the reflector is represented by Ω_{Re}. The overlapping area Ω_{Ra}^{s} ($\Omega_{Ra}^{s} = \Omega_{Ra} \cap \Omega_{\mathrm{Re}}$) is stated as the squeeze domain. The remaining area of the radiator is stated as the no-squeeze domain Ω_{Ra}^{n}. In order to guarantee that the height of the squeeze film can be expressed in the solution domain, the no-squeeze domain Ω_{Ra}^{n} is assumed to be grooved, as shown in Figure 3. The depth of the groove is denoted as h_g. Thus, the dimensionless thickness of the squeeze film is written as

$$H = \begin{cases} 1 + \dfrac{\xi_0 \cdot V(r) \cdot sin(T)}{h_0} & (r, \theta) \subseteq \Omega_{Ra}^{s} \\ 1 + \dfrac{\left[\xi_0 \cdot V(r) \cdot sin(T) + h_g\right]}{h_0} & (r, \theta) \subseteq \Omega_{Ra}^{n} \end{cases}, \tag{2.11}$$

where $V(r)$ and ξ_0 represent the normalized mode shape and the maximum vibration amplitude of the radiator, respectively, as shown in Figure 1. In order to acquire the pressure distribution, the main parameters of the positioning system and its operating conditions are listed in Table 1.

Parameter	Value	Unit
Radius L	60	mm
Excitation frequency f	19	kHz
Weight of the reflector plate	0.9244	N
Vibration amplitudes ξ_0	16.9	μm
Air temperature	20	°C
Air density ρ_a	1.204	kg/m^3
Air dynamic viscosity μ_a	1.81×10^{-5}	Pa·s
Ambient air pressure p_a	1.013×10^{5}	Pa
Air kinematic viscosity v_a	1.51×10^{-5}	m^2/s

Table 1: Main parameters of the positioning system and its operating conditions.

2.2 Squeeze film bearing

The schematic diagram of the SFB proposed by Zhao *et al.* [126, 127] is shown in Figure 4. Three Langevin ultrasonic transducers compose this bearing. The bearing inner face includes three concave radiation surfaces. When an alternating voltage of the frequency *f* is applied, four piezoelectric plates vibrate at the same frequency along the thickness direction. Due to the squeeze effect, the squeeze film is generated between the outer surface of the rotor and the concave surfaces of the bearing. As a result, the levitation force originating from the squeeze film is produced to keep the rotor suspended.

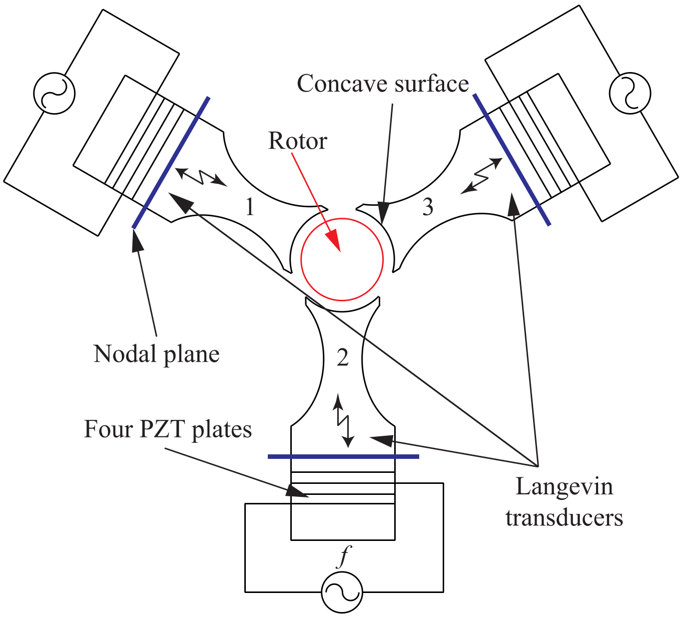

Figure 4: Schematic diagram of the SFB [127].

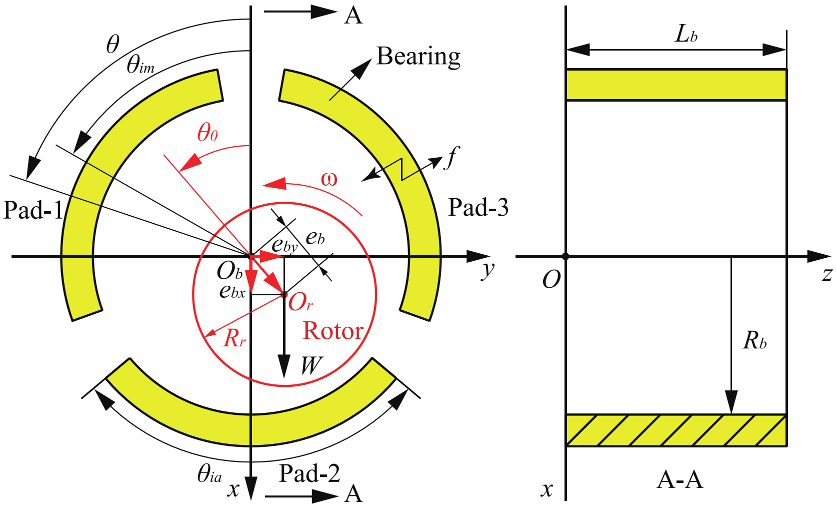

Figure 5: Simplified analysis model of the bearing and coordinate systems, see Publication B.

In order to analyze the running characteristics of this SFB, the analytical model of the bearing shown in Figure 5 is presented. Each Langevin ultrasonic transducer is simplified to a pad with the same vibration behavior. Two assumptions are adopted in this analytical model: (I) due to the high tilting and radial stiffnesses of the Langevin transducer, the squeeze film pressure does not influence the movement of the pad; (II) each pad has a uniform radial vibration amplitude distribution over the entire pad area. The center points of the bearing and the rotor are O_b and O_r, respectively. The bearing inner radius and the outer radius of the rotor are defined as R_b and R_r, respectively. The nominal clearance of the bearing is expressed as $c = R_b - R_r$. The width of the bearing is L_b. The eccentricity displacement e_b is the distance between O_b and O_r, which has two components e_{by} and e_{bx} in the *y*- and *x*-directions, respectively. The attitude angle θ_0 is defined by the angle between the direction of static external load and the connection line between the bearing and rotor centers. The static external load W may come from the magnetic force or the weight of the rotor, etc. The rotor is treated as perfectly balanced and rigid.

2.2.1 Reynolds equation

Based on the assumptions (a-e) as shown in subsection 2.1.1, taking into account both the squeeze and aerodynamic effects, the expression of the steady-state dimensionless Reynolds equation is written as [134, 135]

$$\frac{\partial}{\partial \theta}\left(PH^3\frac{\partial P}{\partial \theta}\right)+\frac{\partial}{\partial Z}\left(PH^3\frac{\partial P}{\partial Z}\right)=\Lambda_b\frac{\partial(PH)}{\partial \theta}+\sigma_b\frac{\partial(PH)}{\partial T}, \tag{2.12}$$

where $Z = z / R_b$ is the normalized position in the *z*-direction. The normalized film thickness is $H = h / c$. The normalized time T and film pressure P are mentioned in subsection 2.1.1. The rotation speed of the rotor is denoted as n. The bearing number Λ_b represents the aerodynamic pressure produced by the rotor rotating at an angular velocity $\omega_n = 2\pi \cdot n / 60$, which is given by

$$\Lambda_b = \frac{6\mu_a\omega_n}{p_a}\left(\frac{R_b}{c}\right)^2. \tag{2.13}$$

The squeeze number σ_b is given by

$$\sigma_b = \frac{12\mu_a\omega}{p_a}\left(\frac{R_b}{c}\right)^2. \tag{2.14}$$

2.2.2 Boundary conditions and film thickness

In Figure 5, the contact boundary conditions are defined by

$$P(\theta, z = 0 \,\&\, L_b) = 1,\ P(\theta_{im} \pm \theta_{ia} / 2, z)_{|(i=1,2,3)} = 1, \tag{2.15}$$

where θ_{im} and θ_{ia} represent the middle angle and arc length of the i^{th} pad, respectively. The initial and periodic boundary conditions are described by equations (2.7) and (2.8), respectively.

In Figure 5, the film thickness between the bearing inner face and the rotor outer face is determined by three components: eccentricity e_b, the nominal clearance c, and the radial displacement due to the vibration of the bearing. Consequently, the dimensionless thickness of the squeeze film is represented by

$$H = 1 + \frac{e_{by} \cdot \sin(\theta) + e_{bx} \cdot \cos(\theta) + \xi_i \cdot V_i(\theta, z) \cdot \sin(T)}{c}, \tag{2.16}$$

where $V_i(\theta, z)$ and ξ_i are the normalized mode shape and the maximum vibration amplitude for the i^{th} pad. According to the assumption (II) mentioned in subsection 2.2.1 that the entire pad area has a uniform radial amplitude, the normalized mode shape $V_i(\theta, z)$ in this work is therefore equal to 1. The basic parameters of the SFB are listed in Table 2. The air material properties are shown in Table 1.

Parameters	Value	Unit
Rotor radius R_r	24.97	mm
Bearing bore radius R_b	25	mm
Bearing nominal clearance c	30	µm
Bearing width L_b	25	mm
Pad number i	1,2,3	
Pad arc length θ_{ia}	100°; 100°; 100°	
Pad middle angle θ_{im}	60°; 180°; 300°	
Pad vibration amplitudes $\xi_i\,(i=1,2,3)$	15	µm
Excitation frequency f	20	kHz
Static external load W	40	N

Table 2: The basic parameters of the SFB.

2.3 Contactless transportation system

For a smooth concave surface as shown in Figure 4, there is a symmetric pressure distribution between the rotor and the pad in the axial direction. However, the symmetry of the film pressure distribution is destroyed by the introduction of a groove on the radiator, as shown in Figure 6. The groove width, groove depth, and groove arc length are represented by l_g, h_{gt}, and θ_g, respectively. Based on the air lubrication theory, the thrusting force F_t is generated by the asymmetrical pressure distribution. Therefore, this structure not only produces the levitation force F_l, but also produces a thrusting force that drives the horizontal movement of the levitator.

By using multiple Langevin transducers as shown in Figure 6, a contactless transportation system based on the NFAL for cylindrical objects is presented in Figure 7. This transportation system has two distinct benefits. The first is the increment of the load-carrying capacity. The second is to satisfy the requirement for long-distance transportation.

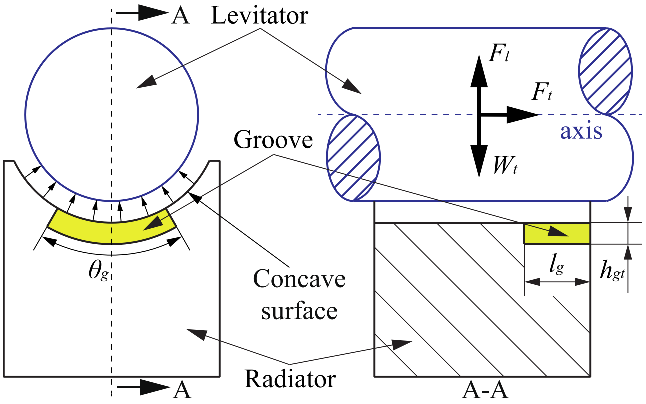

Figure 6: Schematic diagram of the engraved groove on the radiator, see Publication C.

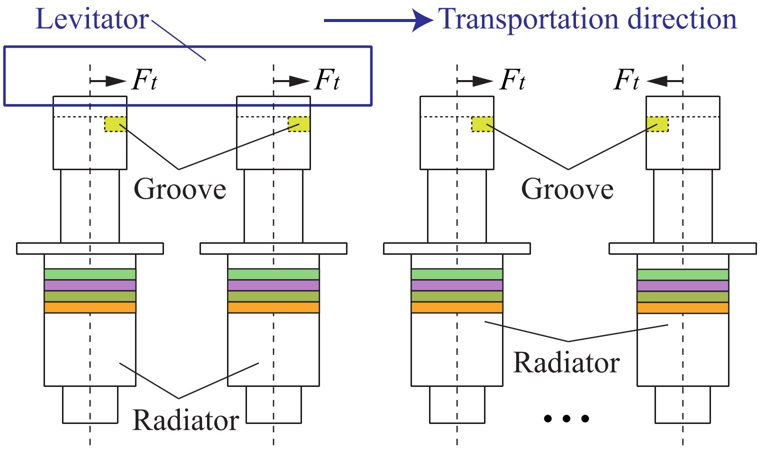

Figure 7: Schematic configuration of the contactless transportation system, see Publication C.

The analytical model for one radiator is shown in Figure 8. The center points of the radiator and the rotor are O_t and O_l, respectively. The radiator inner radius and the levitator outer radius are defined as R_t and R_l, respectively. The nominal clearance of the system is expressed as $c_t = R_t - R_l$. The width of the radiator is L_t. Since the squeeze film is symmetrical in the θ-direction and there is no other force to drive the levitator rotation, the levitator will not rotate. Therefore, the aerodynamic effect is ignored, and only the squeeze effect works in the squeeze film. Hence, center points O_t and O_l are situated on the *x*-axis. The distance between O_t and O_l is called the eccentricity e_t. As shown in Figure 7, the levitator is simultaneously supported by several radiators. Therefore, the inclination of the levitator is ignored. The levitator displacement in the transportation direction relative to its initial position is defined as u_t. In addition, the levitator is supposed to be perfectly balanced and a rigid body.

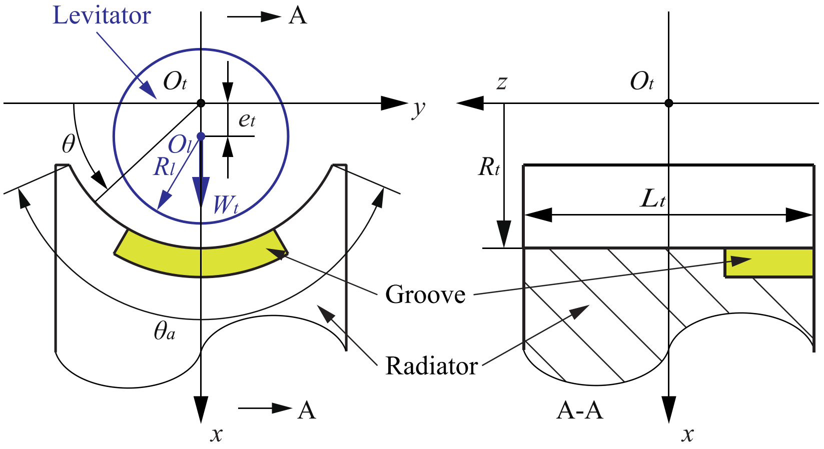

Figure 8: Analytical model for one radiator and corresponding coordinate systems, see Publication C.

2.3.1 Reynolds equation

Based on the research of subsections 2.1.1 and 2.2.1, the expression for the dimensionless Reynolds equation taking into account the motion of the levitator in the transportation direction is expressed as

$$\frac{\partial}{\partial \theta}\left(PH^3\frac{\partial P}{\partial \theta}\right)+\frac{\partial}{\partial Z}\left(PH^3\frac{\partial P}{\partial Z}\right)=\sigma_t\frac{\partial(PH)}{\partial T}+\Lambda_t\frac{\partial(PH)}{\partial Z}-\alpha_t\frac{\partial\left(P^2H^3\right)}{\partial Z}. \tag{2.17}$$

The coefficients $\Lambda_t = 6\mu_a \dot{u}_t R_t / p_a c_t^2$ and $\alpha_t = \rho_a \ddot{u}_t R_t / 2p_a$ represent the influence of the speed of the levitator movement $\dot{u}_t$ and its acceleration $\ddot{u}_t$ on the pressure value. The squeeze number is

$$\sigma_t = \frac{12\mu_a \omega R_t^2}{p_a c_t^2}. \tag{2.18}$$

The normalized film thickness and width position are $H = h / c_t$ and $Z = z / R_t$, respectively. The normalized film pressure P and time T are described in subsection 2.1.1.

2.3.2 Boundary conditions and film thickness

As shown in Figure 8, the contact boundary conditions are

$$P\left(\theta, z=\pm L_t/2\right)=1,\ P\left(\theta=\pi/2\pm\theta_a/2, z\right)=1, \tag{2.19}$$

in which θ_a is the radiator arc length. The initial and periodic boundary conditions are expressed by equations (2.7) and (2.8), respectively.

In Figure 8, the radial vibration amplitude of the radiator is assumed to be uniform [165]. Therefore, the normalized mode shape $V_t\left(\theta, z\right)$ equals 1. Referring to Figures 6 and 8, the groove domain includes the right ($\theta=\pi/2+\theta_g/2$), the left ($\theta=\pi/2-\theta_g/2$), the front ($z=-L_t/2$), and the rear ($z=-L/2+l_g$) boundaries. Therefore, the dimensionless film thickness is stated as

$$H=\begin{cases}1+\dfrac{\xi_t\cdot V_t\left(\theta,z\right)\cdot\sin\left(T\right)+h_{gt}-e_t\cdot\sin\left(\theta\right)}{c_t} & \left(\text{groove domain}\right)\\ 1+\dfrac{\xi_t\cdot V_t\left(\theta,z\right)\cdot\sin\left(T\right)-e_t\cdot\sin\left(\theta\right)}{c_t} & \left(\text{remaining domain}\right)\end{cases}, \tag{2.20}$$

where ξ_t represents the maximum vibration amplitude of the radiator. The basic design parameters of the radiator are listed in Table 3. The air material properties are described in Table 1.

Parameter	Value	Unit
Levitator outer radius R_l	9.96	mm
Radiator concave radius R_t	10 mm	mm
Nominal clearance c_t	40	µm
Radiator width L_t	20	mm
Radiator arc length θ_a	120	°
Groove depth h_{gt}	1	mm
Groove width l_g	3	mm
Groove arc length θ_g	80	°
Vibration frequency f	20	kHz
Weight of the levitator W_t	0.5	N
Vibration amplitude ξ_t	9	µm

Table 3: The basic design parameters of the radiator.

3 Applied Methods

This section describes the methods used in this work. By using numerical methods to solve the non-linear Reynolds equation, the pressure distribution in the squeeze film is obtained. Next, the squeeze film forces are computed by the integration of the pressure or the pressure gradient. In addition, the solution method for the dynamic coefficients of the squeeze film bearing and the experimental measurement method of the restoring force are presented, respectively.

3.1 Numerical methods

Since the Reynolds equation is a second-order non-linear differential equation, it is usually solved by numerical methods. The utilized numerical methods in this work are introduced in the following subsections.

3.1.1 Finite difference method

In fluid lubrication calculations, the finite difference method (FDM) is frequently applied to solve the Reynolds equation [160]. In order to solve equation (2.12), a two-dimensional mesh grid is adopted for the FDM, as shown in Figure 9. The pressure gradient of a node can be expressed by the pressure of the adjacent four nodes, namely

$$\begin{aligned} \frac{\partial P}{\partial \theta} &= \frac{P_{i+1,j}-P_{i-1,j}}{2\Delta\theta}, \quad \frac{\partial^2 P}{\partial \theta^2} = \frac{P_{i+1,j}+P_{i-1,j}-2P_{i,j}}{(\Delta\theta)^2} \\ \frac{\partial P}{\partial z} &= \frac{P_{i,j+1}-P_{i,j-1}}{2\Delta z}, \quad \frac{\partial^2 P}{\partial z^2} = \frac{P_{i,j+1}+P_{i,j-1}-2P_{i,j}}{(\Delta z)^2} \end{aligned} . \tag{3.1}$$

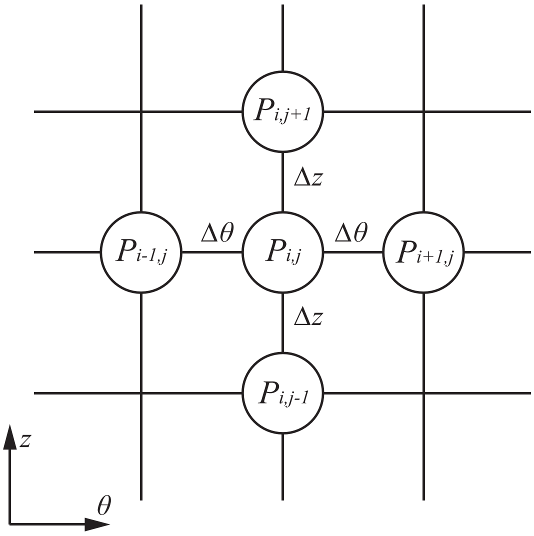

Figure 9: The detailed two-dimensional mesh grid for the FDM [160].

By substituting equation (3.1) into equation (2.12), a non-linear difference equation that represents the relationship between the film thickness and the pressure over time can be expressed as [32]

$$f_{i,j}\left(P_{i-1,j},P_{i,j},P_{i+1,j},P_{i,j-1},P_{i,j+1},H,T\right)=0\,. \tag{3.2}$$

3.1.2 Eight-point discrete method

Owing to the existence of the groove, as shown in Figure 8, the film thickness is discontinuous at the boundaries of the groove domain. Consequently, the partial differentials $\left(\partial H/\partial\theta\right)_{i,j}$ and $\left(\partial H/\partial Z\right)_{i,j}$ in equation (2.17) are unsolvable. In this case, the above-mentioned FDM is not a suitable solution method. Hence, the eight-point discrete method (EDM) is applied here to handle the problem of the discontinuous film thickness [34]. The detailed two-dimensional mesh grid for the EDM is illustrated in Figure 10. The node $G_{i,j}$ is surrounded by the area Ω_{ij}, which is surrounded by the four blue dashed lines $\Gamma_{ij,1\text{-}4}$. The adjacent eight points $N_{ij,1-8}$ are averagely positioned on the four dashed lines $\Gamma_{ij,1\text{-}4}$.

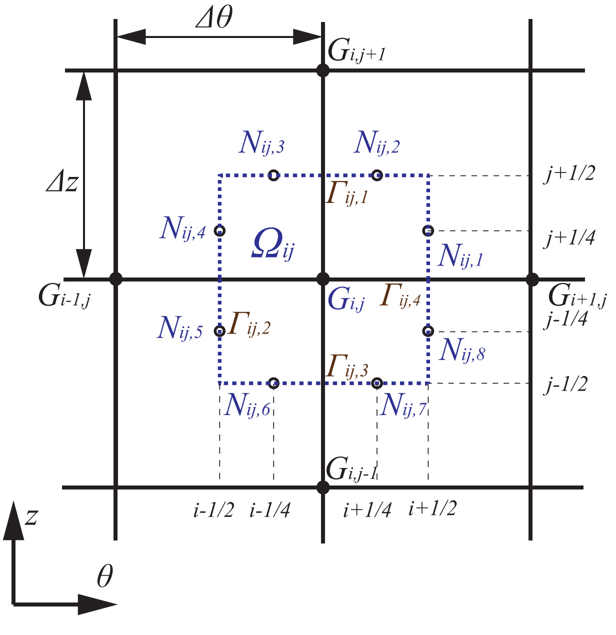

Figure 10: The detailed two-dimensional mesh grid for the EDM, see Publication C.

By integrating equation (2.17) over area Ω_{ij}, the dimensionless rate of fluid flow passing through Ω_{ij} is expressed as

$$\begin{aligned}&\iint_{\Omega_{ij}}\left\{\frac{\partial}{\partial\theta}\left(PH^3\frac{\partial P}{\partial\theta}\right)+\frac{\partial}{\partial Z}\left[PH^3\frac{\partial P}{\partial Z}\right]\right\}d\theta dZ\\&=\iint_{\Omega_{ij}}\left[\sigma_t\frac{\partial(PH)}{\partial T}\right]d\theta dZ+\iint_{\Omega_{ij}}\left[\Lambda_t\frac{\partial(PH)}{\partial Z}-\alpha_t\frac{\partial\left(P^2H^3\right)}{\partial Z}\right]d\theta dZ\end{aligned}\ . \tag{3.3}$$

By using Green's theorem, the surface integration of the left-hand side and the second term on the right-hand side of equation (3.3) are equal to an enclosed line integration, as follows

$$\begin{aligned}&\oint_{\Gamma_{ij}}\left[-\left(PH^3\frac{\partial P}{\partial Z}\right)d\theta+\left(PH^3\frac{\partial P}{\partial\theta}\right)dZ\right]\\&=\iint_{\Omega_{ij}}\left[\sigma_t\frac{\partial(PH)}{\partial T}\right]d\theta dZ+\oint_{\Gamma_{ij}}\left[\alpha_t\partial\left(P^2H^3\right)-\Lambda_t\partial(PH)\right]d\theta\end{aligned}\ . \tag{3.4}$$

The direction of line integration is counterclockwise, i.e., from $\mathit{\Gamma}_{ij,1}$ to $\mathit{\Gamma}_{ij,4}$. For the first term on the left-hand side of equation (3.4), since the projections of $\mathit{\Gamma}_{ij,2}$ and $\mathit{\Gamma}_{ij,4}$ on the θ-axis equal zero, the line integrations along $\mathit{\Gamma}_{ij,2}$ and $\mathit{\Gamma}_{ij,4}$ equal zero as well. Therefore, equation (3.4) is simplified to

$$\oint_{\Gamma_{ij}}-\left(PH^3\frac{\partial P}{\partial Z}\right)d\theta=-\int_{\Gamma_{ij,1}}\left(PH^3\frac{\partial P}{\partial Z}\right)d\theta-\int_{\Gamma_{ij,3}}\left(PH^3\frac{\partial P}{\partial Z}\right)d\theta\,. \tag{3.5}$$

The mean film thickness of two points located on the same dashed line is used to replace the corresponding line film thickness [34], such as

$$H^3\left(\mathit{\Gamma}_{ij,1}\right)=\left(H^3_{i-1/4,j+1/2}+H^3_{i+1/4,j+1/2}\right)/\,2\,. \tag{3.6}$$

Subsequently, the trapezoidal rule and the central difference method are used to expand equation (3.5), which can be expressed as

$$\begin{aligned}&-\int_{\Gamma_{ij,1}}\left(PH^3\frac{\partial P}{\partial Z}\right)d\theta-\int_{\Gamma_{ij,3}}\left(PH^3\frac{\partial P}{\partial Z}\right)d\theta\\&=(P_{i,j}+P_{i,j+1})(P_{i,j+1}-P_{i,j})\left(H^3_{i-1/4,j+1/2}+H^3_{i+1/4,j+1/2}\right)\frac{\Delta\theta}{4\Delta Z}\\&-(P_{i,j}+P_{i,j-1})(P_{i,j}-P_{i,j-1})\left(H^3_{i-1/4,j-1/2}+H^3_{i+1/4,j-1/2}\right)\frac{\Delta\theta}{4\Delta Z}\end{aligned}\ . \tag{3.7}$$

All the terms in equation (3.4) can be decomposed in the same format as equation (3.7). Thus, the non-linear Reynolds equation (2.17) can be substituted by equation (3.2).

The details of using the EDM to solve the Reynolds equation for the positioning system are described in Ref. [27].

3.1.3 Newton-Raphson method

The Newton–Raphson method is used to linearize the aforementioned difference equation

(3.2) [166-168], which is expressed as

$$\begin{aligned} & f_{i,j}^{(n)} + \frac{\partial f_{i,j}^{(n)}}{\partial P_{i-1,j}} \left(P_{i-1,j}^{(n+1)} - P_{i-1,j}^{(n)} \right) \\ & + \frac{\partial f_{i,j}^{(n)}}{\partial P_{i,j}} \left(P_{i,j}^{(n+1)} - P_{i,j}^{(n)} \right) + \frac{\partial f_{i,j}^{(n)}}{\partial P_{i+1,j}} \left(P_{i+1,j}^{(n+1)} - P_{i+1,j}^{(n)} \right) \\ & + \frac{\partial f_{i,j}^{(n)}}{\partial P_{i,j-1}} \left(P_{i,j-1}^{(n+1)} - P_{i,j-1}^{(n)} \right) + \frac{\partial f_{i,j}^{(n)}}{\partial P_{i,j+1}} \left(P_{i,j+1}^{(n+1)} - P_{i,j+1}^{(n)} \right) = 0 \end{aligned} \quad . \tag{3.8}$$

After solving equation (3.8), the pressure profile in the squeeze film is acquired. Therefore, the squeeze film forces originating from the pressure field are computed in the next section 3.2.

3.2 Squeeze film forces

Generally, the NFAL generates two types of squeeze film forces. The first is the levitation force due to the difference between the mean film pressure and the environmental pressure. The second is the shear stress due to the pressure gradient. The forces obtained by integrating the shear stresses are called the restoring force and the thrusting force in the positioning system and the contactless transportation system, respectively.

3.2.1 Restoring force

As shown in Figure 2, the pressure distribution of the positioning system is calculated in the cylindrical coordinate system with origin O (denoted by $O - r\theta z$). Subsequently, the shear stresses obtained in the system $O\text{-}r\theta z$ are decomposed into the system $O_1 - r_1\theta_1 z$, as shown in Figure 11. Therefore, the mean restoring forces in the x-direction $\bar{F}_{rx}$ and in the y-direction $\bar{F}_{ry}$ are calculated by averaging the restoring force in one period, which are expressed by

$$\begin{bmatrix} \bar{F}_{rx} \\ \bar{F}_{ry} \end{bmatrix} = \frac{1}{2\pi} \int_0^{2\pi} \int_0^{2\pi} \int_0^{L} \begin{bmatrix} -\tau_{z\theta} \cos(\theta_1) & -\tau_{zr} \cos(\theta_1) \\ \tau_{z\theta} \sin(\theta_1) & \tau_{zr} \sin(\theta_1) \end{bmatrix} \cdot \begin{bmatrix} \sin(\theta - \theta_1) \\ \cos(\theta - \theta_1) \end{bmatrix} \cdot r dr d\theta dT \, . \tag{3.9}$$

The total restoring force $\bar{F}_r = \sqrt{\bar{F}_{rx}^{\,2} + \bar{F}_{ry}^{\,2}}$ is computed with the two components $\bar{F}_{rx}$ and $\bar{F}_{ry}$. The angle θ_1 is expressed by

$$\theta_1 = \theta - \arcsin\left[e \cdot \sin(\alpha - \theta) / r_1 \right], \ \theta \subseteq [0, 2\pi] \, . \tag{3.10}$$

And the distance r_1 between N and O_1 is written as

$$r_1 = \sqrt{r^2 + e^2 - 2re\cos(\alpha - \theta)}, \ \ \theta \subseteq [0, 2\pi] \, . \tag{3.11}$$

For a Newtonian fluid, according to assumption (c), the shear stresses in the cylindrical coordinate is defined by [169]

$$\tau_{zj} = \mu_a \left(\frac{\partial v_z}{\partial j} + \frac{\partial v_j}{\partial z} \right) \cong \mu_a \frac{\partial v_j}{\partial z} \quad \left(j = r, \theta \right). \tag{3.12}$$

Substituting equations (2.3) and (2.4) into equation (3.12) yields the expression of the shear stresses $\tau_{z\theta}$ and τ_{zr}, which are stated as

$$\tau_{z\theta} \big|_{(z=h)} = \mu_a \frac{\partial v_\theta}{\partial z} \big|_{(z=h)} = \frac{h}{2r} \frac{\partial p}{\partial \theta} + \mu_a \frac{\dot{\varphi} r}{h} + \frac{\rho h \ddot{\varphi} r}{3}, \tag{3.13}$$

$$\tau_{zr} \big|_{(z=h)} = \mu_a \frac{\partial v_r}{\partial z} \big|_{(z=h)} = \frac{h}{2} \frac{\partial p}{\partial r} + \mu_a \frac{\dot{u}}{h} + \frac{\rho h \ddot{u}}{3}. \tag{3.14}$$

It is observed that the restoring force is mainly influenced by the pressure gradient, the film thickness, and the reflector motion in the horizontal and circumferential directions. The mean levitation force $\bar{F}_z$ is determined by integrating the pressure in the whole area of the radiator surface in one period, which is written as

$$\bar{F}_z = \frac{1}{2\pi} \int_0^{2\pi} \int_0^{2\pi} \int_0^{L} (p - p_a) \cdot r dr d\theta dT. \tag{3.15}$$

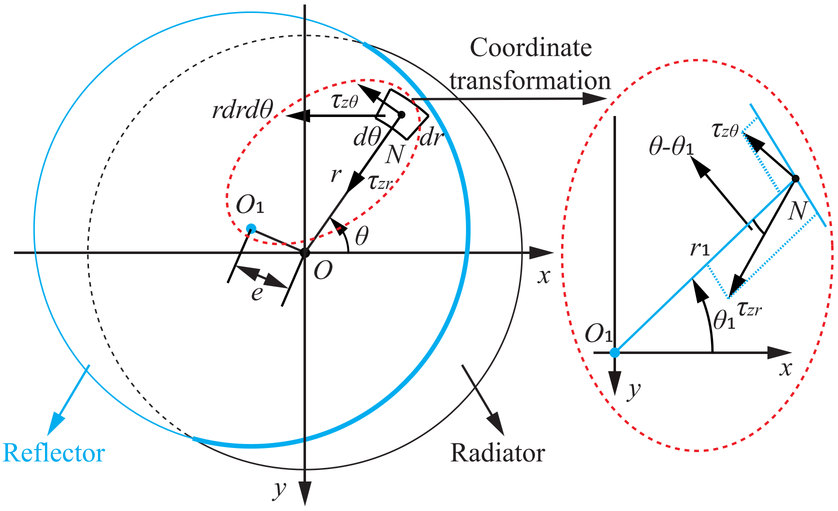

Figure 11: Geometric diagram for the resolution and composition of shear stresses, see Publication A.

3.2.2 Bearing forces

The bearing forces are the integral of the film pressure in the inner surface of the bearing [139]. As shown in Figure 5, the pressure distribution is calculated in a cylindrical coordinate system. Therefore, the mean bearing forces of the SFB in the Cartesian coordinate system are expressed by

$$\bar{F}_{by} = \frac{1}{2\pi}\sum_{i=1}^{3}\int_{0}^{2\pi}\int_{0}^{L_b}\int_{\theta_{im}-\theta_{ia}/2}^{\theta_{im}+\theta_{ia}/2}\left(p-p_a\right)\cdot\sin\left(\theta\right)d\theta dz dT\,, \tag{3.16}$$

$$\bar{F}_{bx} = \frac{1}{2\pi}\sum_{i=1}^{3}\int_{0}^{2\pi}\int_{0}^{L_b}\int_{\theta_{im}-\theta_{ia}/2}^{\theta_{im}+\theta_{ia}/2}\left(p-p_a\right)\cdot\cos\left(\theta\right)d\theta dz dT\,, \tag{3.17}$$

$$\bar{F}_{b} = \sqrt{\bar{F}_{bx}^{\ 2} + \bar{F}_{by}^{\ 2}}\,, \tag{3.18}$$

where $\bar{F}_{by}$ and $\bar{F}_{bx}$ are the components of the mean bearing force $\bar{F}_b$ in the y- and x-directions, respectively.

3.2.3 Thrusting force

In the analytical model of one radiator shown in Figure 8, based on the research of subsections 3.2.1 and 3.2.2, the mean thrusting force $\bar{F}_t$ and the mean levitation force $\bar{F}_l$ are expressed as

$$\begin{bmatrix}\bar{F}_t\\ \bar{F}_l\end{bmatrix} = \frac{1}{2\pi}\int_{0}^{2\pi}\int_{\pi/2-\theta_a/2}^{\pi/2+\theta_a/2}\int_{-L_t/2}^{L_t/2}\begin{bmatrix}\dfrac{h}{2}\dfrac{\partial p}{\partial z}+\mu_a\dfrac{\dot{u}_t}{h}+\dfrac{\rho_a h\ddot{u}_t}{3}\\ \left(p-p_a\right)\sin\left(\theta\right)\end{bmatrix}dz d\theta dT\,. \tag{3.19}$$

In the steady-state squeeze film, the value of the mean thrusting force $\bar{F}_t$ is equal to the value of the levitator weight W_t. In addition, it is observed that the mean thrusting force $\bar{F}_t$ has a close relationship with the film thickness h, the pressure gradient $\partial p/\partial z$, movement speed $\dot{u}_t$ and acceleration $\ddot{u}_t$ of the levitator.

3.3 Bearing attitude angle and dynamic coefficients

For the SFB model shown in Figure 5, in the steady condition, the mean vertical bearing force $\bar{F}_{bx}$ counterbalances the static external load W, and the mean horizontal bearing force $\bar{F}_{by}$ is equal to zero, which are expressed by

$$\bar{F}_{bx} = W,\ \bar{F}_{by} = 0,\ \arctan\left(\bar{F}_{by}/\bar{F}_{bx}\right) = 0,\ \theta_0 = \arctan\left(e_{by}/e_{bx}\right). \tag{3.20}$$

An error factor is given by

$$d\theta_0^k = \arctan\left(\bar{F}_{by}/\bar{F}_{bx}\right), \tag{3.21}$$

where k denotes the iteration numbers. Furthermore, the Newton-Raphson iteration method is adopted to update the attitude angle [170], which is described as

$$\theta_0^{k+1} = \theta_0^k - \frac{d\theta_0^k}{\left(d\theta_0^k - d\theta_0^{k-1}\right)}\left(\theta_0^k - \theta_0^{k-1}\right). \tag{3.22}$$

A flowchart of the static performance calculation program is shown in Figure 12. When the error $\left|d\theta_0^k\right|$ is less than or equal to the convergence threshold $\Delta\theta_0$, the calculation ends and θ_0^k is regarded as the attitude angle θ_0. In this work, $\Delta\theta_0$ is set to 1.7×10^{-3} rad. In the case where the value of the mean bearing force is not equal to the value of the external and the deviation is up to 0.1 N, a correction factor δe is applied to modify the eccentricity. The correction factor is given in this work as $0.001c$.

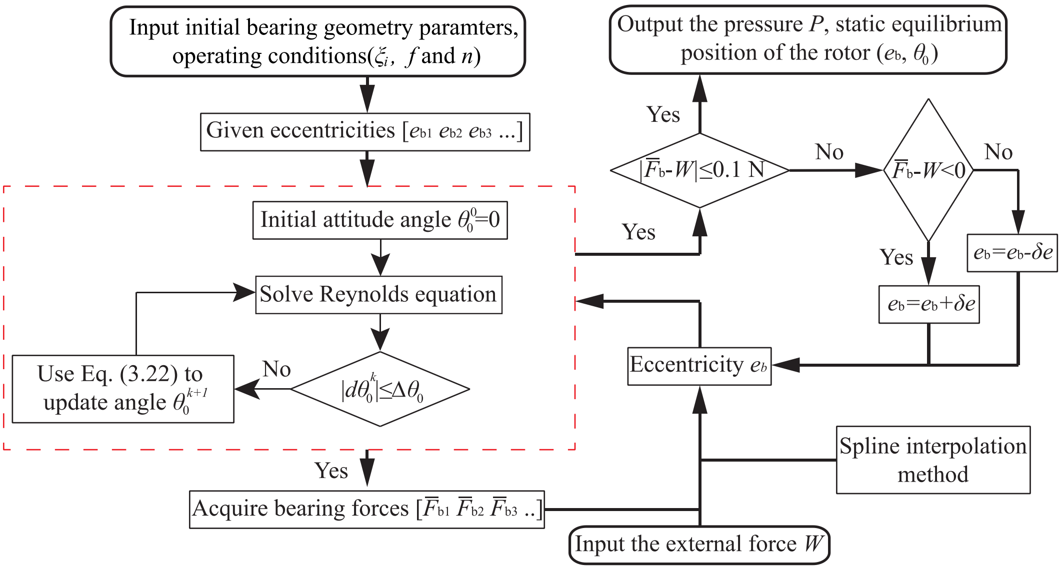

Figure 12: Flowchart of the static performance calculation, see Publication B.

After the static performance of the SFB is determined, the next step is to calculate its dynamic performance. Several different methods such as the Finite Volume Method (FVM) [171], the finite perturbation method [172], and the infinitesimal perturbation method [139] can be used to calculate the bearing stiffness and damping coefficients. Many studies have employed the infinitesimal perturbation method as the calculation method [173-176]. This method supposes that the infinitesimal displacement perturbations (Δx, Δy) and velocity perturbations ($\Delta\dot{x}$, $\Delta\dot{y}$) are applied to the rotor in the balance position. Thus, the modified normalized film pressure $\bar{P}$ and thickness $\bar{H}$ are expressed as [177]

$$\bar{P} = P_0 + \Delta P = P_0 + P_x\Delta X + P_y\Delta Y + P_{\dot{x}}\Delta\dot{X} + P_{\dot{y}}\Delta\dot{Y}\,, \tag{3.23}$$

$$\bar{H} = H_0 + \Delta H = H_0 + \Delta X\cos\left(\theta\right) + \Delta Y\sin\left(\theta\right), \tag{3.24}$$

where P_0 and H_0 represents the normalized film pressure and thickness in the balance position, respectively. The static calculation process shown in Figure 12 is used to obtain P_0 and H_0. The normalized perturbation variables are defined as $\Delta X = \Delta x / c$, $\Delta Y = \Delta y / c$, $\Delta\dot{X} = \Delta\dot{x} / c$, and $\Delta\dot{Y} = \Delta\dot{y} / c$. The normalized perturbation pressures P_x, P_y, $P_{\dot{x}}$ and $P_{\dot{y}}$ originate from the perturbation variables Δx, Δy, $\Delta\dot{x}$ and $\Delta\dot{y}$, respectively. In the infinitesimal perturbation method, the rotor orbits at a whirl angular velocity υ relative to the balance position. The dimensionless dynamic Reynolds equation taking into account the perturbation motion of the rotor is expressed as

$$\frac{\partial}{\partial\theta}\left(\bar{P}\bar{H}^3\frac{\partial\bar{P}}{\partial\theta}\right)+\frac{\partial}{\partial Z}\left(\bar{P}\bar{H}^3\frac{\partial\bar{P}}{\partial Z}\right)=\Lambda_b\frac{\partial\left(\bar{P}\bar{H}\right)}{\partial\theta}+2\Lambda_b\gamma\frac{\partial\left(\bar{P}\bar{H}\right)}{\partial\bar{t}}, \tag{3.25}$$

in which $\bar{t}=\upsilon t$ is the dimensionless time. In this work, it is assumed that the whirl frequency and the rotation frequency have the same value, which represents the ratio $\gamma=\upsilon/\omega$ equals 1. The normalized film pressure P_0 and thickness H_0 are periodic functions of frequency f over time. Since the bearing excitation frequency f (greater than 20 kHz) is significantly higher than the whirl frequency (1 kHz equals 60 krpm), the change rates of the film pressure and thickness with the dimensionless time $\bar{t}$ are approximately zero, which means $\partial P_0/\partial\bar{t}\approx 0$ and $\partial H_0/\partial\bar{t}\approx 0$. However, if f and the whirl frequency have the same order of magnitude, this approximation is not reasonable.

Substituting equations (3.23) and (3.24) into equation (3.25), and then collecting the terms with the same coefficients gives a group of differential equations as

$$\frac{\partial}{\partial\theta}\left(P_0H_0^3\frac{\partial P_\zeta}{\partial\theta}\right)+\frac{\partial}{\partial\theta}\left(P_\zeta H_0^3\frac{\partial P_0}{\partial\theta}\right)+\frac{\partial}{\partial Z}\left(P_0H_0^3\frac{\partial P_\zeta}{\partial Z}\right)+\frac{\partial}{\partial Z}\left(P_\zeta H_0^3\frac{\partial P_0}{\partial Z}\right)$$

$$\begin{aligned}&=\Lambda_b\frac{\partial P_xH_0+\partial P_0\cos\theta}{\partial\theta}-2\Lambda_b\gamma P_{\dot{x}}H_0\\&-\frac{\partial}{\partial\theta}\left(3P_0H_0^2\cos\theta\frac{\partial P_0}{\partial\theta}\right)-\frac{\partial}{\partial Z}\left(3P_0H_0^2\cos\theta\frac{\partial P_0}{\partial Z}\right)\quad \zeta=x\end{aligned}, \tag{3.26}$$

$$=\Lambda_b\frac{\partial P_{\dot{x}}H_0}{\partial\theta}+2\Lambda_b\gamma\left(P_0\cos\theta+P_xH_0\right)\qquad \zeta=\dot{x}, \tag{3.27}$$

$$\begin{aligned}&=\Lambda_b\frac{\partial P_yH_0+\partial P_0\sin\theta}{\partial\theta}-2\Lambda_b\gamma P_{\dot{y}}H_0\\&-\frac{\partial}{\partial\theta}\left(3P_0H_0^2\sin\theta\frac{\partial P_0}{\partial\theta}\right)-\frac{\partial}{\partial Z}\left(3P_0H_0^2\sin\theta\frac{\partial P_0}{\partial Z}\right)\quad \zeta=y\end{aligned}, \tag{3.28}$$

$$=\Lambda_b\frac{\partial P_{\dot{y}}H_0}{\partial\theta}+2\Lambda_b\gamma\left(P_0\sin\theta+P_yH_0\right)\qquad \zeta=\dot{y}. \tag{3.29}$$

The boundary conditions are stated as

$$P_x=P_y=P_{\dot{x}}=P_{\dot{y}}=0\qquad \text{at}\, z=0\,\&\,L_b, \tag{3.30}$$

$$P_x=P_y=P_{\dot{x}}=P_{\dot{y}}=0\qquad \text{at}\,\theta=\theta_{im}\pm\theta_{ia}/2\left(i=1,2,3\right). \tag{3.31}$$

The dimensionless perturbation pressures P_x and $P_{\dot{x}}$ are obtained by solving equations (3.26) and (3.27) simultaneously. Similarly, equations (3.28) and (3.29) are used to obtain P_y and $P_{\dot{y}}$. It is noted that the dimensionless perturbation pressures are periodic functions of time. Therefore, the mean stiffness and damping coefficients of the bearing in one period are calculated by

$$\begin{bmatrix} K_{xx} & K_{xy} \\ K_{yx} & K_{yy} \end{bmatrix} = \sum_{i=1}^{3} \frac{1}{2\pi} \int_0^{2\pi} \int_0^{L/R} \int_{\theta_{im}-\theta_{ia}/2}^{\theta_{im}+\theta_{ia}/2} \begin{bmatrix} P_x \cos\theta & P_y \cos\theta \\ -P_x \sin\theta & -P_y \sin\theta \end{bmatrix} \frac{P_a R^2}{c} d\theta dZ dT , \qquad (3.32)$$

$$\begin{bmatrix} C_{xx} & C_{xy} \\ C_{yx} & C_{yy} \end{bmatrix} = \sum_{i=1}^{3} \frac{1}{2\pi} \int_0^{2\pi} \int_0^{L/R} \int_{\theta_{im}-\theta_{ia}/2}^{\theta_{im}+\theta_{ia}/2} \begin{bmatrix} P_{\dot{x}} \cos\theta & P_{\dot{y}} \cos\theta \\ -P_{\dot{x}} \sin\theta & -P_{\dot{y}} \sin\theta \end{bmatrix} \frac{P_a R^2}{c\omega} d\theta dZ dT . \qquad (3.33)$$

3.4 Experimental measurement system of restoring force

The restoring force is usually in the order of milli-Newton (mN) therefore several methods exist to measure the small force [85]. For example, References [178-180] use a measurement system that mainly consists of voice coil motors (VCM), optical displacement sensors, and a proportional–integral–derivative (PID) controller to measure the restoring force. This measurement system has the advantage of excellent precision and repetitiveness. Nevertheless, it is also pretty complex.

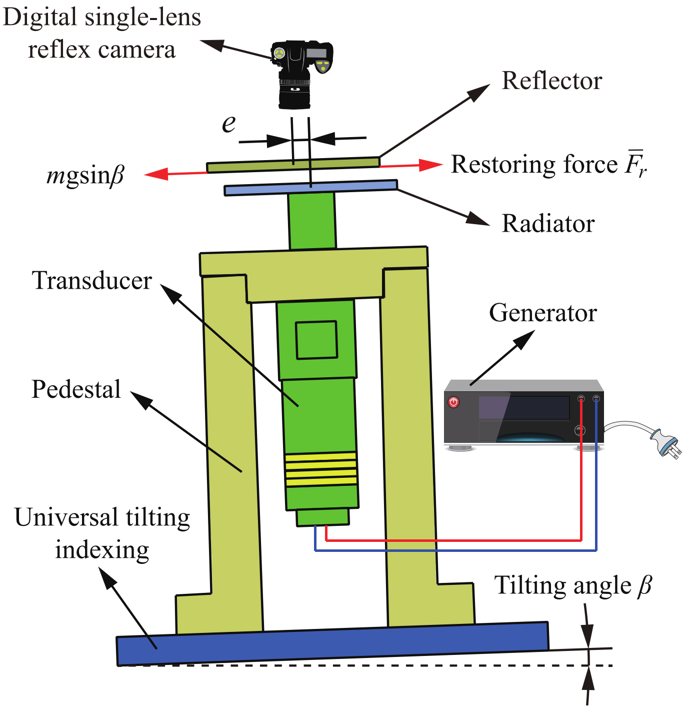

Figure 13: Schematic diagram of experimental measurement system, see Publication A.

Another measurement system utilizes a universal tilting indexing disc to approximately measure the restoring force [11, 66], which has the benefit of being easy to implement. An example of such a test setup is shown in Figure 13. It mainly contains a universal tilting indexing disc, a signal generator, a transducer, a pedestal, and the corresponding control unit. In addition, a camera is mounted for observing the misalignment performance of the reflector plate.

The transducer is fixed on the pedestal, which is mounted on the tilting indexing disc. This disc can be inclined to a specific angle β by regulating the control unit. Thus, when the reflector is suspended, the eccentricity e is regulated until the weight component $mg \sin \beta$ and the restoring force $\bar{F}_r$ are balanced with each other. In this way, the relationship between the restoring force and the eccentricity is obtained. The reflector is made of AL2024. The resolution of the disc determines the accuracy of the measured restoring force. In this work, the minimum tilting angle β is $20'$, which represents the minimum measured restoring force is 5.378 mN.

4 Summary of Appended Publications

The relevant publications of this dissertation are briefly summarized in this section. In addition, the individual contribution of the candidate to the three publications is indicated.

4.1 Publication A

Stabilizing Near-Field Acoustic Levitation: Investigation of Non-Linear Restoring Force Generated by Asymmetric Gas Squeeze Film

In the introduction of this publication, the advantages, applications, and research methods of the NFAL are discussed. Subsequently, the generation mechanism of the restoring force is presented. In the standing wave-based NFAL, the restoring force is produced by the gradient of the film pressure in the fluid domain. In addition, the related research about the stability of the levitator is reviewed. However, the above-mentioned methods [16, 85, 90] in subsection 1.1.1 cannot obtain the pressure distribution representing the airflow. Therefore, this publication addresses the problems of computing the actual pressure profile in the squeeze film and predicting the restoring force.

An air lubrication theory-based approach for calculating the restoring force of the levitator is proposed in this publication. Firstly, due to the misalignment of the levitator, the squeeze film thickness is discontinuous in the solving domain, which is handled by introducing an imaginary grooved levitator. Secondly, by using the EDM and the Newton-Raphson method, the pressure distribution is computed by solving the combination of the dynamic equation of the levitator and the Reynolds equation. Finally, the restoring force that arises from the pressure gradient is obtained. Furthermore, a specifically constructed testing device is built to measure the restoring force.

The calculated pressure distribution illustrates that four variables will influence the distribution of the restoring force, namely the eccentricity and the weight of the levitator as well as the mode and vibration amplitude of the radiator. The proposed numerical calculation method is verified by comparing the numerical results with the experimental data. The research results point out that the restoring force is increased with the increment of the vibration amplitude, eccentricity, and weight of the reflector. In addition, the restoring force in the first-order longitudinal vibration mode of the radiator is higher than for the second- and third-order modes. This paper contributes to providing guidance for the design of an NFAL-based stable positioning system in industrial applications.

Individual contributions of the candidate: This paper was published in the international peer-reviewed journal *The Journal of the Acoustical Society of America*. My contribution to this work was to propose an analysis model and code writing. I have performed numerical calculations, analyzed the results, and written the original draft of the manuscript.

4.2 Publication B

Theoretical Analysis on the Static and Dynamic Performances of a Squeeze Film Air Journal Bearing with Three Separate Pads Structure

This publication starts with the design concept of the SFB and points out its advantages, such as oil-free and low wear. The research development about the structure and the dynamic characteristics of the SFB is then reviewed. One distinct drawback of most SFBs [116-123] is the low load-carrying capacity. Zhao *et al.* [126, 127] proposed an SFB with three Langevin transducers which can significantly enhance its load-carrying capacity. However, the static and dynamic performance of this kind of SFB has not yet been investigated. Yet, this is fundamental for the design and application of the SFB. Therefore, the theoretical prediction of the static and dynamic performance of the three-pad SFB is presented in this publication.

A simplified theoretical model is proposed based on the SFB that consists of three separate Langevin transducers. The pressure distribution of the lubrication film between the bearing inner surface and the rotor outer surface is obtained by solving the steady Reynolds equation. The bearing forces are acquired by the integration of the film pressure in the inner surface of the bearing. The Newton-Raphson iteration method is applied to calculate the attitude angle and the eccentricity ratio of the rotor at the balance position. Next, the film pressure and thickness are modified by considering the perturbation variables. By substituting them into the dynamic Reynolds equation, a group of differential equations is derived. The eight dynamic coefficients are computed by solving this group of differential equations.

The comparison of the dimensionless pressure profile between the rotating rotor and the rotor at rest indicates that the squeeze effect is the major cause of high pressure. Further, the comparison between the predicted and published experimental data [127] validates the accuracy of the proposed calculation method. The static performance of the bearing is enhanced by increasing the vibration amplitude or decreasing the nominal clearance. The dynamic performance results indicate that higher synchronous direct dynamic coefficients are acquired for higher vibration amplitudes or lower rotation speeds. Through this study, it is helpful to determine the design and running parameters of squeeze film bearings under different working conditions.

Individual contributions of the candidate: This paper was published in the international peer-reviewed journal *International Journal of Mechanical Sciences*. My contribution to this work was to propose the analytical model and code writing. I have performed numerical calculations, analyzed the results, and written the original draft of the manuscript.

4.3 Publication C

Theoretical Analysis of a Contactless Transportation System for Cylindrical Objects Based on Ultrasonic Levitation

In the introduction of this publication, brief information on the mechanism of the NFAL is given. It is pointed out that two approaches are usually utilized to produce an acoustic viscous force, which corresponds to two types of NFAL, i.e., the traveling wave-based NFAL and the standing wave-based NFAL. The transportation systems based on these two types of NFAL are reviewed. However, the above-mentioned NFAL-based transportation systems [11, 51, 66, 68, 146-152, 155] in subsection 1.1.3 can only be used to transport the object with planar surfaces, whereas some components in the industry have cylindrical surfaces.

In this publication, the non-contact transportation of cylindrical objects is achieved by means of engraving one groove on the concave surface of the Langevin transducer. In this condition, the groove will break the symmetric pressure field between the levitator and the radiator. Based on the air lubrication theory, the asymmetric pressure distribution produces the levitation force and the thrusting force simultaneously. By using several grooved radiators, a transportation system is proposed to suspend and transport cylindrical objects. The film pressure profile is calculated by solving the non-linear Reynolds equation that takes into account the levitator motion in the horizontal direction. The EDM is used to deal with the problem of discontinuous film thickness caused by the groove. Therefore, the thrusting force and the levitation force are determined by the integral of the pressure gradient and the pressure over the solving domain, respectively.

The proposed numerical method is verified by comparing the calculated and published experimental results [165] of the levitation force in the same running conditions. The numerical results show that the thrusting force increases with increasing the radiator vibration amplitude, the levitator weight, or the groove width. The thrusting force maintains a stable value after the groove depth increases to a critical value. This critical value is 0.9 mm in this work. Moreover, the maximal thrusting force is obtained when the arc length of the groove equals the optimal value (40° in this work). This publication provides useful guidance for designing an available non-contact transportation system for cylindrical objects in industrial applications.

Individual contributions of the candidate: This paper was published in the international peer-reviewed journal *The Journal of the Acoustical Society of America*. My contribution to this work was to propose the transportation model and code writing. I have performed numerical calculations, analyzed the results, and written the first draft of the publication.

5 Discussion of Results

The NFAL technology opens up multiple application prospects in the fields of electronics manufacturing, microelectromechanical systems, and precision machinery technology. At present, there are mainly three application fields based on the NFAL, i.e., positioning system, SFB, and contactless transportation system. However, some problems are still existing in these applications, such as the stability of the floating objects in the positioning system, the dynamic performance of the SFB, and the transportation of the cylindrical objects, which prevent their industrial application. Therefore, this work is dedicated to studying and solving these problems based on analytical models and experimental methods. The main research results of these three application fields will be discussed in this section.

For positioning systems, two types of investigation methods are used to study the stability problem of the floating object. The first methodology uses theoretical methods to predict the magnitude of the restoring force, e.g., the block-spring model used by Koike *et al.* [58] and the acoustic radiation potential method used by Li *et al.* [90]. The second one is based on the experiments, e.g., Matsuo *et al.* [16] experimentally studied the effect of different cross-sections of the radiator on the stability. However, the visualized pressure profile representing the airflow in the squeeze film cannot be obtained by these methods [16, 58, 90]. For this reason, the air lubrication theory-based method is presented to calculate the restoring fore for the floating object in Publication A. Subsequently, the pressure distribution in the squeeze film is obtained by solving the Reynolds equation.

It is shown that the calculated pressure distribution is asymmetric due to the misalignment of the reflector. Therefore, the shear stresses are produced in the squeeze film due to the pressure gradient. The restoring force is computed by the integration of the shear stress over the solving domain. The calculated results pointed out that the restoring force is closely related to the eccentricity and the weight of the reflector as well as the mode shape and the vibration amplitude of the radiator, which is in accordance with Refs. [16, 85]. The calculated results of the restoring force are in good match with the experimental results for small eccentricity since the inclination of the reflector is ignored in this model. The restoring force exponentially increases as the eccentricity increases with an index less than 1, which is also found in Ref. [85]. The restoring force has an approximately linear relation with respect to the vibration amplitude, which is reported in Ref. [16] by experimental observations. This result is probably attributed to the fact that the squeeze effect is improved by increasing the vibration amplitude. Moreover, the restoring force increases with the increasing the reflector weight. The heavier reflector weight shows that the film pressure value is higher, which means that the pressure gradient in the squeeze film is greater. Therefore, the value of the restoring force will be greater as well. Since the positioning system has a greater load-carrying capacity in the third-order mode than in the first- and second-order mode [90], it leads to a lower levitation height and a smaller restoring force in the third-order mode.

The vibration source in most of the SFBs [116, 118, 119] is the piezoelectric plates, which leads to insufficient load-carrying capacity for these bearings. In order to improve this situation, Zhao *et al.* [127] proposed an active SFB which uses three Langevin transducers to constitute the construction of the bearing. However, the static and dynamic performances of this kind of bearing are not studied. In Publication B, the balance position of the rotor is computed by using the combination of the steady-state Reynolds equation and the Newton-Raphson iteration method. The infinitesimal perturbation method and the dynamic Reynolds equation are used to determine the dynamic coefficients of the bearing.

It is found in Publication B that the squeeze effect plays a major role in generating high pressure in the air squeeze film. In addition, the aerodynamic effect will weaken the load-carrying capacity of the bearing. On the contrary, Feng *et al.* [135] found that the aerodynamic effect mainly affects the change in pressure, and it has a positive influence on the bearing force. The possible reason for this contradictory result is that the vibration amplitude in this work is much higher than that in Ref. [135]. Furthermore, another kind of hybrid gas-lubricated bearing, namely the aerostatic porous bearing, also shows similar results [92, 93] as Publication B.

The proposed static and dynamic calculation methods presented in subsection 3.3 are verified by the experimental results published in Ref. [127]. The static numerical results show that the eccentricity ratio is increased, and the attitude angle is decreased by increasing the external load. This result can be found in other fluid lubrication bearings [181] as well. In addition, the eccentricity ratio decreases with the decrement of the nominal clearance since the squeeze effect will be improved by decreasing the clearance [119]. Since increasing the vibration amplitude means improving the levitation effect [27], the eccentricity ratio is decreased by increasing the vibration amplitude, which is also reported by experimental studies on SFBs [118, 182]. The dynamic numerical results point out that the synchronous direct dynamic coefficients decrease when increasing the rotation speed. This trend is similar to the results of the aerostatic bearing at high supply pressure [93]. Moreover, the synchronous direct dynamic coefficients increase with the increment of the vibration amplitude. This is due to the improvement of the squeeze effect and the increment of the quantity of viscous damping [183]. Pad-1 (see Figure 5) and Pad-3 have a significant influence on the direct dynamic coefficients, while Pad-2 has an important effect on the load-carrying capacity than the other two pads.

Finally, since some cylindrical components in the industry have a sensitive and precisely manufactured surface [156, 157], the contactless transportation of such components is necessary. However, most transportation systems [11, 51, 66, 68, 146-152, 155] based on the NFAL are only suitable for levitators with planar surfaces. According to the results of Publication A, the horizontal force can be obtained by engraving the groove. Additionally, in Publication B, the Langevin transducer has a cylindrical concave. Thus, by engraving a groove on the cylindrical concave of the Langevin transducer, a non-contact transportation system for cylindrical components is proposed in Publication C. The pressure profile between the concave and the component is calculated by computing the Reynolds equation.

The calculation results of the levitation force in this work agree well with the experimental results in Ref. [165] during the same conditions, which validates the numerical methods. It is observed for this contactless transportation system that the thrusting force increases at first and then maintains a constant value with the increment of the groove depth. This phenomenon occurs because the squeeze effect is still available in the groove domain at low groove depths. When the groove depth is high, the squeeze effect in the groove domain disappears, and the pressure distribution does not change. With the groove arc length increasing, the pressure gradient increases and the film thickness decreases. The thrusting force is highly dependent on both the film thickness and the pressure gradient according to equation (3.19). Consequently, the thrusting force is increased firstly and then is decreased by increasing the arc length of the groove. The optimum value for the arc length is nearly 40° in this work. Moreover, the thrusting force increases with respect to the increment of the groove width. This result is consistent with the result in Publication A. In addition, the thrusting force is linearly relative to the vibration since the squeeze effect is improved by the increment of the vibration amplitude [16].

6 Conclusion

As a new developing suspension technology, the NFAL utilizes the squeeze effect to generate the high-pressure field. Compared with the magnetic levitation, the NFAL has no material limit of the levitator. Compared with the air cushions, the NFAL has a more compact system. These characters make the NFAL has the potential application in the field of ultra-cleanness and ultra-precision, such as the transport of components of the microelectronics and microelectromechanical systems. In addition, the squeeze film bearing is designed by combining the NFAL and the gas-lubrication bearing, which can meet the requirements of high precision and frictionless. This work is dedicated to the study of the applications of the NFAL, namely positioning systems, SFBs, and contactless transportation systems. This work aims to optimize the design parameters of the system and to find suitable running conditions to achieve a high-performance levitation system.

In the positioning system, the generation mechanism of the restoring force for floating objects is theoretically analyzed based on the air lubrication theory. An experimental setup is built to measure the restoring force as validation. It is found that the restoring force is increased by increasing the eccentricity, which means the horizontal oscillation frequency is increasing. In order to establish a stable positioning system, the radiator vibration amplitude or the reflector weight has to be as large as possible within a reasonable range. The calculation results suggested that the restoring force decreases as the longitudinal mode order of the radiator increases, whereas the load-carrying capacity shows an opposite trend. Therefore, operating the levitation system in the second-order mode is recommended by considering the balance between stability and load-carrying capacity. The limitation of this analytical model is the neglect of the inclination of the reflector. However, this restriction is reasonable for reflectors with small eccentricities. It is suggested that the influence of the inclination in large eccentricity conditions should be discussed in future work.

Next, a modified calculation method for the dynamic coefficients of the SFB is originally presented to predict the dynamic performance of the SFB. By investigating the static performance of the bearing, it is found that there is a threshold value for the vibration amplitude and nominal clearance of the bearing to reach a balance between the squeeze effect and the aerodynamic effect. Consequently, the eccentricity can approximately remain constant with varying rotation speed, which provides guidance to control the rotor trajectory. The bearing load-carrying capacity increases as the rotation speed increases when the clearance of the bearing is higher or the vibration amplitude of the bearing is lower than its threshold values. Otherwise, the bearing load-carrying capacity decreases with increasing the rotation speed. Moreover, the eccentricity decreases with the decrement in the external load or with the increment in the vibration amplitude of the pad. In the study of the dynamic performance of the bearing, the higher synchronous direct dynamic coefficients are acquired when the rotation speed of the rotor is lower or the vibration amplitude of the bearing is higher, which is more expected for this bearing design. In addition, Pad-1 (see

Figure 5) and Pad-3 have more influence on the synchronous direct dynamic coefficients than Pad-2. Based on the current study, the investigation on the dynamic performance of a rotor supported by the SFBs will be implemented in future work.

Finally, this work deals with the problem of contactless transportation of cylindrical objects by using the NFAL. This is achieved by engraving one groove on the concave surface of the Langevin transducer to generate an asymmetric pressure distribution. The influence of the groove parameters on the transportation performance is subsequently analyzed. With respect to the groove parameters, the numerical results pointed out that the thrusting force firstly increases and then maintains a constant value with the increment in the groove depth. The arc length of the groove has an optimal value to acquire the maximum value of the thrusting force. In addition, the transportation performance is improved, but the load-carrying capacity is weakened by increasing the groove width. Therefore, it is important to determine the suitable groove parameters to obtain high transportation performance. Moreover, the radiator vibration amplitude or the levitator weight has a positive effect on the thrusting force. Future work focuses on manufacturing a prototype for this transportation system and introducing a control unit to precisely manipulate the motion trajectory of the levitator.

Bibliography

[1] G. Reinhart and J. Hoeppner. Non-contact handling using high-intensity ultrasonics. *CIRP Annals-Manufacturing Technology*, 49(1):5-8, 2000.

[2] W. S. Wang, S. Tatic-Lucic, W. L. Brown, and R. Vinci. Design of a bidirectional MEMS actuator with high displacement resolution, large driving force and power-free latching. *Microelectronic Engineering*, 85(3):587-598, 2008.

[3] G. Fedorko, V. Molnár, J. Živčák, M. Dovica, and N. Husáková. Failure analysis of textile rubber conveyor belt damaged by dynamic wear. *Engineering Failure Analysis*, 28:103-114, 2013.

[4] V. Vandaele, P. Lambert, and A. Delchambre. Non-contact handling in microassembly: Acoustical levitation. *Precision Engineering*, 29(4):491-505, 2005.

[5] B. J. Kang, L. S. Hung, S. K. Kuo, S. C. Lin, and C. M. Liaw. H∞ 2DOF control for the motion of a magnetic suspension positioning stage driven by inverter-fed linear motor. *Mechatronics*, 13(7):677-696, 2003.

[6] O. S. Kim, S. H. Lee, and D. C. Han. Positioning performance and straightness error compensation of the magnetic levitation stage supported by the linear magnetic bearing. *IEEE Transactions on Industrial Electronics*, 50(2):374-378, 2003.

[7] F. Erzincanli, J. M. Sharp, and S. Erhal. Design and operational considerations of a non-contact robotic handling system for non-rigid materials. *International Journal of Machine Tools and Manufacture*, 38(4):353-361, 1998.

[8] G. J. Laurent, A. Delettre, and N. Le Fort-Piat. A new aerodynamic-traction principle for handling products on an air cushion. *IEEE Transactions on robotics*, 27(2):379-384, 2011.

[9] K. Amano, S. Yoshimoto, M. Miyatake, and T. Hirayama. Basic investigation of noncontact transportation system for large TFT-LCD glass sheet used in CCD inspection section. *Precision Engineering*, 35(1):58-64, 2011.

[10] K. Feng, Y. Y. Liu, and M. M. Cheng. Numerical analysis of the transportation characteristics of a self-running sliding stage based on near-field acoustic levitation. *The Journal of the Acoustical Society of America*, 138(6):3723-3732, 2015.

[11] D. Koyama, K. Nakamura, and S. Ueha. A stator for a self-running, ultrasonically-levitated sliding stage. *IEEE Transactions on Ultrasonics, Ferroelectrics, and Frequency control*, 54(11):2337-2343, 2007.

[12] E. H. Brandt. Acoustic physics: suspended by sound. *Nature*, 413:474-475, 2001.

[13] R. Kashima, D. Koyama, and M. Matsukawa. Two-dimensional noncontact transportation of small objects in air using flexural vibration of a plate. *IEEE Transactions on Ultrasonics, Ferroelectrics, and Frequency control*, 62(12):2161-

2168, 2015.

[14] W. J. Xie, C. D. Cao, Y. J. Lü, Z. Y. Hong, and B. Wei. Acoustic method for levitation of small living animals. *Applied Physics Letters*, 89(21):214102, 2006.

[15] W. J. Xie and B. Wei. Parametric study of single-axis acoustic levitation. *Applied Physics Letters*, 79(6):881-883, 2001.

[16] E. Matsuo, Y. Koike, K. Nakamura, S. Ueha, and Y. Hashimoto. Holding characteristics of planar objects suspended by near-field acoustic levitation. *Ultrasonics*, 38(1-8):60-63, 2000.

[17] R. R. Whymark. Acoustic field positioning for containerless processing. *Ultrasonics*, 13(6):251-261, 1975.

[18] Y. D. Liang, H. Ling, and Y. Zhang. Study on the conditions of near-field acoustic levitation. *Advanced Materials Research*, 97-101:4135-4140, 2010.

[19] B.-T. Chu and R. E. Apfel. Acoustic radiation pressure produced by a beam of sound. *The Journal of the Acoustical Society of America*, 72(6):1673-1687, 1981.

[20] Y. Hashimoto, Y. Koike, and S. Ueha. Near-field acoustic levitation of planar specimens using flexural vibration. *The Journal of the Acoustical Society of America*, 100(4):2057-2061, 1996.

[21] Y. Hashimoto, Y. Koike, and S. Ueha. Acoustic levitation of planar objects using a longitudinal vibration mode. *Journal of the Acoustical Society of Japan (E)*, 16(3):189-192, 1995.

[22] S. Zhao and J. Wallaschek. A standing wave acoustic levitation system for large planar objects. *Archive of Applied Mechanics*, 81(2):123-139, 2011.

[23] E. O. J. Salbu. Compressible squeeze films and squeeze bearings. *Journal of Fluids Engineering-Transactions of ASME*, 86(2):355-364, 1964.

[24] J. V. Beck, W. G. Holliday, and C. L. Strodtman. Experiment and analysis of a flat disk squeeze-film bearing including effects of supported mass motion. *Journal of Tribology-Transactions of ASME*, 91(1):138-148, 1969.

[25] H. Nomura, T. Kamakura, and K. Matsuda. Theoretical and experimental examination of near-field acoustic levitation. *The Journal of the Acoustical Society of America*, 111(4):1578-1583, 2002.

[26] A. Minikes, I. Bucher, and S. Haber. Levitation force induced by pressure radiation in gas squeeze films. *The Journal of the Acoustical Society of America*, 116(1):217-226, 2004.

[27] W. J. Li, Y. Y. Liu, and K. Feng. Modelling and experimental study on the influence of surface grooves on near-field acoustic levitation. *Tribology International*, 116:138-146, 2017.

[28] X. N. Chang, B. Wei, M. Atherton, C. Mares, T. A. Stolarski, and A. Almurshedi. NFAL prototype design and feasibility analysis for self-levitated conveying. *Tribology Transactions*, 59(5):957-968, 2016.

[29] D. Ilssar and I. Bucher. On the slow dynamics of near-field acoustically levitated objects under High excitation frequencies. *Journal of Sound and Vibration*, 354:154-166, 2015.

[30] D. Ilssar, I. Bucher, and H. Flashner. Modeling and closed loop control of near-field acoustically levitated objects. *Mechanical Systems and Signal Processing*, 85:367-381, 2017.

[31] M. Wiesendanger. *Squeeze film air bearings using piezoelectric bending elements*. PhD thesis, École polytechnique fédérale de Lausanne, Lausanne, Switzerland, 2001.

[32] K. Feng and S. Kaneko. A numerical calculation model of multi wound foil bearing with the effect of foil local deformation. *Journal of System Design and Dynamics*, 1(3):648-659, 2007.

[33] C. A. Heshmat, D. S. Xu, and H. Heshmat. Analysis of gas lubricated foil thrust bearings using coupled finite element and finite difference methods. *Journal of Tribology-Transactions of ASME*, 122(1):199-204, 2000.

[34] S. K. Chen, H. C. Chou, and Y. Kang. Stability analysis of hydrodynamic bearing with herringbone grooved sleeve. *Tribology International*, 55(2):15-28, 2012.

[35] J. S. Larsen and I. F. Santos. Efficient solution of the non-linear Reynolds equation for compressible fluid using the finite element method. *Journal of the Brazilian Society of Mechanical Sciences Engineering*, 37(3):945-957, 2015.

[36] D. Bonneau and J. Absi. Analysis of aerodynamic journal bearings with small number of herringbone grooves by finite element method. *Journal of Tribology-Transactions of ASME*, 116(4):698-704, 1994.

[37] L. R. Gero and C. M. McC. Ettles. An evaluation of finite difference and finite element methods for the solution of the Reynolds equation. *Tribology Transactions*, 29(2):166-172, 1986.

[38] H. G. Elrod and T. Y. Chu. Inertia and energy effects in the developing gas film between two parallel flat plates. *Journal of Tribology-Transactions of ASME*, 95(4):524-532, 1973.

[39] H. Hashimoto. Squeeze film characteristics between parallel circular plates containing a single central air bubble in the inertial flow regime. *Journal of Tribology-Transactions of ASME*, 117(3):513-518, 1995.

[40] E. A. Hamza and D. A. Macdonald. A fluid film squeezed between two parallel plane surfaces. *Journal of Fluid Mechanics*, 109:147-160, 1981.

[41] B. Wei, M. Miyatake, S. Kawada, and S. Yoshimoto. The gas squeeze film

characteristics of acoustic levitation with various excitation disc shapes based on the modified reynolds equation. *Tribology Transactions*, 63(3):487-493, 2020.

[42] A. Smalley, J. Vohr, V. Castelli, and C. Wachmann. An analytical and experimental investigation of turbulent flow in bearing films including convective fluid inertia forces. *Journal of Tribology-Transactions of ASME*, 96(1):151-157, 1974.

[43] S. R. Turns. Annular squeeze films with inertial effects. *Journal of Tribology-Transactions of ASME*, 105(3):361-363, 1983.

[44] K. Tonder. A numerical assessment of the effect of striated roughness on gas lubrication. *Journal of Tribology-Transactions of ASME*, 106(3):315-319, 1984.

[45] J. W. White and P. E. Raad. Effect of a rough translating surface on gas film lubrication: a numerical and analytical study. *Journal of Tribology-Transactions of ASME*, 109(2):271-275, 1987.

[46] J. W. White. The effect of two-dimensional surface roughness on the load-carrying capacity of a thin compressible gas film. *Journal of Tribology-Transactions of ASME*, 115(2):246-252, 1993.

[47] T. A. Stolarski and C. Wei. Inertia effect in squeeze film air contact. *Tribology International*, 41(8):716-723, 2008.

[48] J. Li, W. W. Cao, P. K. Liu, and H. Ding. Influence of gas inertia and edge effect on squeeze film in near field acoustic levitation. *Applied Physics Letters*, 96(24):243507, 2010.

[49] P. K. Liu, J. Li, H. Ding, and C. W. W. Modeling and experimental study on near-field acoustic levitation by flexural mode. *IEEE Transactions on Ultrasonics, Ferroelectrics, and Frequency control*, 56(12):2679-2685, 2009.

[50] T. A. Stolarski and C. Wei. Load-carrying capacity generation in squeeze film action. *International Journal of Mechanical Sciences*, 48(7):736-741, 2006.

[51] A. Minikes and I. Bucher. Noncontacting lateral transportation using gas squeeze film generated by flexural traveling waves-numerical analysis. *The Journal of the Acoustical Society of America*, 113(5):2464-2473, 2003.

[52] T. A. Stolarski. Numerical modeling and experimental verification of compressible squeeze film pressure. *Tribology International*, 43(1-2):356-360, 2010.

[53] Y. Wada, D. Koyama, and K. Nakamura. Finite-element analysis of acoustic streaming generated between a bending transducer and a reflector through second-order approximated forces. *Acoustical Science and Technology*, 34(5):322-331, 2013.

[54] Y. Wada, T. Kundu, and K. Nakamura. Mesh-free distributed point source method for modeling viscous fluid motion between disks vibrating at ultrasonic frequency. *The Journal of the Acoustical Society of America*, 136(2):466-474, 2014.

[55] N. Brunetière and M. Wodtke. Considerations about the applicability of the Reynolds

equation for analyzing high-speed near field levitation phenomena. *Journal of Sound and Vibration*, 483:115496, 2020.

[56] Ansys CFX -pre theory guide, Ansys Inc., Release 18.1, Canonsburg, PA.

[57] Y. B. Yin. *Non-contact Object Transportation Using Near-field Acoustic Levitation Induced by Ultrasonic Flexural Waves*. PhD thesis, North Carolina State University, Raleigh, USA, 2007.

[58] Y. Koike, S. Ueha, A. Okonogi, T. Amano, and K. Nakamura. Suspension mechanism in near field acoustic levitation phenomenon. *2000 IEEE International Ultrasonics Symposium*, 1:671-674, San Juan, PR, USA, 2000.

[59] T. A. Stolarski and W. Chai. Self-levitating sliding air contact. *International Journal of Mechanical Sciences*, 48(6):601-620, 2006.

[60] F. M. Distel and G. Reinhart. Automated Design and Optimization of Rectangular Plate Sonotrodes for Squeeze Film Levitation. *Journal of Vibrational Engineering and Technologies* 3(2):151-160, 2015.

[61] G. Reinhart, J. Hoeppner, and J. Zimmermann. Non-contact wafer handling using high-intensity ultrasonics. *2001 IEEE/SEMI Advanced Semiconductor Manufacturing Conference* 139-140, Munich, Germany, 2001.

[62] T. Oiwa and M. Kato. Squeeze air bearing based on ultrasonic oscillation: Motion error compensation using amplitude modulation. *Review of scientific instruments*, 75(11):4615-4620, 2004.

[63] S. Yoshimoto, H. Kobayashi, and M. Miyatake. Float characteristics of a squeeze-film air bearing for a linear motion guide using ultrasonic vibration. *Tribology International*, 40(3):503-511, 2007.

[64] C. Chen, J. S. Wang, B. Jia, and F. Li. Design of a noncontact spherical bearing based on near-field acoustic levitation. *Journal of Intelligent Material Systems and Structures*, 25(6):755-767, 2014.

[65] J. F. Liu, X. G. Sun, X. Y. Jiao, H. X. Chen, S. M. Hua, and H. C. Zhang. The near-field acoustic levitation for spheres by transducer with concave spherical radiating surface. *Journal of Mechanical Science and Technology*, 27(2):289-295, 2013.

[66] J. H. Hu, G. R. Li, H. L. W. Chan, and C. L. Choy. A standing wave-type noncontact linear ultrasonic motor. *IEEE Transactions on Ultrasonics, Ferroelectrics, and Frequency control*, 48(3):699-708, 2001.

[67] S. Ueha, Y. Hashimoto, and Y. Koike. Non-contact transportation using near-field acoustic levitation. *Ultrasonics*, 38(1):26-32, 2000.

[68] Y. Hashimoto, Y. Koike, and S. Ueha. Transporting objects without contact using flexural traveling waves. *The Journal of the Acoustical Society of America*, 103(6):3230-3233, 1998.

[69] B. Yang, J. Q. Liu, D. Chen, and B. C. Cai. Theoretical and experimental research on a disk-type non-contact ultrasonic motor. *Ultrasonics*, 44(3):238-243, 2006.

[70] M. H. Shi, X. J. Liu, K. Feng, and K. Zhang. Experimental and numerical investigation of a self-adapting non-contact ultrasonic motor. *Tribology International*, 153:106624, 2021.

[71] R. Gabai, D. Ilssar, R. Shaham, N. Cohen, and I. Bucher. A rotational traveling wave based levitation device–Modelling, design, and control. *Sensors and Actuators A: Physical*, 255:34-45, 2017.

[72] H. Li, Q. Q. Quan, Z. Q. Deng, D. E. Bai, and Y. C. Wang. Development of a novel noncontact ultrasonic bearing actuated by piezoelectric transducers. *2017 IEEE International Ultrasonics Symposium*:1-4, Washington, DC, USA, 2017.

[73] M. H. Shi, K. Feng, J. H. Hu, J. Zhu, and H. L. Cui. Near-field acoustic levitation and applications to bearings: a critical review. *International Journal of Extreme Manufacturing*, 1(3):032002, 2019.

[74] S. Pan, D. Wang, and W. Q. Huang. A novel small motor measurement system based on ultrasonic bearings. *Measurement*, 168:108307, 2021.

[75] T. Amano, Y. Koike, K. Nakamura, S. Ueha, and Y. Hashimoto. A multi-transducer near field acoustic levitation system for noncontact transportation of large-sized planar objects. *Japanese Journal of Applied Physics*, 39(5S):2982, 2000.

[76] J. Li, P. K. Liu, H. Ding, and W. W. Cao. Modeling characterization and optimization design for PZT transducer used in Near Field Acoustic Levitation. *Sensors and Actuators A: Physical*, 171(2):260-265, 2011.

[77] N. Guo, P. Cawley, and D. Hitchings. The finite element analysis of the vibration characteristics of piezoelectric discs. *Journal of Sound and Vibration*, 159(1):115-138, 1992.

[78] X. L. Lu, J. H. Hu, H. M. Peng, and Y. Wang. A new topological structure for the Langevin-type ultrasonic transducer. *Ultrasonics*, 75:1-8, 2017.

[79] D. A. DeAngelis and G. W. Schulze. Performance of PZT8 versus PZT4 piezoceramic materials in ultrasonic transducers. *Physics Procedia*, 87:85-92, 2016.

[80] J. Wu, Y. Mizuno, and K. Nakamura. Vibration characteristics of polymer-based Langevin transducers. *Smart Materials and Structures*, 27(9):095013, 2018.

[81] J. F. Tressler, W. W. Cao, K. Uchino, and R. E. Newnham. Finite element analysis of the cymbal-type flextensional transducer. *IEEE Transactions on Ultrasonics, Ferroelectrics, and Frequency control*, 45(5):1363-1369, 1998.

[82] T. A. Stolarski and C. I. Woolliscroft. Use of near-field acoustic levitation in experimental sliding contact. *Journal of Applied Mechanics*, 74(4):816-820, 2007.

[83] A. Almurshedi, M. Atherton, C. Mares, and T. A. Stolarski. Modelling influence of

Poisson's contraction on squeeze film levitation of planar objects. *Journal of Applied Physics*, 125(9):095303, 2019.

[84] J. F. Liu, H. Jiang, H. You, X. Y. Jiao, H. X. Chen, and G. J. Liu. Non-contact transportation of heavy load objects using ultrasonic suspension and aerostatic suspension. *Proceedings of the Institution of Mechanical Engineers, Part C: Journal of Mechanical Engineering Science*, 228(5):840-851, 2014.

[85] J. H. Hu, K. Nakamura, and S. Ueha. Stability analysis of an acoustically levitated disk. *IEEE Transactions on Ultrasonics, Ferroelectrics, and Frequency control*, 50(2):117-127, 2003.

[86] J. H. Hu, K. Nakamura, and S. Ueha. An analysis of a noncontact ultrasonic motor with an ultrasonically levitated rotor. *Ultrasonics*, 35(6):459-467, 1997.

[87] J. Saito, J. R. Friend, K. Nakamura, and S. Ueha. Resonant mode design for noncontact ultrasonic motor with levitated rotor. *Japanese journal of applied physics*, 44(6S):4666, 2005.

[88] C.-H. Kim and J.-G. Ih. On the horizontal wobbling of an object levitated by near-field acoustic levitation. *Ultrasonics*, 46(4):331-335, 2007.

[89] S. Yoshimoto, H. Sekine, and M. Miyatake. A non-contact chuck using ultrasonic vibration: analysis of the primary cause of the holding force acting on a floating object. *Proceedings of the Institution of Mechanical Engineers, Part C: Journal of Mechanical Engineering Science*, 224(2):305-313, 2010.

[90] J. Li, P. K. Liu, H. Ding, and W. W. Cao. Nonlinear restoring forces and geometry influence on stability in near-field acoustic levitation. *Journal of Applied Physics*, 109(8):084518, 2011.

[91] F. Wardle. *Ultra-precision bearings*. Woodhead Publishing, Cambridge, UK, 1st edition 2015.

[92] L. San Andrés. Hybrid flexure pivot-tilting pad gas bearings: analysis and experimental validation. *Journal of Tribology-Transactions of ASME*, 128(3):551-558, 2006.

[93] K. Feng, Y. H. Wu, W. H. Liu, X. Y. Zhao, and W. J. Li. Theoretical investigation on porous tilting pad bearings considering tilting pad motion and porous material restriction. *Precision Engineering*, 53:26-37, 2018.

[94] B. J. Hamrock, S. R. Schmid, and B. O. Jacobson. *Fundamentals of fluid film lubrication*. CRC press, Boca Raton, 2nd edition 2004.

[95] H. Heshmat and P. Hermel. Compliant foil bearings technology and their application to high speed turbomachinery. *Tribology Series*, 25:559-575, 1993.

[96] L. San Andrés and B. Rodríguez. Experiments with a rotor-hybrid gas bearing system undergoing maneuver loads from its base support. *Journal of Engineering for Gas*

Turbines and Power-Transactions of ASME, 142(11):111004, 2020.

[97] B. Sternlicht. Gas-Bearing Turbomachinery. *Journal of Tribology-Transactions of ASME*, 90(4):665-678, 1968.

[98] A. Angantyr and J. O. Aidanpaa. Constrained optimization of gas turbine tilting pad bearing designs. *Journal of Engineering for Gas Turbines and Power-Transactions of ASME*, 128(4):873-878, 2006.

[99] Y. Li, F. H. Duan, L. Fan, and Y. Yan. Static error model of a three-floated gyroscope with a rotor supported on gas-lubricated bearings. *Proceedings of the Institution of Mechanical Engineers, Part C: Journal of Mechanical Engineering Science*, 232(16):2850-2860, 2018.

[100] L. Smolík, M. Hajžman, and M. Byrtus. Investigation of bearing clearance effects in dynamics of turbochargers. *International Journal of Mechanical Sciences*, 127:62-72, 2017.

[101] L. Gu, E. Guenat, and J. Schiffmann. A review of grooved dynamic gas bearings. *Applied Mechanics Reviews*, 72(1):010802, 2020.

[102] G. W. K. Ford, D. M. Harris, and D. Pantall. Principles and applications of hydrodynamic-type gas bearings. *Proceedings of the Institution of Mechanical Engineers*, 171(1):93-128, 1957.

[103] H. Heshmat. Advancements in the performance of aerodynamic foil journal bearings: high speed and load capability. *Journal of Tribology-Transactions of ASME*, 116(2):287-294, 1994.

[104] Y. L. Yu, G. Pu, T. C. Jiang, and K. Jiang. A dragonfly wing inspired biomimetic aerodynamic thrust bearing for increased load capacity. *International Journal of Mechanical Sciences*, 176:105550, 2020.

[105] F. C. Xu, Y. Sun, G. H. Zhang, and Z. S. Liu. Effect of bump structural friction on the performance of bump foil bearing and rotor dynamic behavior: Experimental study. *Proceedings of the Institution of Mechanical Engineers, Part J: Journal of Engineering Tribology*, 233(5):702-711, 2019.

[106] C.-C. Lee and H.-I. You. Characteristics of externally pressurized porous gas bearings considering structure permeability. *Tribology Transactions*, 52(6):768-776, 2009.

[107] D. Kim and D. Lee. Design of three-pad hybrid air foil bearing and experimental investigation on static performance at zero running speed. *Journal of Engineering for Gas Turbines and Power-Transactions of ASME*, 132(12):122504, 2010.

[108] A. Charki, K. Diop, S. Champmartin, and A. Ambari. Numerical simulation and experimental study of thrust air bearings with multiple orifices. *International Journal of Mechanical Sciences*, 72:28-38, 2013.

[109] T. A. Stolarski and S. P. Woolliscroft. Performance of a self-lifting linear air contact.

Proceedings of the Institution of Mechanical Engineers Part C: Journal of Mechanical Engineering Science, 221(9):1103-1115, 2007.

[110] S. Zhao and J. Wallaschek. Experimental investigations of ultrasonic levitation in a machine tool spindle system. *2009 IEEE International Ultrasonics Symposium*:1-4, Rome, Italy, 2009.

[111] H. Li, Q. Q. Quan, Z. Q. Deng, D. E. Bai, and Y. C. Wang. Design and experimental study on an ultrasonic bearing with bidirectional carrying capacity. *Sensors Actuators A: Physical*, 273:58-66, 2018.

[112] H. Li and Z. Q. Deng. Prediction of load-carrying capacity in the radial direction for piezoelectric-driven ultrasonic bearings. *IEEE Access*, 7:30599-30614, 2019.

[113] C. Pan. *Squeeze-film gas bearing technology*. 1968 [accessed 4 August, 2013] https://ntrs.nasa.gov/citations/19680000180.

[114] S. Yoshimoto. Floating characteristics of squeeze-film gas bearings with vibration absorber for linear motion guide. *Journal of Tribology-Transactions of ASME*, 119(3):531-536, 1997.

[115] J. L. Gupta and G. M. Deheri. Effect of roughness on the behavior of squeeze film in a spherical bearing. *Tribology Transactions*, 39(1):99-102, 1996.

[116] D. N. Ha, T. A. Stolarski, and S. Yoshimoto. An aerodynamic bearing with adjustable geometry and self-lifting capacity. Part 1: self-lift capacity by squeeze film. *Proceedings of the Institution of Mechanical Engineers, Part J: Journal of Engineering Tribology*, 219(1):33-39, 2005.

[117] P. Guo and H. Gao. An active non-contact journal bearing with bi-directional driving capability utilizing coupled resonant mode. *CIRP Annals-Manufacturing Technology*, 67(1):405-408, 2018.

[118] K. Feng, M. H. Shi, T. Gong, Y. Y. Liu, and J. Zhu. A novel squeeze-film air bearing with flexure pivot-tilting pads: Numerical analysis and measurement. *International Journal of Mechanical Sciences*, 134:41-50, 2017.

[119] T. A. Stolarski, Y. Xue, and S. Yoshimoto. Air journal bearing utilizing near-field acoustic levitation stationary shaft case. *Proceedings of the Institution of Mechanical Engineers, Part J: Journal of Engineering Tribology*, 225(3):120-127, 2011.

[120] R. Gawarkiewicz, T. A. Stolarski, and K. Tesch. Acoustic journal bearing—a search for adequate configuration. *Tribology International*, 92:387-394, 2015.

[121] C. Wang and Y. J. Au. Levitation characteristics of a squeeze-film air journal bearing at its normal modes. *The International Journal of Advanced Manufacturing Technology*, 60(1-4):1-10, 2012.

[122] C. Wang and Y. J. Au. Comparative performance of squeeze film air journal bearings made of aluminium and copper. *The International Journal of Advanced*

Manufacturing Technology, 65(1-4):57-66, 2013.

[123] M. H. Shi, L. An, K. Feng, Z. Y. Guo, and W. H. Liu. Numerical and experimental study on the influence of material characteristics on the levitation performance of squeeze-film air bearing. *Tribology International*, 126:307-316, 2018.

[124] Y. K. Wang and P. Guo. Stiffness modeling for near field acoustic levitation bearings. *Applied Physics Letters*, 118(20):204102, 2021.

[125] Z. Y. Hong, P. Lü, D. L. Geng, W. Zhai, N. Yan, and B. Wei. The near-field acoustic levitation of high-mass rotors. *Review of Scientific Instruments*, 85(10):104904, 2014.

[126] S. Zhao, J. Twiefel, and J. Wallaschek. Design and experimental investigations of high power piezoelectric transducers for a novel squeeze film journal bearing. *Active and Passive Smart Structures and Integrated Systems 2009*, 7288:72881G, San Diego, California, United States, 2009.

[127] S. Zhao, S. Mojrzisch, and J. Wallaschek. An ultrasonic levitation journal bearing able to control spindle center position. *Mechanical Systems and Signal Processing*, 36(1):168-181, 2013.

[128] H. Li, Y. X. Hua, Q. Q. Quan, D. E. Bai, Y. C. Wang, and Z. Q. Deng. On the modeling of levitation force for ultrasonic journal bearings actuated by piezoelectric transducers. *Journal of Intelligent Material Systems and Structures*, 29(6):1113-1119, 2018.

[129] T. A. Stolarski, R. Gawarkiewicz, and K. Tesch. Acoustic journal bearing–Performance under various load and speed conditions. *Tribology International*, 102:297-304, 2016.

[130] T. A. Stolarski, R. Gawarkiewicz, and K. Tesch. Extended duration running and impulse loading characteristics of an acoustic bearing with enhanced geometry. *Tribology Letters*, 65(2):46, 2017.

[131] T. Shou, S. Yoshimoto, and T. A. Stolarski. Running performance of an aerodynamic journal bearing with squeeze film effect. *International Journal of Mechanical Sciences*, 77:184-193, 2013.

[132] H. Li and Z. Q. Deng. Experimental study on friction characteristics and running stability of a novel ultrasonic levitating bearing. *IEEE Access*, 6:21719-21730, 2018.

[133] M. H. Shi, X. J. Liu, K. Feng, K. Zhang, and M. Huang. Running performance of a squeeze film air bearing with flexure pivot tilting pad. *Tribology Transactions*, 63(4):704-717, 2020.

[134] T. A. Stolarski. Running characteristics of aerodynamic bearing with self-lifting capability at low rotational speed. *Advances in Tribology*, 2011:973740, 2011.

[135] K. Feng, M. H. Shi, T. Gong, and Z. Huang. Integrated numerical analysis on the performance of a hybrid gas-lubricated bearing utilizing near-field acoustic levitation. *Tribology Transactions*, 61(3):482-493, 2018.

[136] T. A. Stolarski and M. Miyatake. Acoustic journal bearing with changeable geometry and built-in flexibility. *Journal of Tribology-Transactions of ASME*, 140(6):061707, 2018.

[137] J. V. Beck and C. L. Strodtman. Stability of a squeeze-film journal bearing. *Journal of Tribology-Transactions of ASME*, 89(3):369-373, 1967.

[138] J. W. Lund. Calculation of stiffness and damping properties of gas bearings. *Journal of Tribology-Transactions of ASME*, 90(4):793-803, 1968.

[139] J.-P. Peng and M. Carpino. Calculation of stiffness and damping coefficients for elastically supported gas foil bearings. *Journal of Tribology-Transactions of ASME*, 115(1):20-27, 1993.

[140] M. Amine H., M. Arghir, and M. Frocot. Comparison between numerical and experimental dynamic coefficients of a hybrid aerostatic bearing. *Journal of Engineering for Gas Turbines and Power-Transactions of ASME*, 134(12):122506, 2012.

[141] L. L. Li, D. Zhang, and Y. H. Xie. Effect of misalignment on the dynamic characteristic of MEMS gas bearing considering rarefaction effect. *Tribology International*, 139:22-35, 2019.

[142] K. Czolczynski. *Rotordynamics of gas-lubricated journal bearing systems*. Springer Science and Business Media, New York, 1999.

[143] K. Sim and D. Kim. Design of flexure pivot tilting pads gas bearings for high-speed oil-free microturbomachinery. *Journal of Tribology-Transactions of ASME*, 129(1):112-119, 2007.

[144] L. San Andrés and T. H. Kim. Analysis of gas foil bearings integrating FE top foil models. *Tribology International*, 42(1):111-120, 2009.

[145] E. Guenat and J. Schiffmann. Dynamic force coefficients identification on air-lubricated herringbone grooved journal bearing. *Mechanical Systems Signal Processing*, 136:106498, 2020.

[146] J. Li, W. W. Cao, and W. J. Zhang. A nonlinear model for the layer between plates in acoustic noncontact transportation. *Journal of Applied Physics*, 116(21):214905, 2014.

[147] T. Ide, J. Friend, K. Nakamura, and S. Ueha. A non-contact linear bearing and actuator via ultrasonic levitation. *Sensors and Actuators A: Physical*, 135(2):740-747, 2007.

[148] D. Koyama, T. Ide, J. R. Friend, K. Nakamura, and S. Ueha. An ultrasonically levitated noncontact stage using traveling vibrations on precision ceramic guide rails. *IEEE Transactions on Ultrasonics, Ferroelectrics, and Frequency control*, 54(3):597-604, 2007.

[149] W. J. Li, Y. Q. Zhu, K. Feng, and K. Zhang. Effect of surface grooves on the characteristics of noncontact transportation using near-field acoustic levitation.

Tribology Transactions, 61(5):960-971, 2018.

[150] J. H. Hu, K. C. Cha, and K. C. Lim. New type of linear ultrasonic actuator based on a plate-shaped vibrator with triangular grooves. *IEEE Transactions on Ultrasonics, Ferroelectrics, and Frequency control*, 51(10):1206-1208, 2004.

[151] B. Wei, R. Shaham, and I. Bucher. Theoretical investigation and prototype design for non-parallel squeeze film movement platform driven by standing waves. *Tribology International*, 119:539-548, 2018.

[152] K. Y. Chen, S. M. Gao, Y. Y. Pan, and P. Guo. Self-running and self-floating two-dimensional actuator using near-field acoustic levitation. *Applied Physics Letters*, 109(12):123503, 2016.

[153] Y. Yang, K. Y. Chen, and P. Guo. Noncontact planar stage based on near-Field acoustic transportation. *Journal of Micro-and Nano-Manufacturing*, 8(2):021002, 2020.

[154] K. Aono, M. Aoyagi, H. Kajiwara, H. Tamura, and T. Takano. Increase of holding force in near-field acoustic levitation of tabular object inserted between opposing vibration sources. *Japanese Journal of Applied Physics*, 58(SG):SGGD11, 2019.

[155] Y. Hashimoto, Y. Koike, and S. Ueha. Noncontact suspending and transporting planar objects by using acoustic levitation. *IEEJ Transactions on Industry Applications*, 117(11):1406-1407, 1997.

[156] X. Q. Hao, S. Y. Pei, L. Wang, H. Xu, N. He, and B. H. Lu. Microtexture fabrication on cylindrical metallic surfaces and its application to a rotor-bearing system. *The International Journal of Advanced Manufacturing Technology*, 78(5-8):1021-1029, 2015.

[157] J. Qian, W. Li, and H. Ohmori. Cylindrical grinding of bearing steel with electrolytic in-process dressing. *Precision engineering*, 24(2):153-159, 2000.

[158] O. Reynolds. On the theory of lubrication and its application to Mr. Beauchamp tower's experiments, including an experimental determination of the viscosity of olive oil. *Philosophical transactions of the Royal Society of London*, 177:157-234, 1886.

[159] A. Minikes and I. Bucher. Comparing numerical and analytical solutions for squeeze-film levitation force. *Journal of Fluids and Structures*, 22(5):713-719, 2006.

[160] S. Z. Wen and P. Huang. *Principles of tribology*. John Wiley & Sons, New York, 2012.

[161] Y. Wada, D. Koyama, and K. Nakamura. Acoustic streaming in an ultrasonic air pump with three-dimensional finite-difference time-domain analysis and comparison to the measurement. *Ultrasonics*, 54(8):2119-2125, 2014.

[162] S. S. Mohite, V. R. Sonti, and R. Pratap. A compact squeeze-film model including inertia, compressibility, and rarefaction effects for perforated 3-D MEMS structures.

Journal of Microelectromechanical Systems, 17(3):709-723, 2008.

[163] W. A. Gross. *Gas film lubrication*. John Wiley & Sons, New York, 1962.

[164] Y. Z. Wang and B. Wei. Mixed-modal disk gas squeeze film theoretical and experimental analysis. *International Journal of Modern Physics B*, 27(25):1350168, 2013.

[165] H. Li, Q. Q. Quan, Z. Q. Deng, Y. X. Hua, Y. C. Wang, and D. E. Bai. A novel noncontact ultrasonic levitating bearing excited by piezoelectric ceramics. *Applied Sciences*, 6(10):280, 2016.

[166] Q. Y. Chang, P. R. Yang, Y. G. Meng, and S. Z. Wen. Thermoelastohydrodynamic analysis of the static performance of tilting-pad journal bearings with the Newton–Raphson method. *Tribology international*, 35(4):225-234, 2002.

[167] K. Feng and S. Kaneko. Analytical model of bump-type foil bearings using a link-spring structure and a finite-element shell model. *Journal of Tribology-Transactions of ASME*, 132(2):021706, 2010.

[168] H. Heshmat, J. A. Walowit, and O. Pinkus. Analysis of gas-lubricated foil journal bearings. *Journal of Tribology-Transactions of ASME*, 105(4):647-655, 1983.

[169] F. A. Morrison. *An introduction to fluid mechanics*. Cambridge University Press, New York, 2013.

[170] E. Kreyszig, H. Kreyszig, and E. J. Norminton. *Advanced Engineering Mathematics*. John Wiley & Sons, New York, 10th eddition 2009.

[171] Q. Li, S. Zhang, L. Ma, W. W. Xu, and S. Y. Zheng. Stiffness and damping coefficients for journal bearing using the 3D transient flow calculation. *Journal of Mechanical Science and Technology*, 31(5):2083-2091, 2017.

[172] Z. L. Qiu and A. K. Tieu. The effect of perturbation amplitudes on eight force coefficients of journal bearings. *Tribology Transactions*, 39(2):469-475, 1996.

[173] K. Feng, H. Q. Guan, Z. L. Zhao, and T. Y. Liu. Active bump-type foil bearing with controllable mechanical preloads. *Tribology International*, 120:187-202, 2018.

[174] K. Feng, X. Y. Zhao, C. J. Huo, and Z. M. Zhang. Analysis of novel hybrid bump-metal mesh foil bearings. *Tribology International*, 103:529-539, 2016.

[175] C. E. Merelli, D. O. Barilá, G. G. Vignolo, and L. M. Quinzani. Dynamic coefficients of finite length journal bearing. Evaluation using a regular perturbation method. *International Journal of Mechanical Sciences*, 151:251-262, 2019.

[176] X. Z. Ma, S. L. Xie, and W. K. Zhang. Influence of the disturbance frequency on the dynamic characteristics of an ultrasonic gas squeeze film. *Tribology Transactions*, 59(4):690-697, 2016.

[177] J. W. Lund. Review of the concept of dynamic coefficients for fluid film journal

bearings. *Journal of Tribology-Transactions of ASME*, 109(1):37-41, 1987.

[178] S. Chino, Y. Kato, Y. Ishino, M. Takasaki, and T. Mizuno. Actuation force characteristics of ultrasonic suspension for minute object. *2011 IEEE International Ultrasonics Symposium*:1218-1221, Orlando, FL, USA, 2011.

[179] K. Uchiage, Y. Ishino, M. Takasaki, and T. Mizuno. Enlargement of floator size in ultrasonic suspension by arranging the shape of vibrating surface. *2014 IEEE International Ultrasonics Symposium*:2510-2513, Chicago, IL, USA, 2014.

[180] M. Takasaki, S. Chino, Y. Kato, Y. Ishino, and T. Mizuno. Actuation force measurement mechanism for non-contact ultrasonic suspension. *Key Engineering Materials*, 523:727-732, 2012.

[181] K. Feng, W. H. Liu, Z. M. Zhang, and T. Zhang. Theoretical model of flexure pivot tilting pad gas bearings with metal mesh dampers in parallel. *Tribology International*, 94:26-38, 2016.

[182] Y. Ono, S. Yoshimoto, and M. Miyatake. Impulse-load dynamics of squeeze film gas bearings for a linear motion guide. *Journal of Tribology-Transactions of ASME*, 131(4):041706, 2009.

[183] M. Carpino and G. Talmage. Prediction of rotor dynamic coefficients in gas lubricated foil journal bearings with corrugated sub-foils. *Tribology Transactions*, 49(3):400-409, 2006.

Part II Appended Publications

Publication A

Reproduced from

Yuanyuan Liu, Minghui Shi, Kai Feng, Kian K. Sepahvand, and Steffen Marburg

Stabilizing near-field acoustic levitation: Investigation of non-linear restoring force generated by asymmetric gas squeeze film

in The Journal of the Acoustical Society of America, Volume 148, Issue 3, 2020, pp. 1468-1477, DOI: https://doi.org/10.1121/10.0001963, with the permission of the Acoustical Society of America.

AIP PUBLISHING LICENSE
TERMS AND CONDITIONS

Jun 10, 2022

This Agreement between Technical University of Munich -- Yuanyuan Liu ("You") and AIP Publishing ("AIP Publishing") consists of your license details and the terms and conditions provided by AIP Publishing and Copyright Clearance Center.

License Number	5325501139792
License date	Jun 10, 2022
Licensed Content Publisher	Acoustical Society of America
Licensed Content Publication	The Journal of the Acoustical Society of America
Licensed Content Title	Stabilizing near-field acoustic levitation: Investigation of non-linear restoring force generated by asymmetric gas squeeze film
Licensed Content Author	Yuanyuan Liu, Minghui Shi, Kai Feng, et al
Licensed Content Date	Sep 1, 2020
Licensed Content Volume	148

Licensed Content Issue	3
Type of Use	Thesis/Dissertation
Requestor type	Author (original article)
Format	Print and electronic
Portion	Excerpt (> 800 words)
Will you be translating?	No
Title	Theoretical Analysis on Applications of Near-field Acoustic Levitation: Positioning, Bearing, and Transportation Systems
Institution name	Techincal University of Munich
Expected presentation date	Jul 2022
Portions	Full article
Requestor Location	Technical University of Munich Boltzmannstraße 15 Munich, 85748 Germany Attn: Technical University of Munich
Total	0.00 EUR

Terms and Conditions

Acoustic Society of America -- Terms and Conditions: Permissions Uses

Acoustic Society of America ("ASA") hereby grants to you the non-exclusive right and license to use and/or distribute the Material according to the use specified in your order, on a one-time basis, for the specified term, with a maximum distribution equal to the number that you have ordered. Any links or other content accompanying the Material are not the subject of this license.

1. You agree to include the following copyright and permission notice with the reproduction of the Material:"Reprinted with permission from [FULL CITATION]. Copyright [PUBLICATION YEAR], Acoustic Society of America." For an article, the copyright and permission notice must be printed on the first page of the article or book chapter. For photographs, covers, or tables, the copyright and permission notice may appear with the Material, in a footnote, or in the reference list.
2. If you have licensed reuse of a figure, photograph, cover, or table, it is your responsibility to ensure that the material is original to ASA and does not contain the copyright of another entity, and that the copyright notice of the figure, photograph, cover, or table does not indicate that it was reprinted by ASA, with permission, from another source. Under no circumstances does ASA, purport or intend to grant permission to reuse material to which it does not hold copyright.
3. You may not alter or modify the Material in any manner. You may translate the Material into another language only if you have licensed translation rights. You may not use the Material for promotional purposes. ASA reserves all rights not specifically granted herein.
4. The foregoing license shall not take effect unless and until ASA or its agent, Copyright Clearance Center, receives the Payment in accordance with Copyright Clearance Center Billing and Payment Terms and Conditions, which are incorporated herein by reference.
5. ASA or the Copyright Clearance Center may, within two business days of granting this license, revoke the license for any reason whatsoever, with a full refund payable to you. Should you violate the terms of this license at any time, ASA, Acoustic Society of America, or Copyright Clearance Center may revoke the license with no refund to you. Notice of such revocation will be made using the contact information provided by you. Failure to receive such notice will not nullify the revocation.
6. ASA makes no representations or warranties with respect to the Material. You agree to indemnify and hold harmless ASA, Acoustic Society of America, and their officers, directors, employees or agents from and against any and all claims arising out of your use of the Material other than as specifically authorized herein.
7. The permission granted herein is personal to you and is not transferable or assignable without the prior written permission of ASA. This license may not be amended except in a writing signed by the party to be charged.
8. If purchase orders, acknowledgments or check endorsements are issued on any forms containing terms and conditions which are inconsistent with these provisions, such inconsistent terms and conditions shall be of no force and effect. This document, including the CCC Billing and

Payment Terms and Conditions, shall be the entire agreement between the parties relating to the subject matter hereof.

This Agreement shall be governed by and construed in accordance with the laws of the State of New York. Both parties hereby submit to the jurisdiction of the courts of New York County for purposes of resolving any disputes that may arise hereunder.

Questions? customercare@copyright.com or +1-855-239-3415 (toll free in the US) or +1-978-646-2777.

JASA ARTICLE

Stabilizing near-field acoustic levitation: Investigation of non-linear restoring force generated by asymmetric gas squeeze film

Yuanyuan Liu,[1,a)] Minghui Shi,[2] Kai Feng,[2] Kian K. Sepahvand,[1] and Steffen Marburg[1]
[1]*Chair of Vibro-Acoustics of Vehicles and Machines, Technical University of Munich, Boltzmann Strasse 15, 85748 Garching b. Munich, Germany*
[2]*State Key Laboratory of Advanced Design and Manufacturing for Vehicle Body, Hunan University, Lushan South Road 2, Yuelu District, Changsha 410082, China*

ABSTRACT:
The instability of a floating object is the main factor preventing near-field acoustic levitation (NAFL) from being widely used in the manufacture of micro-electro-mechanical systems. Therefore, investigating the restoring force due to the generation mechanisms of NAFL is necessary to ensure the stable levitation of the floating object. This study presents a theoretical analysis to evaluate the restoring force based on the gas-film-lubrication theory. The gas-film pressure between the reflector and the radiator is expressed in the form of the dimensionless Reynolds equation in a cylindrical coordinate system, which is solved by an eight-point discrete grid method due to the discontinuous gas-film distribution. An experimental rig is constructed to measure the restoring force at various eccentricities, which can be used to support the developed numerical model. The theoretical results show that the restoring force increases with an increment in eccentricity, which agrees with experimental results. Furthermore, theoretical prediction results indicate that the restoring force increases when the amplitude of the radiator and weight of the levitator increases, which indicates higher system stability. The results of the radiator vibration mode on the restoring force show that the restoring force is the largest in the first-order mode. © *2020 Acoustical Society of America.*
https://doi.org/10.1121/10.0001963

(Received 7 April 2020; revised 30 July 2020; accepted 27 August 2020; published online 15 September 2020)
[Editor: Mark Hamilton] Pages: 1468–1477

I. INTRODUCTION

Near-field acoustic levitation (NFAL) technology has been developing rapidly in recent years. In comparison with the traditional non-contact levitation technology such as air cushion[1] and magnetic systems,[2] the NFAL system is a very compact system that does not need an additional air compressor to provide high air pressure and does not produce any undesirable magnetic field. Researchers have presented various studies on the application of the NFAL technology due to its promising potential in the application of micro-assembly in micro-electronics and micro-electro-mechanical systems (MEMS).[3] For instance, several non-contact transporting systems have been proposed by using transport objects with different cross sections.[4,5] Moreover, some new concepts for bearing designs[6–8] that are based on NFAL have been introduced to meet the ultra-precision, low wear, and oil-free requirement. Meanwhile, research on the NFAL mechanism and load-carrying capacity predictors are also developing. Hashimoto *et al.*[9] have considered the case where acoustic waves propagate from the radiating surface in a vertical direction, and then they derived a relationship between levitation distance, weight of the levitated object, and vibration amplitude of the radiation plate based on linear acoustic theory. *In addition, Wada* et al.[10–12] *used some other methods to calculate the fluid motion between a vibrating plate and other plates, for example, finite-element analysis and the distributed point source method (DPSM).* However, researchers preferred to use the theory of gas-film lubrication by solving the non-linear Reynolds equation, which can show accurate pressure distribution in the squeeze film.[13–15] To increase the accuracy of the numerical model, some researchers took different variables into consideration in the theoretical formulation, such as air inertia[16] and edge effect.[17]

Surface properties such as roughness can influence the fluid flow around the levitated object and slightly modify the acoustic field between the radiation plate and the levitated object.[3] In addition, the manufacture and installation error also produce an acoustic viscous force, which affects the stability of the floating object. In NFAL, two methods are commonly used to generate an acoustic viscous force.[18] *The first method is to use the traveling wave sound field in the fluid between the vibrator and the levitated object.*[19,20] The second method is to use the gradient of the sound field in the fluid domain.[21] *Generally, the viscous force produced by the first method can be used to transport and rotate an object*. The stability of an acoustically levitated object

---

[a)] Electronic mail: yuanyuan.liu@tum.de

mainly relates to the viscous force produced by the second method.[22] In 2000, Matsuo *et al.*[23] found that the stability of the levitated object has a close relationship with the magnitude and distribution of a radiator plate vibration. Koike *et al.*[22] used the block-spring model to evaluate the stability of the levitated object and acoustic viscous forces in two directions based on the theory of the near-boundary acoustic streaming. Based on this, Hu *et al.*[18] considered the effect of acoustic streaming outside the boundary layer when calculating the acoustic viscous force. Later, Li *et al.*[24] pointed out that the block-spring system model can only treat small amplitude oscillation because of its linear approximation. They used Stokes micro-continuum theory and acoustic radiation potential method to acquire the restoring force. However, they did not present subsequent experimental results.

The actual pressure distribution describing the fluid motion in the squeeze film cannot be acquired by the above-mentioned methods.[18,22] *Therefore, a different approach for generating mechanism analysis of the restoring force for the floating object is suggested in this paper.* An imaginary grooved reflector is used to solve the discontinuity due to eccentricity in the solving domain. *With the combination of the non-linear Reynolds equation and the levitator motion equation, the pressure distribution is evaluated by using the finite difference method (FDM) and the Newton-Raphson method.* The corresponding restoring force is calculated from the pressure gradient. The numerically evaluated restoring force is verified with experimental data from a specifically constructed testing device. Subsequently, some studies on the influence of various factors such as amplitude of the radiator, weight of the reflector, and vibration mode of the radiator on the restoring force are presented. The study shows that the levitation system becomes more stable in the higher amplitude of the radiator and the weight of the levitator, and in lower order vibration mode.

This paper is organized as follows: in Sec. II, the governing equations of the misaligned squeeze film model is presented. Section III presents the experimental setup that can be used to measure the restoring force at different amplitudes. In Sec. IV, the pressure distribution of the squeeze film, stability analysis of the reflector, and parametric study are presented.

II. GOVERNING EQUATIONS

A. Reynolds equation

The model of the NAFL which considers the eccentricity of the reflector in the cylindrical coordinate system is shown in Fig. 1. The radius of the reflector is the same as the radius of the radiator and is defined as L. O and O_1 are the center of the radiator and the reflector plates, respectively. The distance between O and O_1 is called eccentricity and is defined as e. For the symmetrical model, the centers of radiator and reflector are concentric i.e., $e = 0$. In this condition, the reflector will remain stable in the horizontal direction, and the pressure in the squeeze film can be expressed by the steady Reynolds equation as shown in Ref. 25. However, if the center of the reflector does not coincide with the radiator center, the reflector will perform a damped oscillation in the horizontal direction until it reaches an equilibrium position.[18] Thus, an updated Reynolds equation in the cylindrical coordinate system is derived by using the momentum and continuity equations. In reality, when the reflector is misaligned, it remains inclined relative to the radiator. In order to simplify the numerical model, the effect of the inclination can be neglected for smaller eccentricity.[18,24]

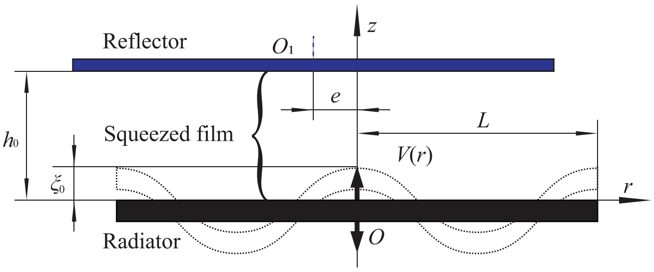

FIG. 1. (Color online) Misaligned squeeze film model in the cylindrical coordinate.

Some assumptions are introduced here to simplify the momentum equations. First, the fluid and flow are treated as Newtonian fluid and laminar flow, respectively. *Second, the pressure gradient in the film thickness direction is neglected since the radius of the plate L is much greater than the mean thickness of the air film* h_0.[26] *However, if the radius and the film thickness are at the same size level, the pressure gradient in the film thickness direction cannot be neglected.*[12] Third, the squeeze film is assumed as an isothermal film due to the small levitation height.[27] Moreover, the fluid inertia force and body force are compared with the viscous force and can be neglected in the lower Reynolds number.[28] Based on these assumptions, the momentum equations in the r- and θ-directions are stated as[29]

$$\rho\left(\frac{\partial v_r}{\partial t}\right) = -\frac{\partial p}{\partial r} + \mu_a \frac{\partial^2 v_r}{\partial z^2}, \tag{1a}$$

$$\rho\left(\frac{\partial v_\theta}{\partial t}\right) = -\frac{1}{r}\frac{\partial p}{\partial \theta} + \mu_a \frac{\partial^2 v_\theta}{\partial z^2}, \tag{1b}$$

where v_r and v_θ are the airflow velocity in the r- and θ-directions, μ_a is the dynamic air viscosity, ρ and p are the density and pressure of air in the squeeze film, respectively. It is assumed that no relative slip exists between the air and the bottom surface of the reflector, and the corresponding velocity profile in the r- and θ-directions is presented with reference to Eq. (1) as[26]

$$v_r = \frac{z}{2\mu_a}\frac{\partial p}{\partial r}(z-h) + \dot{u}\frac{z}{h} + \ddot{u}\frac{\rho z}{6\mu_a h}(z^2 - h^2), \tag{2a}$$

$$v_\theta = \frac{z}{2\mu_a r}\frac{\partial p}{\partial \theta}(z-h) + \dot{\varphi}\frac{zr}{h} + \ddot{\varphi}\frac{\rho z r}{6\mu_a h}(z^2 - h^2), \tag{2b}$$

where u and φ are the relative horizontal displacement and rotation angle of the reflector, and $h = h(r, \theta, t)$ is the corresponding film thickness. Integrating the continuity equation across the squeeze film thickness leads to[30]

$$\int_0^h \left[\frac{\partial \rho}{\partial t} + \frac{\partial (r\rho v_r)}{r \cdot \partial r} + \frac{\partial (\rho v_\theta)}{r \cdot \partial \theta} + \frac{\partial (\rho v_z)}{\partial z}\right] dz = 0, \tag{3}$$

where v_z is the airflow velocity in the z-direction. However, it was assumed earlier that $v_z = 0$. The expressions of airflow velocity in the squeeze film derived in Eq. (2) is substituted into Eq. (3). Then, a dimensionless Reynolds equation in cylindrical coordinates can be expressed as

$$\begin{aligned} &\frac{\partial}{\partial R}\left(RPH^3 \frac{\partial P}{\partial R}\right) + \frac{1}{R} \cdot \frac{\partial}{\partial \theta}\left(PH^3 \frac{\partial P}{\partial \theta}\right) \\ &\quad = \sigma R \cdot \frac{\partial (PH)}{\partial T} + \Lambda_1 \dot{U} \frac{\partial (RPH)}{\partial R} + \Lambda_1 \dot{\varphi} \frac{\partial (RPH)}{\partial \theta} \\ &\qquad + \Lambda_2 \ddot{U} \frac{\partial (RPAH^3)}{\partial R} + \Lambda_2 \ddot{\varphi} \frac{\partial (RPAH^3)}{\partial \theta}, \end{aligned} \tag{4}$$

where, $\sigma = 12\mu_a \omega L^2/p_a h_0^2$, $\Lambda_1 = 6\mu_a L^2/p_a h_0^2$, and $\Lambda_2 = -\rho_a L^2/2p_a$. σ is known as the squeeze number. U is the reflector relative dimensionless horizontal displacement. The dimensionless parameters are stated as

$$\begin{aligned} &R = r/L, \quad H = h/h_0, \quad P = p/p_a, \\ &\quad U = u/L, \quad A = \rho/\rho_a \text{ and } T = \omega \cdot t, \end{aligned}$$

where p_a, ρ_a, and $\omega = 2\pi f$ are ambient air pressure, air density, and angular frequency of excitation, respectively.

B. Boundary conditions

The solution of the squeeze air pressure distribution is based on the cylindrical coordinate system with origin O. The solution domain Ω_{Ra} is equivalent to the area of the radiator, and is defined by the radius of the radiator and enclosed by the boundary $\Gamma(r = L)$, as shown in Fig. 2. The corresponding domain of reflector is enclosed by a circular area of radius L, and defined by Ω_{Re}, as depicted in Fig. 2. Due to the eccentric positioning of the reflector with respect to the radiator, the center of the reflector can be expressed by $O_1(e, \alpha)$. The solution domain Ω_{Ra} is divided into two parts: the overlapping domain of Ω_{Ra} and Ω_{Re} is defined as the squeezed domain $\Omega^s_{Ra}(\Omega^s_{Ra} = \Omega_{Ra} \cap \Omega_{\mathrm{Re}})$, and the remaining part of the radiator domain Ω_{Ra} is stated as the no-squeezed domain Ω^n_{Ra}. The position of O_1 and radius L decide the area of the domain Ω^s_{Ra}. The boundary Γ_s between the domain Ω^s_{Ra} and the domain Ω^n_{Ra} is represented by the thick line in Fig. 2, which is expressed by

$$\begin{aligned} &r = \sqrt{L^2 - [e \cdot \sin(\alpha - \theta)]^2} + e \cdot \cos(\alpha - \theta), \\ &\theta \subseteq \left[\alpha + \arccos\left(\frac{e}{2L}\right) - 2\pi, \alpha - \arccos\left(\frac{e}{2L}\right)\right]. \end{aligned} \tag{5}$$

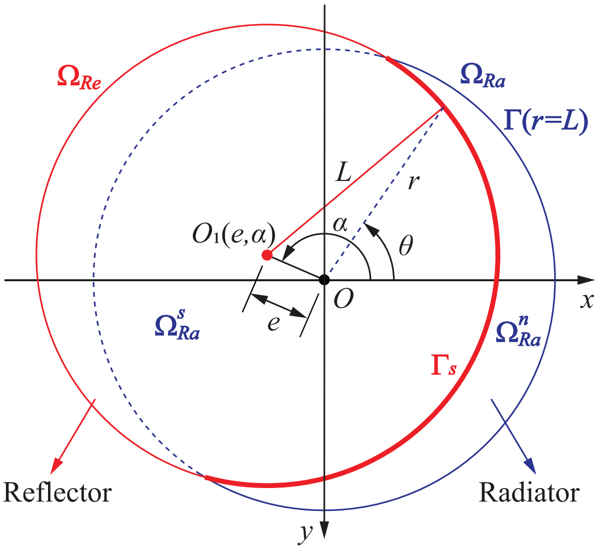

FIG. 2. (Color online) Schematic diagram of the boundary conditions.

Owing to the misalignment of the reflector, the thickness of the no-squeezed domain Ω^n_{Ra} is infinite. Thus, domain Ω^n_{Ra} can be treated as grooved in order to ensure the height of the solving domain can be expressed, as shown in Fig. 3. The depth of the groove is h_g. However, it is assumed that the pressure in this domain always equals the atmospheric pressure.

Therefore, the thickness of the dimensionless air film can be expressed as

$$H = \begin{cases} 1 + \dfrac{\xi_0 \cdot V(r) \cdot \sin T}{h_0} & (r, \theta) \subseteq \Omega^s_{Ra} \\ 1 + \dfrac{\left[\xi_0 \cdot V(r) \cdot \sin T + h_g\right]}{h_0} & (r, \theta) \subseteq \Omega^n_{Ra}, \end{cases} \tag{6}$$

where ξ_0 and $V(r)$ are the maximum vibration amplitude and mode shape of the radiator, respectively, as shown in Fig. 1. The boundary Γ contact with the ambient air implies

$$P|_{\Gamma(R=1)} = 1. \tag{7}$$

The pressure gradient at the center O is zero, which represents

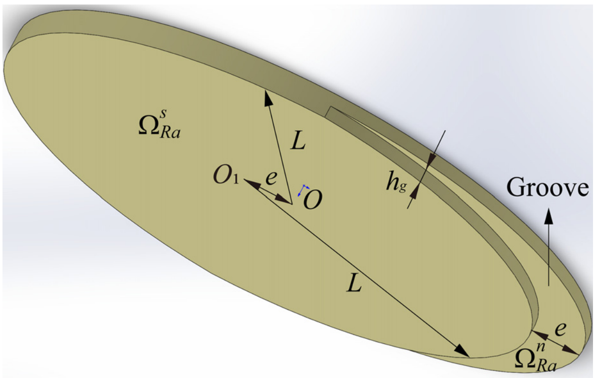

FIG. 3. (Color online) The imaginary reflector with groove.

$$\frac{\partial P}{\partial R}(R=0,T)=0. \tag{8}$$

Initially, the reflector plate is placed on the radiator, where the film thickness equals zero, and the corresponding pressure equals the atmospheric pressure. This can be numerically stated as

$$P(R,T=0)=1, \quad H(R,T=0)=0. \tag{9}$$

The eight-point discrete method is introduced here to decrease the order of the Reynolds equation, due to the existence of the groove.[25,31] Next, the pressure distribution within the solution domain Ω_{Ra} can be obtained by using the Newton-Raphson method.[32,33]

C. Dynamic equations

Three types of forces, such as levitation force $\mathbf{F_z}$, horizontal thrust force $\mathbf{F_t}$, and rotational moment M_r are acting on the reflector plate due to the squeeze film as shown in Fig. 4.

The horizontal thrust force $\mathbf{F_t}$ is referred to as the restoring force, and decomposes into components in the x- and y-directions as $\mathbf{F_x}$ and $\mathbf{F_y}$, respectively. This meets the following condition as $F_t=\sqrt{F_x^2+F_y^2}$. Similarly, the reflector relative horizontal displacement $\mathbf{u}$ decomposes into $\mathbf{u_x}$ and $\mathbf{u_y}$. The relative vertical displacement of reflector is $\mathbf{u_z}$. Thus, the equation of motion for the reflector in matrix form is written as

$$\begin{bmatrix} m & 0 & 0 & 0 \\ 0 & m & 0 & 0 \\ 0 & 0 & m & 0 \\ 0 & 0 & 0 & J \end{bmatrix} \begin{Bmatrix} \ddot{u}_z \\ \ddot{u}_x \\ \ddot{u}_y \\ \ddot{\varphi} \end{Bmatrix} = \begin{Bmatrix} F_z - G \\ F_x - F_{dx} \\ F_y - F_{dy} \\ M_r - M_d \end{Bmatrix}, \tag{10}$$

where m and $J = mL^2/2$ are the mass and moment of inertia of the reflector, respectively. $G = mg$ is the weight of the reflector, and g is the gravitational acceleration. $\ddot{\mathbf{u}}_\mathbf{x}$, $\ddot{\mathbf{u}}_\mathbf{y}$, $\ddot{\mathbf{u}}_\mathbf{z}$, and $\ddot{\varphi}$ are the reflector motion acceleration in the x-, y-, z-, and θ-directions, respectively. $\mathbf{F_{dx}}$ and $\mathbf{F_{dy}}$ are the components of the horizontal drag force $\mathbf{F_d}$ in the x- and y-directions. M_d is the drag rotational moment in θ-direction. $\mathbf{F_{dx}}$, $\mathbf{F_{dy}}$, and M_d originate due to the relative movement between the reflector and surrounding air. The vertical drag force can be neglected due to very small value of $\dot{\mathbf{u}}_\mathbf{z}$.[27] For laminar flow over a flat plate, the drag forces and moment can be written as[34]

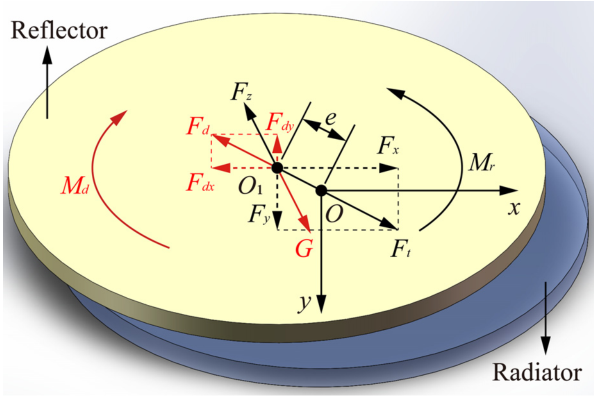

FIG. 4. (Color online) Diagram of forces on the reflector.

$$\begin{Bmatrix} F_{dx} \\ F_{dy} \end{Bmatrix} = \frac{1}{2}\rho_a S \begin{Bmatrix} C_{dx}\dot{u}_x^2 \\ C_{dy}\dot{u}_y^2 \end{Bmatrix}, \tag{11a}$$

$$M_d = \int_0^L \frac{1}{2} C_{d\theta}\rho_a(\dot{\varphi}r)^2 2\pi r \cdot r dr = -\frac{1}{5}\pi C_{d\theta}\rho_a\dot{\varphi}^2 L^5, \tag{11b}$$

where $S = \pi L^2$ is the total surface area in contact with the air; $\dot{\mathbf{u}}_\mathbf{x}$, $\dot{\mathbf{u}}_\mathbf{y}$, and $\dot{\varphi}$ are the relative velocity of reflector in the x-, y-, and θ-directions, respectively. Drag coefficient C_d is expressed as

$$\begin{Bmatrix} C_{dx} \\ C_{dy} \\ C_{d\theta} \end{Bmatrix} = \frac{1}{S}\int_0^L 2\pi \cdot 0.664\sqrt{v_a r} \cdot \begin{Bmatrix} \dot{u}_x \\ \dot{u}_y \\ \dot{\varphi} r \end{Bmatrix}^{-0.5}$$

$$dr = 0.885\sqrt{v_a} \cdot \begin{Bmatrix} L\dot{u}_x \\ L\dot{u}_y \\ 4L^2\dot{\varphi}/9 \end{Bmatrix}^{-0.5}, \tag{12}$$

wherein v_a is the air kinematic viscosity.

As mentioned earlier, the cylindrical coordinate system with origin O (represented by $O - r\theta z$) is used to solve the squeeze air pressure. Therefore, the forces that are calculated in the cylindrical coordinate system $O - r\theta z$ need to decompose into the cylindrical coordinate system $O_1 - r_1\theta_1 z$, as shown in Fig. 5. Except for the squeezed domain Ω_{Ra}^s where there exists a pressure change, all other domains remain in atmospheric air pressure. Shear stresses τ_{zr} and $\tau_{z\theta}$ are developed due to the air flow in the r- and θ-directions, which act on the bottom surface of the reflector and normal to the z-axis. In the coordinate system $O_1 - r_1\theta_1 z$, both τ_{zr} and $\tau_{z\theta}$ have one component in the r_1- and θ_1-directions, respectively. Thus, the mean thrust forces F_x, F_y, and M_r within one cycle can be expressed as

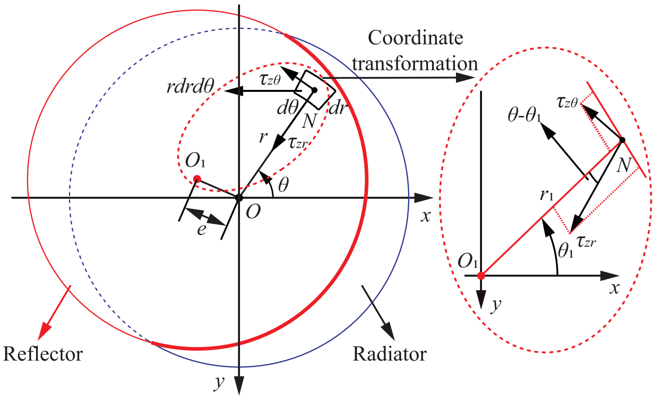

FIG. 5. (Color online) Geometric diagram for the resolution and composition of shear stresses.

$$\begin{bmatrix} F_x \\ F_y \\ M_r \end{bmatrix} = \frac{1}{2\pi}\int_0^{2\pi}\int_0^{2\pi}\int_0^{L} \begin{bmatrix} -\tau_{z\theta}\cos(\theta_1) & -\tau_{zr}\cos(\theta_1) \\ \tau_{z\theta}\sin(\theta_1) & \tau_{zr}\sin(\theta_1) \\ -\tau_{zr}\cdot r_1 & \tau_{z\theta}\cdot r_1 \end{bmatrix} \cdot \begin{bmatrix} \sin(\theta-\theta_1) \\ \cos(\theta-\theta_1) \end{bmatrix} \cdot r dr d\theta dT. \quad (13)$$

This means that the radius between N and O_1 is written as

$$r_1 = \sqrt{r^2 + e^2 - 2re\cos(\alpha - \theta)}, \qquad \theta \subseteq [0, 2\pi], \quad (14)$$

and θ_1 is expressed by

$$\theta_1 = \theta - \arcsin\left[e \cdot \sin(\alpha - \theta)/r_1\right], \qquad \theta \subseteq [0, 2\pi]. \quad (15)$$

For a Newtonian fluid, the shear stresses in the flow act on the surface normal to the z-axis in the cylindrical coordinate system, and are defined by[35]

$$\tau_{zi} = \mu_a\left(\frac{\partial v_z}{\partial i} + \frac{\partial v_i}{\partial z}\right) \cong \mu_a \frac{\partial v_i}{\partial z} \qquad (i = r,\ \theta). \quad (16)$$

Substituting Eq. (2) into Eq. (16) leads to the expression for the shear stresses τ_{zr} and $\tau_{z\theta}$ on the bottom surface of the reflector, which is stated as

$$\tau_{zr}\big|_{(z=h)} = \mu_a \frac{\partial v_r}{\partial z}\bigg|_{(z=h)} = \frac{h}{2}\frac{\partial p}{\partial r} + \mu_a \frac{\dot{u}}{h} + \frac{\rho h \ddot{u}}{3}, \quad (17a)$$

$$\tau_{z\theta}\big|_{(z=h)} = \mu_a \frac{\partial v_\theta}{\partial z}\bigg|_{(z=h)} = \frac{h}{2r}\frac{\partial p}{\partial \theta} + \mu_a \frac{\dot{\varphi} r}{h} + \frac{\rho h \ddot{\varphi} r}{3}. \quad (17b)$$

It is observed from Eq. (17) that the shear stresses mainly depend on the pressure gradient and the relative movement of the reflector. The levitation force F_z is the integral of pressure in the solution domain, which is stated as[17]

$$F_z = \frac{1}{2\pi}\int_0^{2\pi}\int_0^{2\pi}\int_0^{L} (p - p_a) \cdot r dr d\theta dT. \quad (18)$$

III. EXPERIMENTAL MEASUREMENT

In order to measure the relationship between eccentricity and restoring force, based on the same transducer and radiator as presented in Ref. 25, a new reflector plate is used. It is made of AL2024 and has the same diameter as the radiator. The diameter of the radiator is 120 mm. The thickness and weight of this plate are 3 mm and 0.9244 N, respectively. Generally, the restoring force is very small, i.e., on the order of milli-Newton (mN).[20] *The measurement method which utilizes a voice coil motor (VCM) can be used to acquire the small force.*[36,37] *This measurement method has the benefit of high repeatability and accuracy. However, the measurement system is very complex. As another experimental methodology stated in Refs. 19 and 20, a universal tilting indexing disk is used to approximately measure the restoring force.* This experiment has been conducted here to validate the proposed numerical model. The experimental setup is shown in Fig. 6 and consists of a universal tilting indexing disk, transducer, and the corresponding control unit. Furthermore, a digital single-lens reflex camera is installed for monitoring the levitation performance of the plate. The transducer is fixed on the universal tilting indexing disk, which can be tilted at a certain angle β by adjusting the control system. Therefore, when the reflector is levitated, the eccentricity e is adjusted until the restoring force F_t and the corresponding weight component $mg\sin\beta$ balance each other. The span of the experimental restoring force is decided by the resolution ratio of the tilting indexing disk. In this experiment, the minimum angle β is $20'$, which corresponds to the minimum weight component 5.378 mN. Figure 6 shows the photograph of the reflector plate in the levitation state when $\beta = 1°20'$ and the amplitude is ξ_0=16.9 μm.

Since the reflector remains in the stable state throughout every measurement, the two centers O and O_1 can simultaneously locate on the x-axis, which means $\alpha = \pi$. Therefore, the solution domain and boundary conditions are symmetric with respect to the x-axis. The pressure distribution also remains symmetric about the x-axis. Moreover, the reflector remains stationary during the measurement; the thrust force F_y and rotational moment M_r are equal to zero. Therefore, the restoring force F_t of Eq. (13) can be simplified to

$$F_t = F_x = \frac{1}{2\pi}\int_0^{2\pi}\int_0^{2\pi}\int_0^{L} -[\tau_{zr}\cos(\theta - \theta_1)] \cdot r\cos(\theta_1) dr d\theta dT = \text{mg}\sin\beta. \quad (19)$$

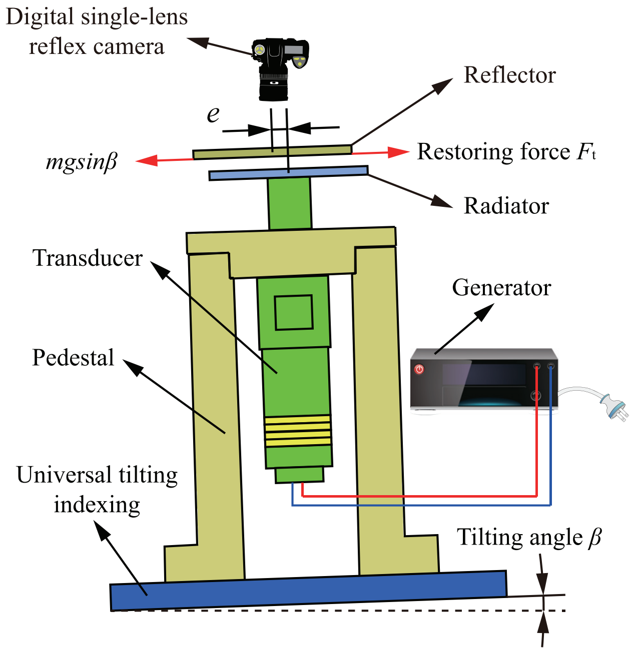

FIG. 6. (Color online) Schematic diagram of experimental measurement system.

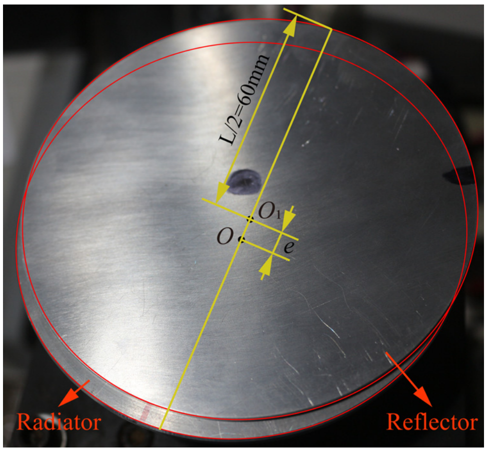

FIG. 7. (Color online) Photograph of the reflector plate in the levitation state.

IV. RESULTS AND DISCUSSIONS

A. Pressure distribution

Table I lists the main parameters of the levitation system and its operating conditions The pressure distribution in the cylindrical coordinate system $O-r\theta z$ at the starting time of one stable cycle is shown in Fig. 8(a). *The effect of the computational domain mesh-density on the numerical results has been checked. Considering the time cost and convergence, the computational domain* Ω_{Ra} *is divided into* 60×40 *grids.*[25] The excitation amplitude, levitation force, and eccentricity are 16.9 μm, 0.9244 N, and 10 mm, respectively. The radiator works in its second-order vibration mode, which indicates the excitation frequency being equal to 19 kHz. Since the vibration mode shape of the radiator is considered in the gas film thickness expression, the shape of the pressure distribution corresponds to the mode shape in the squeezed domain Ω^s_{Ra}. Due to the boundary condition as stated in Eq. (7), the pressure distribution shows a wave crest near the boundary. The pressure distribution is symmetrical about the x-direction, whereas it is asymmetrical about the y-direction. Thus, the pressure distribution meets the conditions while deriving Eq. (19). If the eccentricity equals zero, the pressure distribution will be symmetrical in the squeezed domain as shown in Ref. 25, and the reflector will keep a stable state. In the non-squeezed domain Ω^n_{Ra}, the dimensionless pressure value equals 1, which means that the pressure is the same as the atmospheric pressure. Thus, the imaginary groove will not affect the real pressure distribution in the squeezed domain.

Based on the pressure distribution in Fig. 8(a), the restoring force can be calculated by the coordinate transformation of the shear force as described in Eq. (19). Therefore, the restoring force distribution in the x-axis at two different eccentricities can be seen in Fig. 8(b). The solid line corresponds to eccentricity $e = 10$ mm; the dotted line corresponds to concentric condition, $e = 0$ mm. It is noted that the shape of the restoring force distribution has a close relationship with the mode shape, which is more likely the derivative of the mode shape. This is due to the restoring force, which is related to $\partial p/\partial r$ as shown in Eq. (17a). The outermost zero-point corresponds to the wave crest that is near the boundary in Fig. 8(a). In the concentric condition, the restoring force value is always centrosymmetric about point O. Consequently, the restoring force always equals zero, which means the reflector will keep its stationary state in the horizontal direction. However, for $e = 10$ mm and the time step equal to 80, corresponding to the starting time of one stable cycle, the asymmetric pressure distribution [cf. Fig. 8(a)] caused the asymmetric restoring force distribution. Since the eccentricity is 10 mm, the curve of the restoring force becomes discontinuous in the vicinal position of x equal to –10 mm. Compared with the dotted line, the missing negative part on the right side, which is due to the eccentricity, will break the centrosymmetry. Thus, the positive part is larger than the negative part, and the direction of the restoring force points toward the positive x-direction. In the time step that is equal to 190, corresponding to the half time of one stable cycle, the restoring force distribution indicates the squeezed air will produce a force that makes the reflector move to the left. Thus, the restoring force alternates between positive and negative during one cycle, which can be seen in Fig. 8(c). The maximum positive restoring force absolute value is 0.5897 N, which is larger than the negative absolute value 0.4865 N. Therefore, the mean restoring force value at one cycle is 31.7 mN and points to the opposite direction of eccentricity. Therefore, four important factors will affect the restoring force distribution: the amplitude and weight of the reflector mainly affect the magnitude, the mode affects the shape, and the eccentricity affects the degree of asymmetry.

Figure 9 shows the effect of groove height (cf. Fig. 3) on the levitation and restoring forces. It is observed from Fig. 9 that the levitation and restoring forces vary significantly at the lower value of h_g. If the h_g is greater than 0.5 mm, then the numerical results remain the same. Thus, the groove depth is set at 0.6 mm in this study.

B. Stability analysis

In general, eccentricity is the most important factor affecting restoring force distribution. A comparison of

TABLE I. Main parameters of the levitation system and its operating conditions.

Parameter	SI unit	Parameter	SI unit
Air temperature	20 °C	Air dynamic viscosity (μ_a)	1.81×10^{-5} Pa·s
Radius (L)	60 mm	Ambient air pressure (p_a)	1.013×10^{5} Pa
Excitation frequency (f)	19 kHz	Air kinematic viscosity (ν_a)	1.51×10^{-5} m^2/s
Air density (ρ_a)	1.204 kg/m^3	Weight of the reflector plate	0.9244 N

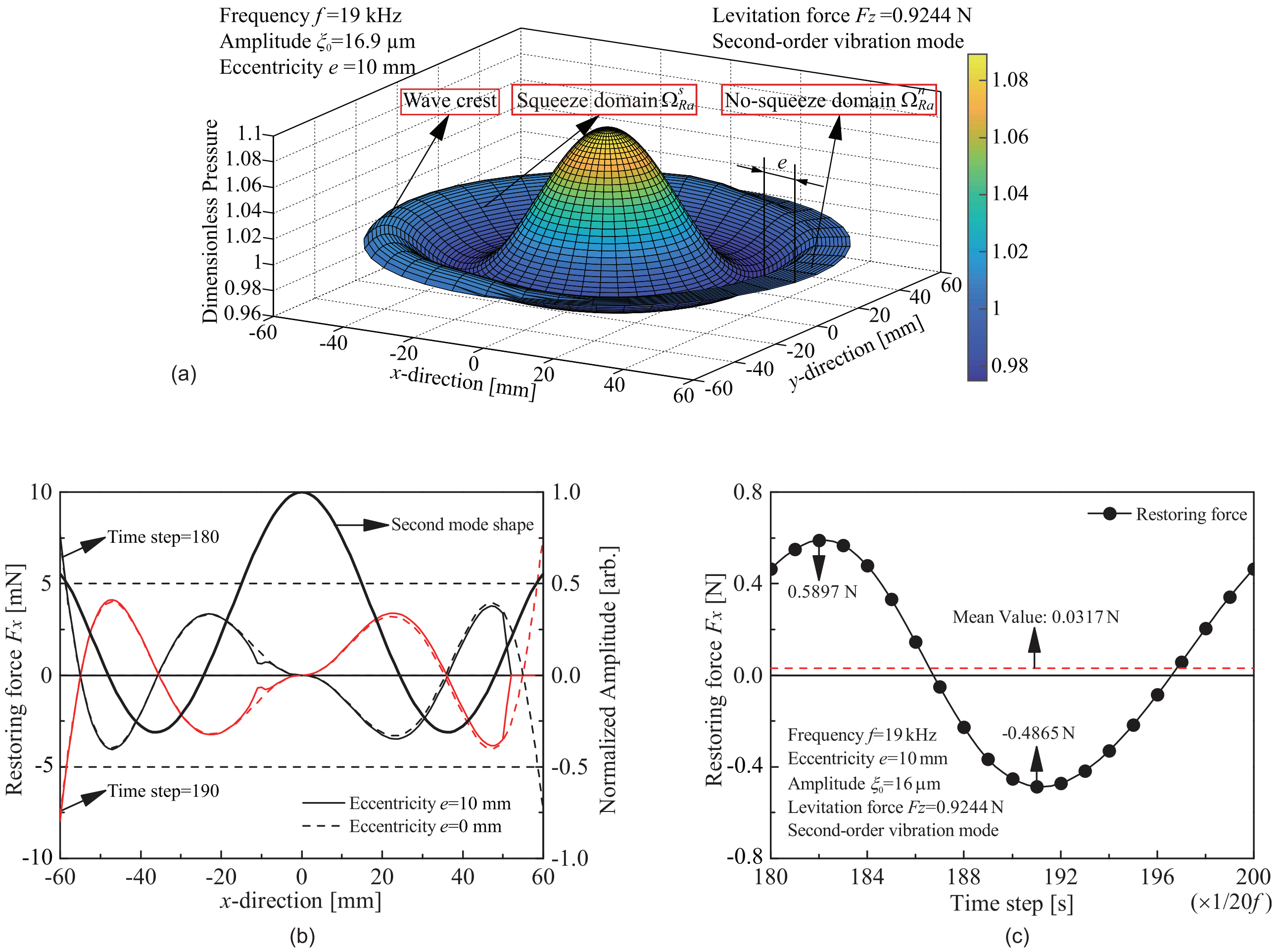

FIG. 8. (Color online) (a) Pressure distribution in solving domain Ω_{Ra}, (b) restoring force distribution in the *x*-axis, and (c) restoring force versus one cycle time.

numerical and experimental results of restoring force at various eccentricities is presented in Fig. 10(a). Notably, the numerical results have exhibited reasonably good agreement with the experimental results in lower eccentricity. The fact that this is due to the inclination of the reflector is neglected in this study. In the lower eccentricity, the effect of inclination is very small. However, with the increment in eccentricity, the inclination became an important factor that affects the stability of the reflector. In two different excitation amplitudes, the restoring force increases with the increment in eccentricity. It is noted that the growth gradient decreases with the increment in eccentricity. So, the relationship between the restoring force and the eccentricity is exponential, and the index is less than 1. The same variation tendency has also been reported in Ref. 18.

The changes in restoring force within one cycle at various eccentricity are shown in Fig. 10(b). As shown, the positive restoring force part is greater than the negative restoring force part. Thus, the average restoring force throughout one cycle is positive, which indicates that the direction of the restoring force is acting opposite to the eccentricity. It clearly indicates that the maximum restoring force value increases with increasing eccentricity. This phenomenon is depicted in Fig. 10(a).

C. Parametric study

1. Amplitude

In the same levitation force, the excitation amplitude exerts a significant influence on the pressure value. Therefore, the magnitude of the restoring force distribution is affected by the vibration amplitude. Figure 11 shows the variation of the restoring force with the increment in the excitation amplitude for $f = 19\,\text{kHz}$ and eccentricity $e = 10\,\text{mm}$. The restoring force increases as the vibration amplitude increases. The relationship between amplitude and restoring force maintains a linear trend. In Ref. 23, the experimental results also present a similar trend. It is observed from Fig. 11 that the restoring force increases with the increment in the levitation force. However, a non-linear relationship exists between the restoring and levitation forces. A detailed discussion is presented in Sec. IV C 2.

2. Weight of the reflector

When the reflector maintains a stable levitation condition, then the levitation force equals the weight of the reflector. This means that the magnitude of the pressure is determined by the weight of the reflector in the same

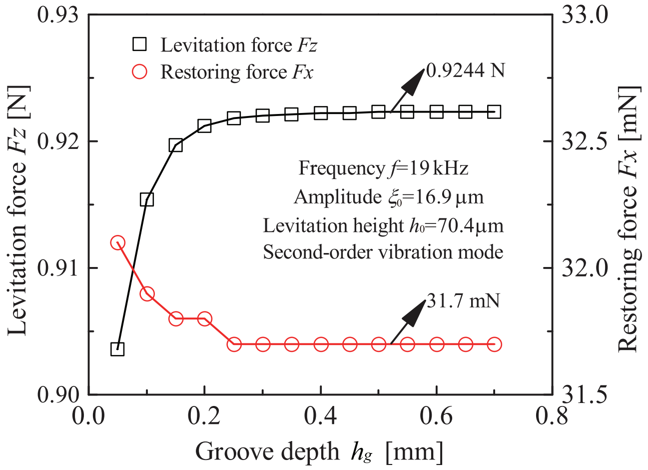

FIG. 9. (Color online) Dependence of the numerical results on the imaginary groove depth.

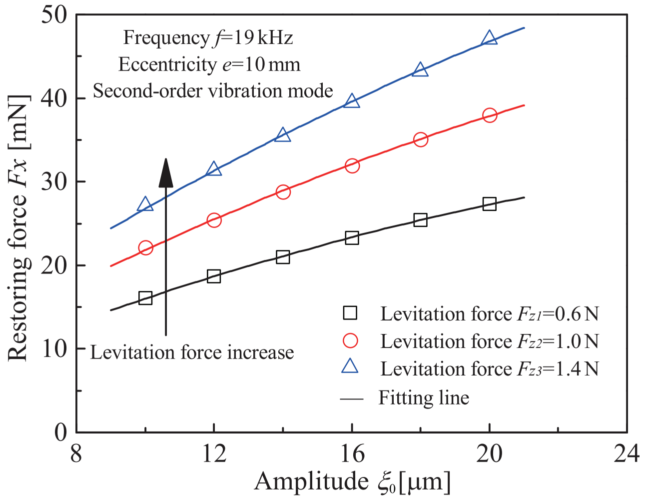

FIG. 11. (Color online) The restoring force versus amplitude at different levitation forces.

amplitude. The dependence of the restoring force on the weight of the reflector is investigated at three excitation amplitudes and is illustrated in Fig. 12. The excitation frequency and eccentricity are set as $f = 19$ kHz and $e = 10$ mm, respectively. It is clearly shown that the restoring force increases as weight increases. However, the relationship between the restoring force and weight is non-linear. The growth gradient of restoring force decreases with the increment in the weight. This result is in accordance with the result in Ref. 18. In the same amplitude, the higher weight of the reflector indicates that the pressure value is greater, which implies that the pressure gradient is also greater. As mentioned in Sec. IV A, the restoring force mainly depends on the pressure gradient. Therefore, the restoring force value will be higher. In Ref. 23, the experimental results show that the restoring force increases with the decrease in levitation height. The reasons for this nonlinear phenomenon are due to the existence of a non-linear relationship between levitation force and levitation height.[38]

3. Mode shape

Another factor that can affect the pressure distribution is the radiator vibration mode. The variation in the restoring force with eccentricity in the first three order modes is shown in Fig. 13. *The driving frequencies which excite the first three order modes are 7150, 19 000, and 37 200 Hz, respectively. In order to study the effect of the vibration mode on the restoring force, the other variables are kept constant except for the driving frequency and vibration mode shape*. The maximum vibration amplitude ξ_0 and levitation force F_z are considered 16 μm and 1 N, respectively. Likewise, as shown in Fig. 10(a), the restoring force increases with the increment in eccentricity. It is observed from Fig. 13 that the restoring force value is at a maximum in the first-order mode and a minimum in the third-order mode. The reason for this phenomenon may be due to the levitation system having a larger load-carrying capacity in the third-order mode.[24] Therefore, the levitation height will

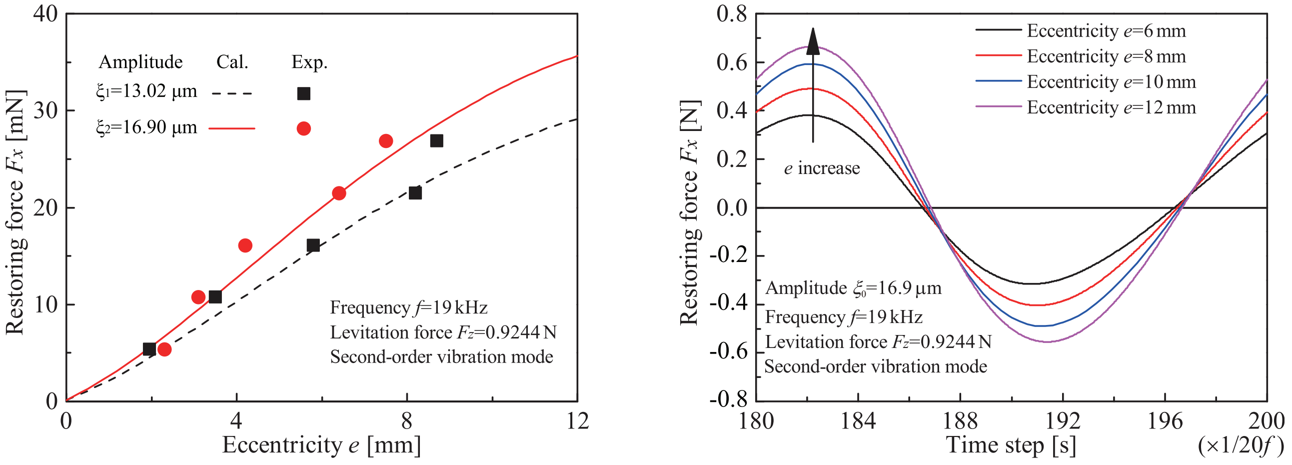

(a)

(b)

FIG. 10. (Color online) (a) Comparisons of the restoring force versus eccentricity between the numerical and experimental results under two different amplitudes; (b) restoring force versus one cycle time at different amplitudes.

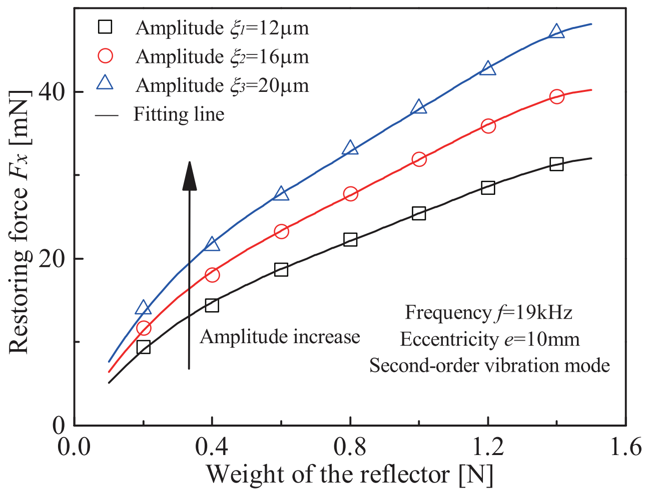

FIG. 12. (Color online) The restoring force versus weight of the reflector at different amplitudes.

be higher in the third-order mode at the same condition levitation force and excitation amplitude. Accordingly, the restoring force has a smaller value in the third-order mode. The comparison with two other order modes indicates that the growth gradient in the third-order mode is smaller. Since the difference between the restoring force in the first- and the second-order modes is small, the load-capacity in the second-order mode is larger. *Therefore, the fact that the radiator works in second-order mode seems beneficial for the given parameters and operating conditions.*

V. CONCLUSIONS

This paper has presented a different numerical methodology for acquiring restoring force. Initially, a Reynolds equation considering the movement of the reflector has been derived. The expression of levitation height has been substituted into the Reynolds equation to obtain the pressure distribution by using FDMs. Subsequently, the restoring force acting on the reflector has been calculated by using the coordinate transformation. Numerical results show that the restoring force increases with the increment in eccentricity. There is an exponential relationship between the restoring force and the eccentricity with an index less than 1. Furthermore, the experimental setup has been developed to support the numerical analysis. The numerical results represent a solid agreement with the experimental results. It can be observed that the relationship between the amplitude of the radiator and the restoring force maintains a positive linear trend and the restoring force increases with the increment in the weight of the reflector. Therefore, a stable levitation system can be developed by increasing the excitation amplitude and the weight of the reflector. Moreover, the restoring force in the first-order mode is greater than the restoring force in the second- and third-order modes. However, the operation of the levitation system in the second-order mode is recommended due to the higher load capacity over the first-order mode. The accomplishment of this research is to provide guidance when encountering instability of floating objects in the industrial application of NAFL.

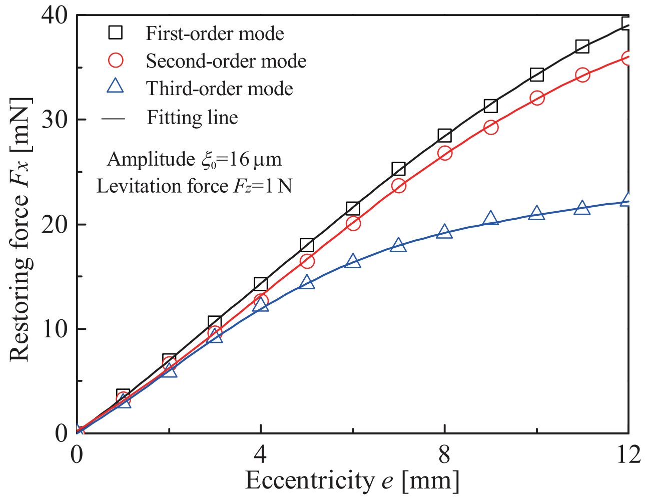

FIG. 13. (Color online) Comparisons of the restoring force versus eccentricity at different mode shapes.

ACKNOWLEDGMENTS

The first author acknowledges the support provided by the China Scholarship Council (CSC) (File No. 201808340068).

[1] F. Erzincanli, J. Sharp, and S. Erhal, "Design and operational considerations of a non-contact robotic handling system for non-rigid materials," Int. J. Mach. Tool. Manuf. **38**(4), 353–361 (1998).

[2] O.-S. Kim, S.-H. Lee, and D.-C. Han, "Positioning performance and straightness error compensation of the magnetic levitation stage supported by the linear magnetic bearing," IEEE. Trans. Ind. Electron. **50**(2), 374–378 (2003).

[3] V. Vandaele, P. Lambert, and A. Delchambre, "Non-contact handling in microassembly: Acoustical levitation," Precis. Eng. **29**(4), 491–505 (2005).

[4] S. Ueha, Y. Hashimoto, and Y. Koike, "Non-contact transportation using near-field acoustic levitation," Ultrasonics **38**(1), 26–32 (2000).

[5] T. Ide, J. Friend, K. Nakamura, and S. Ueha, "A non-contact linear bearing and actuator via ultrasonic levitation," Sens. Actuat. A Phys. **135**(2), 740–747 (2007).

[6] D. Ha, T. Stolarski, and S. Yoshimoto, "An aerodynamic bearing with adjustable geometry and self-lifting capacity. Part 1: Self-lift capacity by squeeze film," Proc. Inst. Mech. Eng. J. Part J **219**(1), 33–39 (2005).

[7] S. Zhao, S. Mojrzisch, and J. Wallaschek, "An ultrasonic levitation journal bearing able to control spindle center position," Mech. Syst. Signal. Process. **36**(1), 168–181 (2013).

[8] K. Feng, M. Shi, T. Gong, Y. Liu, and J. Zhu, "A novel squeeze-film air bearing with flexure pivot-tilting pads: Numerical analysis and measurement," Int. J. Mech. Sci. **134**, 41–50 (2017).

[9] Y. Hashimoto, Y. Koike, and S. Ueha, "Acoustic levitation of planar objects using a longitudinal vibration mode," J. Acoust. Soc. Jpn. E **16**(3), 189–192 (1995).

[10] Y. Wada, D. Koyama, and K. Nakamura, "Finite-element analysis of acoustic streaming generated between a bending transducer and a reflector through second-order approximated forces," Acoust. Sci. Technol. **34**(5), 322–331 (2013).

[11] Y. Wada, T. Kundu, and K. Nakamura, "Mesh-free distributed point source method for modeling viscous fluid motion between disks vibrating at ultrasonic frequency," J. Acoust. Soc. Am. **136**(2), 466–474 (2014).

[12] Y. Wada, D. Koyama, and K. Nakamura, "Acoustic streaming in an ultrasonic air pump with three-dimensional finite-difference time-domain

analysis and comparison to the measurement," Ultrasonics **54**(8), 2119–2125 (2014).

[13] A. Minikes, I. Bucher, and S. Haber, "Levitation force induced by pressure radiation in gas squeeze films," J. Acoust. Soc. Am. **116**(1), 217–226(2004).

[14] A. Almurshedi, M. Atherton, C. Mares, and T. Stolarski, "Modelling influence of Poisson's contraction on squeeze film levitation of planar objects," J. Appl. Phys. **125**, 095303 (2019).

[15] Y. Fan, M. Miyatake, S. Kawada, B. Wei, and S. Yoshimoto, "Inertial effect on gas squeeze film for large radius disc excited by standing waves with complex modal shapes," Int. J. Mod. Phys. B **33**(24), 1950282 (2019).

[16] T. Stolarski and W. Chai, "Inertia effect in squeeze film air contact," Tribol. Int. **41**(8), 716–723 (2008).

[17] J. Li, W. Cao, P. Liu, and H. Ding, "Influence of gas inertia and edge effect on squeeze film in near field acoustic levitation," Appl. Phys. Lett. **96**(24), 243507 (2010).

[18] J. Hu, K. Nakamura, and S. Ueha, "Stability analysis of an acoustically levitated disk," IEEE Trans. Ultrason. Ferr. **50**(2), 117–127 (2003).

[19] J. Saito, J. Friend, K. Nakamura, and S. Ueha, "Resonant mode design for noncontact ultrasonic motor with levitated rotor," Jpn. J. Appl. Phys. **44**(6B), 4666–4668 (2005).

[20] D. Koyama, K. Nakamura, and S. Ueha, "A stator for a self-running, ultrasonically-levitated sliding stage," IEEE Trans. Ultrason. Ferr. **54**(11), 2337–2343 (2007).

[21] J. Hu, G. Li, H. Chan, and C. Choy, "A standing wave-type noncontact linear ultrasonic motor," IEEE Trans. Ultrason. Ferr. **48**(3), 699–708 (2001).

[22] Y. Koike, S. Ueha, A. Okonogi, T. Amano, and K. Nakamura, "Suspension mechanism in near field acoustic levitation phenomenon," in *Proceedings of the 2000 Ultrasonics Symposium*, San Juan, Puerto Rico (October 22–25, 2000), pp. 671–674.

[23] E. Matsuo, Y. Koike, K. Nakamura, S. Ueha, and Y. Hashimoto, "Holding characteristics of planar objects suspended by near-field acoustic levitation," Ultrasonics **38**(1–8), 60–63 (2000).

[24] J. Li, P. Liu, H. Ding, and W. Cao, "Nonlinear restoring forces and geometry influence on stability in near-field acoustic levitation," J. Appl. Phys. **109**(8), 084518 (2011).

[25] W. Li, Y. Liu, and K. Feng, "Modelling and experimental study on the influence of surface grooves on near-field acoustic levitation," Tribol. Int. **116**, 138–146 (2017).

[26] A. Minikes and I. Bucher, "Noncontacting lateral transportation using gas squeeze film generated by flexural traveling waves—Numerical analysis," J. Acoust. Soc. Am. **113**(5), 2464–2473 (2003).

[27] A. Minikes and I. Bucher, "Coupled dynamics of a squeeze-film levitated mass and a vibrating piezoelectric disc: Numerical analysis and experimental study," J. Sound. Vib. **263**(2), 241–268 (2003).

[28] T. Stolarski and W. Chai, "Self-levitating sliding air contact," Int. J. Mech. Sci. **48**(6), 601–620 (2006).

[29] S. Mohite, V. Sonti, and R. Pratap, "A compact squeeze-film model including inertia, compressibility, and rarefaction effects for perforated 3-D MEMS structures," J. Microelectromech. Syst. **17**(3), 709–723 (2008).

[30] B. J. Hamrock, S. R. Schmid, and B. O. Jacobson, *Fundamentals of Fluid Film Lubrication*, 2nd ed. (CRC Press, Boca Raton, FL, 2004), Chap. 6, pp. 165–167.

[31] S.-K. Chen, H.-C. Chou, and Y. Kang, "Stability analysis of hydrodynamic bearing with herringbone grooved sleeve," Tribol. Int. **55**(2), 15–28 (2012).

[32] H. Heshmat, J. Walowit, and O. Pinkus, "Analysis of gas-lubricated foil journal bearings," J. Lubr. Technol. **105**(4), 647–655 (1983).

[33] K. Feng, Y. Liu, and M. Cheng, "Numerical analysis of the transportation characteristics of a self-running sliding stage based on near-field acoustic levitation," J. Acoust. Soc. Am. **138**(6), 3723–3732 (2015).

[34] R. W. Fox, A. T. McDonald, and P. J. Pritchard, *Fox and McDonald's Introduction to Fluid Mechanics*, 8th ed. (John Wiley & Sons, New York, 2011), Chap. 9, pp. 445–448.

[35] F. A. Morrison, *An Introduction to fluid Mechanics* (Cambridge University Press, New York, 2013), Chap. 5, pp. 369–379.

[36] K. Uchiage, Y. Ishino, M. Takasaki, and T. Mizuno, "Enlargement of floater size in ultrasonic suspension by arranging the shape of vibrating surface," in *Proceedings of the 2014 IEEE International Ultrasonics Symposium*, Chicago, IL (September 3–6, 2014), pp. 2510–2513.

[37] M. Takasaki, S. Chino, Y. Kato, Y. Ishino, and T. Mizuno, "Actuation force measurement mechanism for non-contact ultrasonic suspension," Key Eng. Mater. **523–524**, 727–732 (2012).

[38] P. Liu, J. Li, H. Ding, and W. Cao, "Modeling and experimental study on near-field acoustic levitation by flexural mode," IEEE Trans. Ultrason. Ferr. **56**(12), 2679–2685 (2009).

Publication B

Yuanyuan Liu, Xiaodong Sun, Kian K. Sepahvand, and Steffen Marburg

Theoretical analysis on the static and dynamic performances of a squeeze film air journal bearing with three separate pads structure

in International Journal of Mechanical Sciences, Volume 200, 2021, pp. 106442, DOI: https://doi.org/10.1016/j.ijmecsci.2021.106442.

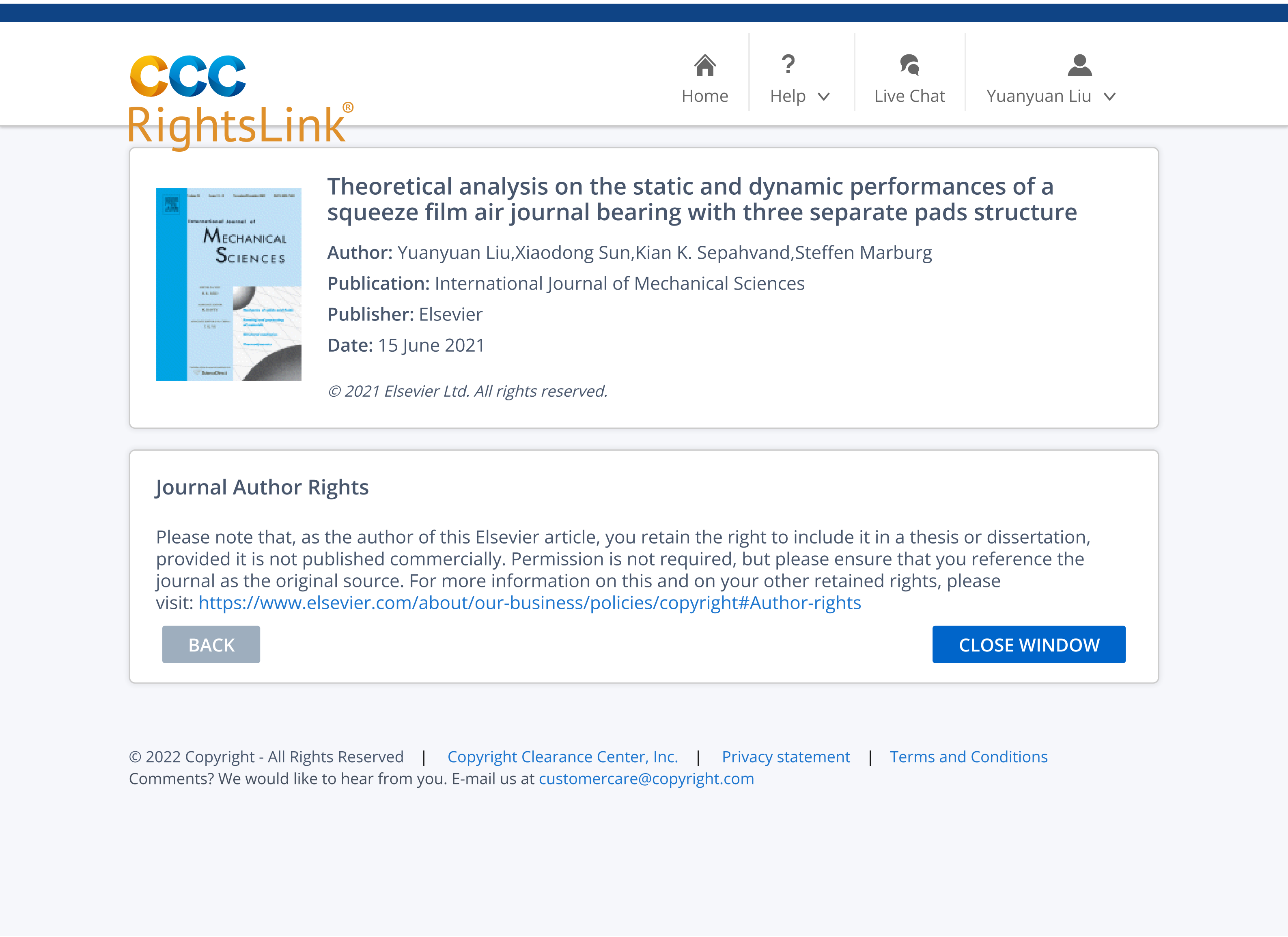

Theoretical analysis on the static and dynamic performances of a squeeze film air journal bearing with three separate pads structure

Author: Yuanyuan Liu,Xiaodong Sun,Kian K. Sepahvand,Steffen Marburg

Publication: International Journal of Mechanical Sciences

Publisher: Elsevier

Date: 15 June 2021

© 2021 Elsevier Ltd. All rights reserved.

Journal Author Rights

Please note that, as the author of this Elsevier article, you retain the right to include it in a thesis or dissertation, provided it is not published commercially. Permission is not required, but please ensure that you reference the journal as the original source. For more information on this and on your other retained rights, please visit: https://www.elsevier.com/about/our-business/policies/copyright#Author-rights

International Journal of Mechanical Sciences 200 (2021) 106442

Contents lists available at ScienceDirect

International Journal of Mechanical Sciences

journal homepage: www.elsevier.com/locate/ijmecsci

Theoretical analysis on the static and dynamic performances of a squeeze film air journal bearing with three separate pads structure

Yuanyuan Liu*, Xiaodong Sun, Kian K. Sepahvand, Steffen Marburg

Chair of Vibro-acoustics of Vehicles and Machines, Technical University of Munich, Boltzmann Str. 15, Garching 85748, Germany

ARTICLE INFO

Keywords:
Squeeze film bearings
Three-pad structure
Equilibrium position
Dynamic coefficients

ABSTRACT

Owing to their distinct non-contact and oil-free characteristics, squeeze film air bearings have been introduced to satisfy ultra-precision, low wear, and ultra-clean requirements. This paper proposes an analytical model of a three-pad squeeze film bearing to study its static and dynamic performance. The bearing force is calculated by integrating the pressure distribution over the bearing surface, which is governed by the Reynolds equation. The stable equilibrium position of the rotor is obtained by the Newton-Raphson method. A numerical method to acquire the bearing dynamic coefficients is originally proposed by considering the vibration of its pad. These dynamic coefficients are determined by solving the perturbation equations derived from the combination of the Reynolds equation and the modified film thickness and pressure. The predicted static and dynamic results show good agreement with experimental results. The parameter study shows that the variation in eccentricity with respect to the rotational speed can be controlled by reasonably adjusting the vibration amplitude or the nominal clearance of the bearing. In addition, the results indicate that the direct stiffness and damping coefficients are increased by decreasing the rotation speed or increasing the vibration amplitude of the bearing pad.

1. Introduction

With the development of turbomachinery, the demand for bearings meeting high-precision and high-speed requirements has increased. Air-lubricated bearings have the advantages of high speed, low cost, and weak heat generation due to the inherently low viscosity of air [1–3]. In addition, their oil-free character eliminates the fluid contamination and is friendly for the environment [4,5]. These features enable their use in turbocompressors, inertial gyroscopes, and turbochargers etc. [6–9] Generally, there are three mechanisms of the high-pressure gas in an air bearing, namely aerodynamic, aerostatic, and squeeze effects [10]. For pure aerodynamic bearings [11–13], since the aerodynamic effect is not evident at a low rotation speed, friction and wear for the bearing and rotor will happen during run-up and shutdown [14]. Aerostatic bearings [15–17] are used to address these issues, as they can provide external force to resist the weight of the rotor at low speed. However, aerostatic bearings require an additional air compressor to provide clean air with high pressure so that the bearing becomes noisy and costly. Among the non-contact techniques, near-field acoustic levitation (NFAL) has several inherent advantages, such as no material limit of the levitator, the compactness of the system and its high load capacity [18,19]. Accordingly, squeeze film bearings (SFBs) which bring NFAL technology into the gas film bearing has been introduced to meet the requirements of low wear and high precision.

The SFB is actually a kind of hybrid gas-lubricated bearing. When the rotation speed equals zero, the pure squeeze effect produces the levitation force to support the rotor [20]. At a certain rotation speed, the squeeze and aerodynamic effects simultaneously influence the film pressure distribution. In 1964, Salbu [21] has introduced the SFB models. Since then, the study of SFB has drawn much attention [22–24]. In 2004, Ha et al. [25] proposed an SFB with elastic hinges and three piezoelectric plates. They studied the influence of the oscillating amplitude and frequency of the bearing on the load-carrying capacity by numerical and experimental methods. However, the paper only considered the squeeze effect without considering the aerodynamic effect. In addition, several different structures for SFB, such as tubular [26], three-lobe [27] and flexure pivot-tilting pad bearings [28] have been proposed. Stolarski et al. [29] studied the acoustic levitation performance of three SFBs with different structures. The experimental results showed that the geometry of the bearing has an important influence on the acoustic levitation effect. Moreover, the material [30,31], operating mode [32], and installation location [28] of the bearing are additional factors which affect the load-carrying capacity. However, such bearings [25–32] have an evident drawback which is insufficient load-carrying capacity. In studies of the acoustic levitation, it was found that the load-carrying capacity increases with the increment of the structure vibration amplitude [33,34]. Compared with the piezoelectric plate used to generate the vibration [25–32], the Langevin ultrasonic transducer can produce a higher vibration amplitude due to its excellent electro-acoustic efficiency and high input power [35]. Thus, Zhao et al. [35,36] proposed a novel active non-contact journal bearing which utilizes three Langevin

---

* Corresponding author.
E-mail address: yuanyuan.liu@tum.de (Y. Liu).

https://doi.org/10.1016/j.ijmecsci.2021.106442
Received 22 February 2021; Received in revised form 21 March 2021; Accepted 6 April 2021

Nomenclature

c	nominal clearance
e	eccentricity displacement
f	vibration frequency
h	film thickness
i	number of the pad
k	number of iterations
n	rotation speed of the rotor
p	film pressure
p_a	ambient air pressure
r	rotor radius
t	time
$\bar{t} = \upsilon t$	dimensionless time (whirl)
x, y, z	cartesian coordinate space
$C_{xx}, C_{xy}, C_{yy}, C_{yx}$	dynamic damping coefficients
F	bearing force
$\bar{F}$	mean bearing force
$H = h/c$	dimensionless film thickness
H_0	dimensionless thickness in the equilibrium position
$K_{xx}, K_{xy}, K_{yy}, K_{yx}$	dynamic stiffness coefficients
L	bearing length
O	bearing center
O_r	rotor center
$P = p/p_a$	dimensionless film pressure
R	bearing radius
$T = \omega_f t$	dimensionless time (steady-state)
$V_i(\theta,z)$	normalized mode shape
W	external load
μ_a	air dynamic viscosity
υ	perturbation angular velocity
ξ_i	maximum vibration amplitude
θ	cylindrical space coordinates
θ_0	attitude angle
θ_{ia}	pad arc length
θ_{im}	pad middle angle
σ	squeeze number
$\omega = 2\pi \bullet n/60$	rotation angular velocity
$\omega_f = 2\pi f$	vibration angular velocity
$\Delta x,\ \Delta y,\ \Delta\dot{x},\ \Delta\dot{y},$	perturbation variables
$\Delta X,\ \Delta Y,\ \Delta\dot{X},\ \Delta\dot{Y},$	dimensionless perturbation variables
Λ	bearing number

transducers as the bearing structure. There are two benefits to this structure. On the one hand, it has a higher load capacity (up to 51 N) than the above-mentioned bearings [25–32]. On the other hand, the vibration of each pad is controllable individually such that the position of the rotor can be adjusted. However, the study failed to analyze the static and dynamic performance of the bearing under different running parameters, which is extremely important for the design and application of this kind of SFB.

The static performance of SFBs has been studied by many researchers [25,28,37]. Several different methods were used to analyze the squeeze effect, e.g., acoustic radiation theory [33], Computational Fluid Dynamics (CFD) model [38] and gas-film lubrication theory [20]. To investigate the dynamic performance of SFBs, many researchers adopted the orbit simulation method as their analysis technique [39–42]. For instance, based on the SFB proposed by Ha et al. [25], Stolarski [43] investigated the dynamic response of a rotor supported by squeeze film pressure at a low rotation speed numerically and experimentally. The results show that the squeeze effect does not only improve the self-generated squeeze-film capacity but also increases the threshold speed of instability. In addition, the stability of the bearing could be improved by increasing the external load. Feng et al. [44] found the same results by numerical analysis. In addition, they pointed out that the influence of the squeeze effect on the critical speed of the rotor is weak for heavy external loads. The orbit simulation method is carried out by coupling the equations of motion of the rotor and the fluid governing equations. Although this method can directly judge the stability of the rotor, it also will result in higher computational costs compared to other analytical methods [43]. For example, Beck and Strodtman [45] used variational and numerical techniques to analyze the stability of SFB. However, their analytical model is just assumed as a single-degree-of-freedom model. In the field of gas-lubricated bearings, many researchers have used a set of stiffness and damping coefficients to study the dynamic characteristics of the bearing [46–49]. The dynamic coefficients are calculated based on the assumption of linearized bearing forces, and they are applied in the critical speed and unbalance response calculation [46,50]. The structure of the SFBs vibrates continuously whereas the bearing structure of other types of air journal bearings [1,47,51] is stable in the steady state. The film thickness and pressure distributions of the SFBs need to be adjusted taking into account the vibration of the structure. Therefore, it is worth studying the dynamic characteristics of the SFBs by using the dynamic coefficients.

This paper addresses the static and dynamic characteristics of a three-pad SFB. A simplified theoretical analysis model based on the bearing in [36] is proposed. Combining the non-linear Reynolds equation and the boundary equations, the pressure distribution between the bearing and the rotor is acquired. The bearing forces are calculated by integrating the pressure. The steady eccentricity ratio and the attitude angle of the rotor are obtained by using the Newton-Raphson method. Next, using the perturbation method, a set of modified partial differential equations is derived from the Reynolds equation. The eight dynamic coefficients are calculated from these differential equations. The static and dynamic numerical methods are validated by comparing the predicted and experimental results in the same operating conditions. Subsequently, the influences of various factors such as the external load, rotation speed, nominal clearance and vibration amplitude on the static equilibrium position of the rotor are investigated. The influences of rotation speed and vibration amplitude on the dynamic coefficients are studied. The effect of each pad on the static and dynamic performances of the bearing is investigated as well.

2. Analytical model

The schematic diagram of the three-pad SFB proposed in [36] is shown in Fig. 1a. The bearing mainly consists of three Langevin ultrasonic transducers. Three concave radiation surfaces compose the inner face of the bearing. *The machine bore diameter of the concave surfaces equals the bearing bore diameter.* According to the piezoelectric effect, the four piezoelectric transducer (PZT) plates generate the same frequency vibration along the through-thickness direction when a sinusoidal voltage is applied at a certain frequency f. The air between the concave surfaces and the outer surface of the rotor is squeezed continuously. Consequently, the levitation force acting on the rotor is produced by the squeeze effect.

The analytical model of the bearing, as shown in Fig. 1b, is employed to analyze its running performance in this study. Three Langevin ultrasonic transducers are simplified to three pads with the same vibration characteristics. Two assumptions in the analysis process are considered: (I) since the Langevin transducer has enough radial and tilting stiffnesses, it is assumed that the motion of the pad is not affected by the squeeze air pressure; (II) the vibration amplitude of each pad is treated as uniform in both the circumferential and axial direction. The center point, the inner radius and the width of the bearing are defined as O, R and L, respectively. The center point and outer radius of the rotor are denoted as O_r and r, respectively. The nominal clearance of the bearing is defined as $c = R - r$. The distance between O and O_r is denoted as eccentricity displacement e, which consists of two components e_x and e_y in

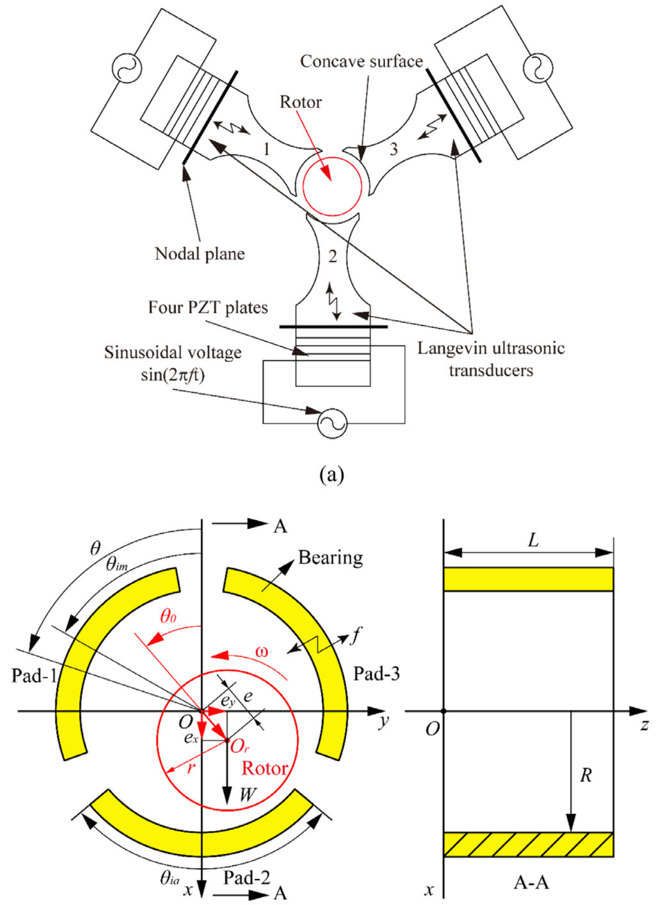

(b)

Fig. 1. (a) Schematic diagram of the SFB [36], where the three concave radiation surfaces compose the inner face of the bearing. (b) Simplified analysis model of the bearing and coordinate systems, where the three Langevin ultrasonic transducers are simplified to three pads.

the x- and y-direction, respectively. The rotation axis of the bearing coincides with the z-axis. The angle between the static load direction and the connection line between the rotor and bearing centers is denoted by the attitude angle θ_0. The static external load Wmay originate from the weight of the rotor or magnetic force, etc. acting on the rotor.

3. Theoretical analysis method

3.1. Reynolds equation

The Reynolds equation is widely employed to calculate the pressure in the fluid film of the aerodynamic bearings or SFBs [28,52,53]. The major assumptions in this paper are the same as those used in other gas-bearing analysis [50]. Firstly, it is assumed that the flow in the gas film is isothermal. Secondly, inertia and body forces are neglected. Thirdly, the flow is assumed to be laminar. In the cylindrical coordinate system shown in Fig. 1b, the expression of the dimensionless steady Reynolds equation considering the aerodynamic and the squeeze effect simultaneously is written as [43,44]

$$\frac{\partial}{\partial\theta}\left(PH^3\frac{\partial P}{\partial\theta}\right)+\frac{\partial}{\partial Z}\left(PH^3\frac{\partial P}{\partial Z}\right)=\Lambda\frac{\partial(PH)}{\partial\theta}+\sigma\frac{\partial(PH)}{\partial T}, \tag{1}$$

where P and H are the dimensionless air film pressure and thickness, respectively. T is the dimensionless time. The dimensionless groups are introduced as

$$P=p/p_a,\ H=h/c,\ Z=z/R,\ T=\omega_f\cdot t=2\pi f\cdot t,\ \omega=2\pi\cdot n/60.$$

Herein, p and h are the air film pressure and thickness, respectively. p_a denotes the pressure of ambient air, and n is the rotation speed of the rotor. The bearing number Λ characterizes the self-acting aerodynamic pressure generated by the rotation of the rotor at an angular velocity ω, which is given by

$$\Lambda=\frac{6\mu_a\omega}{p_a}\left(\frac{R}{c}\right)^2, \tag{2}$$

where μ_a is the viscosity coefficient of ambient air. The squeeze number σ stands for the self-acting squeeze film pressure generated by the cycling vibration of the pad at an angular velocity ω_f, which is given by

$$\sigma=\frac{12\mu_a\omega_f}{p_a}\left(\frac{R}{c}\right)^2. \tag{3}$$

3.2. Boundary conditions and film thickness

Due to the continuity of the pressure at the interface to the ambient air, the pressure on both end faces of the bearing in the z-direction meets the condition

$$P(\theta,z=0\&L)=1. \tag{4}$$

As shown in Fig. 1b, the arc length and middle angle of the i^{th} pad are defined by θ_{ia} and θ_{im}, respectively. The two ends of each pad in the circumferential direction are also in contact with the ambient air, which means

$$P\left(\theta_{im}\pm\theta_{ia}/2,z\right)_{|(i=1,2,3)}=1. \tag{5}$$

It is assumed that the rotor is rigid and well-balanced. The film thickness between the outer face of the rotor and the inner face of the bearing consists of three parts: the nominal clearance c, eccentricity e, and the radial displacement resulting from the vibration of each pad. Therefore, the film thickness is expressed by

$$h=c+e_y\cdot\mathbf{sin}\,(\theta)+e_x\cdot\mathbf{cos}(\theta)+\xi_i\cdot V_i(\theta,z)\cdot\mathbf{sin}\,\left(\omega_f\cdot t\right), \tag{6}$$

where ξ_i and $V_i(\theta,z)$ correspond to the maximum vibration amplitude and the normalized mode shape for the i^{th} pad. The normalized mode shape $V_i(\theta,z)$ equals 1 in this study, due to the above-mentioned assumption (II), i.e., the uniform vibration amplitude in the circumferential and axial direction. Unlike other compliant structure air bearings [54], the eccentricity displacement can exceed the nominal clearance. The maximum eccentricity is the difference between the bearing clearance c and the maximum vibration amplitude ξ, as all pads vibrate continuously. The rotor turns unstably, if the eccentricity exceeds the threshold of $c-\xi$.

Combining Eqs. (1)–(3) with the boundary value problem stated by Eqs. (4)–(6), the pressure distribution is determined by using the finite difference method (FDM) and the Newton-Raphson technique [55,56].

3.3. Bearing force and attitude angle

The bearing forces are acquired by integrating the pressure over the bearing surface [47]. The pressure distribution is expressed in the cylindrical coordinate system. Consequently, the bearing forces of the SFB in Cartesian coordinates are calculated by

$$F_x=p_aR^2\cdot\sum_{i=1}^{3}\int_0^{L/R}\int_{\theta_{im}-\theta_{ia}/2}^{\theta_{im}+\theta_{ia}/2}(P-1)\cdot\mathbf{cos}(\theta)d\theta dZ, \tag{7}$$

$$F_y=p_aR^2\cdot\sum_{i=1}^{3}\int_0^{L/R}\int_{\theta_{im}-\theta_{ia}/2}^{\theta_{im}+\theta_{ia}/2}(P-1)\cdot\mathbf{sin}\,(\theta)d\theta dZ, \tag{8}$$

$$F=\sqrt{{F_x}^2+{F_y}^2}, \tag{9}$$

where F_x and F_y are the components of the bearing force F in the x- and y-direction, respectively. Notably, the bearing force is a periodic function in time with the frequency f, as reported in [28]. The average

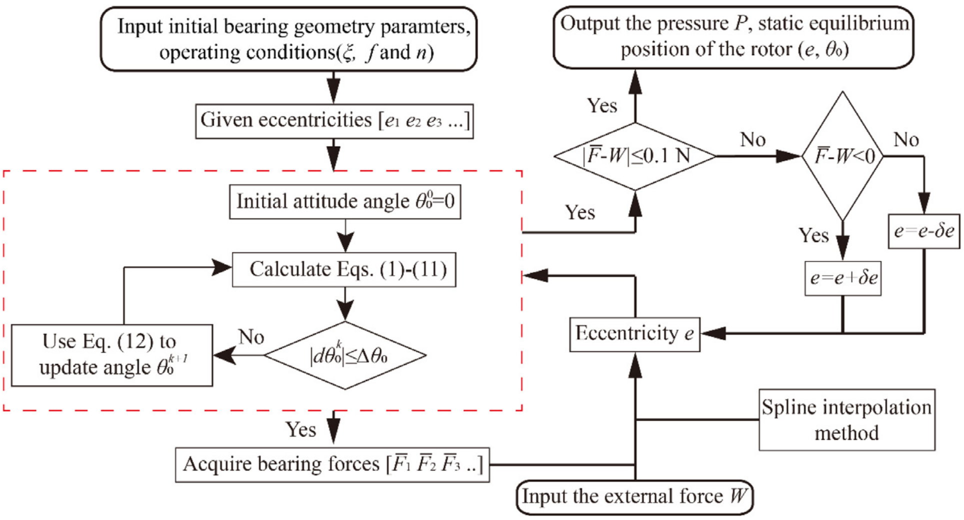

Fig. 2. Flowchart of the static performance calculation, where the Newton-Raphson method described in the dashed box is employed to determine the attitude angle θ_0.

value of the bearing force in one cycle equals the mean bearing force $\bar{F}$ [43]. *As the rotor remains in a steady condition, the mean horizontal bearing force $\bar{F}_y$ equals zero and the mean vertical bearing force $\bar{F}_x$ is counteracting the external load, i.e.,*

$$\bar{F}_x = \frac{1}{2\pi}\int_0^{2\pi} F_x dT = W, \bar{F}_y = \frac{1}{2\pi}\int_0^{2\pi} F_y dT = 0, \mathbf{arctan}\left(\bar{F}_y/\bar{F}_x\right) = 0, \theta_0 = \mathbf{arctan}\left(e_y/e_x\right) \tag{10}$$

An error function is defined as

$$d\theta_0^k = \mathbf{arctan}\left(\bar{F}_y/\bar{F}_x\right), \tag{11}$$

where k represents the number of iterations. The Newton-Raphson iteration method is employed to update the attitude angle [57]

$$\theta_0^{k+1} = \theta_0^k - \frac{d\theta_0^k}{\left(d\theta_0^k - d\theta_0^{k-1}\right)}\left(\theta_0^k - \theta_0^{k-1}\right). \tag{12}$$

The calculation is carried out until the convergence criterion $|d\theta_0^k| \le \Delta\theta_0$ is fulfilled, where $\Delta\theta_0$ stands for the convergence threshold. In this study, $\Delta\theta_0$ is set to 1.7×10^{-3} rad. θ_0^k is considered as the attitude angle θ_0. A flowchart of the static performance calculation procedure is presented in Fig. 2. The correction factor δe is employed to adjust the eccentricity in the case where the mean bearing force does not equal the external load up to a deviation of 0.1 N. The eccentricity correction factor is set to 0.001c in this paper.

3.4. Dynamic coefficients

There are several methods to calculate the stiffness and damping coefficients. Among them, there are the infinitesimal perturbation method [47], the finite perturbation method [58] and the finite volume method [59]. The infinitesimal perturbation method is a common method adopted by many researchers [8,51,60]. This method assumes that infinitesimal displacement perturbations (Δx, Δy) and velocity perturbations ($\Delta\dot{x}$, $\Delta\dot{y}$) are applied to the steady operating conditions. Thus, the modified dimensionless film thickness $\bar{H}$ and pressure $\bar{P}$ are rewritten as [61]

$$\bar{H} = H_0 + \Delta H = H_0 + \Delta X\,\mathbf{cos}(\theta) + \Delta Y\,\mathbf{sin}\,(\theta), \tag{13}$$

$$\bar{P} = P_0 + \Delta P = P_0 + P_x\Delta X + P_y\Delta Y + P_{\dot{x}}\Delta\dot{X} + P_{\dot{y}}\Delta\dot{Y}, \tag{14}$$

in which H_0 and P_0 are the dimensionless film thickness and pressure in the equilibrium position, respectively. $\Delta X = \Delta x/c$,$\Delta Y = \Delta y/c$, $\Delta\dot{X} = \Delta\dot{x}/c$ and $\Delta\dot{Y} = \Delta\dot{y}/c$ are the normalized perturbation variables. P_x, P_y, $P_{\dot{x}}$ and $P_{\dot{y}}$ are the normalized perturbation pressures caused by the perturbation variables Δx, Δy, $\Delta\dot{x}$ and $\Delta\dot{y}$, respectively. In perturbation analysis, the rotor orbits about the equilibrium position with the whirl angular velocity υ. The dimensionless Reynolds equation considering the perturbation motion of the rotor is expressed as

$$\frac{\partial}{\partial\theta}\left(\bar{P}\bar{H}^3\frac{\partial\bar{P}}{\partial\theta}\right) + \frac{\partial}{\partial Z}\left(\bar{P}\bar{H}^3\frac{\partial\bar{P}}{\partial Z}\right) = \Lambda\frac{\partial\left(\bar{P}\bar{H}\right)}{\partial\theta} + 2\Lambda\gamma\frac{\partial\left(\bar{P}\bar{H}\right)}{\partial\bar{t}}, \tag{15}$$

where $\bar{t} = \upsilon t$ is the normalized time. $\gamma = \upsilon/\omega$ is the ratio of the whirl angular velocity and the rotation angular velocity. In this study, setting γ to 1 corresponds to when the whirl frequency equals the rotation frequency, which is also called the synchronous condition. In the equilibrium position, the dimensionless film thickness H_0 and pressure P_0 are periodic functions in time with frequency f. Generally, the pad vibration frequency f (> 20 kHz) is much greater than the whirl frequency (1 kHz correspond to 60 krpm). Thus, the variation rates of film thickness and pressure in the equilibrium position are approximately equal to zero, i.e., $\partial H_0/\partial\bar{t} \approx 0$ and $\partial P_0/\partial\bar{t} \approx 0$. This approximation is not reasonable if the vibration frequency of the pads and the whirl frequency of the rotor are of the same order of magnitude.

Substituting Eqs. (13) and (14) into Eq. (15), the terms with the same coefficients are then collected, yielding four differential equations:

$$\frac{\partial}{\partial\theta}\left(P_0H_0^3\frac{\partial P_\zeta}{\partial\theta}\right) + \frac{\partial}{\partial\theta}\left(P_\zeta H_0^3\frac{\partial P_0}{\partial\theta}\right) + \frac{\partial}{\partial Z}\left(P_0H_0^3\frac{\partial P_\zeta}{\partial Z}\right) + \frac{\partial}{\partial Z}\left(P_\zeta H_0^3\frac{\partial P_0}{\partial Z}\right) = \Lambda\frac{\partial P_xH_0 + \partial P_0\,\mathbf{cos}\,\theta}{\partial\theta} - 2\Lambda\gamma P_{\dot{x}}H_0 - \frac{\partial}{\partial\theta}\left(3P_0H_0^2\,\mathbf{cos}\,\theta\frac{\partial P_0}{\partial\theta}\right) - \frac{\partial}{\partial Z}\left(3P_0H_0^2\,\mathbf{cos}\,\theta\frac{\partial P_0}{\partial Z}\right)\zeta = \mathrm{x}, \tag{16}$$

$$= \Lambda\frac{\partial P_{\dot{x}}H_0}{\partial\theta} + 2\Lambda\gamma\left(P_0\,\mathbf{cos}\,\theta + P_xH_0\right)\zeta = \dot{x}, \tag{17}$$

$$= \Lambda\frac{\partial P_yH_0 + \partial P_0\mathbf{sin}\,\theta}{\partial\theta} - 2\Lambda\gamma P_{\dot{y}}H_0 - \frac{\partial}{\partial\theta}\left(3P_0H_0^2\,\mathbf{sin}\,\theta\frac{\partial P_0}{\partial\theta}\right) - \frac{\partial}{\partial Z}\left(3P_0H_0^2\,\mathbf{sin}\,\theta\frac{\partial P_0}{\partial Z}\right)\zeta = y, \tag{18}$$

$$= \Lambda\frac{\partial P_{\dot{y}}H_0}{\partial\theta} + 2\Lambda\gamma\left(P_0\,\mathbf{sin}\,\theta + P_yH_0\right) \qquad \zeta = \dot{y}. \tag{19}$$

The boundary conditions are stated as

$$P_x = P_y = P_{\dot{x}} = P_{\dot{y}} = 0 \qquad \mathbf{at}\ z = 0\&L, \tag{20}$$

$$P_x = P_y = P_{\dot{x}} = P_{\dot{y}} = 0 \qquad \mathbf{at}\ \theta = \theta_{im} \pm \theta_{ia}/2(i = 1, 2, 3). \tag{21}$$

Table 1
Basic parameters of the SFB and its operating conditions.

Parameters	Value	Unit
Rotor radius r	24.97	mm
Bearing bore radius R	25	mm
Bearing nominal clearance c	30	μm
Bearing width L	25	mm
Pad number i	1,2,3	
Pad arc length θ_{ia}	100°; 100°; 100°	
Pad middle angle θ_{im}	60°; 180°; 300°	
Pad vibration amplitudes $\xi_i (i = 1, 2, 3)$	15	μm
Excitation frequency f	20	kHz
Air dynamic viscosity μ_a	1.81×10^{-5}	Pa•s
Ambient air pressure p_a	1.013×10^{5}	Pa

H_0 and P_0 are calculated by using the proposed calculation procedure as presented in Fig. 2. P_x and $P_{\dot{x}}$are calculated from Eqs. (16) and (17). Similarly, P_y and $P_{\dot{y}}$ are estimated from Eqs. (18) and (19). *Notably, the normalized perturbation pressures* $P_\zeta(\zeta = x, y, \dot{x}, \dot{y})$ *are periodic functions in time with vibration frequency f. Consequently, the time-averaged stiffness and damping coefficients of the bearing within one vibration period are obtained from*

$$\begin{bmatrix} K_{xx} & K_{xy} \\ K_{yx} & K_{yy} \end{bmatrix} = \sum_{i=1}^{3} \frac{1}{2\pi} \int_0^{2\pi} \int_0^{L/R} \int_{\theta_{im}-\theta_{ia}/2}^{\theta_{im}+\theta_{ia}/2} \begin{bmatrix} P_x \cos\theta & P_y \cos\theta \\ -P_x \sin\theta & -P_y \sin\theta \end{bmatrix} \frac{P_a R^2}{c} d\theta dZ dT, \tag{22}$$

$$\begin{bmatrix} C_{xx} & C_{xy} \\ C_{yx} & C_{yy} \end{bmatrix} = \sum_{i=1}^{3} \frac{1}{2\pi} \int_0^{2\pi} \int_0^{L/R} \int_{\theta_{im}-\theta_{ia}/2}^{\theta_{im}+\theta_{ia}/2} \begin{bmatrix} P_{\dot{x}} \cos\theta & P_{\dot{y}} \cos\theta \\ -P_{\dot{x}} \sin\theta & -P_{\dot{y}} \sin\theta \end{bmatrix} \frac{P_a R^2}{c\omega} d\theta dZ dT \tag{23}$$

4. Results and discussion

4.1. Pressure distribution

The basic parameters of the SFB and its operating conditions are listed in Table 1. In this study, if there is no specific clarification, the vibration amplitudes of the three pads are given by the same value. The total computational domain is the area corresponding to the three pads. The effects of the computational domain mesh density on the numerical results have been checked. The results are not presented here for the sake of brevity. To find a compromise between computational efficiency and accuracy, a mesh of each pad area is used which consists of 50 by 25 grid points in the θ- and z-directions, respectively.

Rotation speed, eccentricity and attitude angle are set to 0 krpm, 0.2c and 0°, respectively. Other calculation parameters are listed in Table 1. The time-average dimensionless pressure distribution of one steady excitation circle is plotted in Fig. 3a. It is clearly shown that the time-average pressure is higher than the ambient pressure. The bearing force produced by the squeeze effect can levitate the rotor even at rest. The pressure in pad-2 is higher than that in the other two pads since the rotor is closer to this pad at the equilibrium position. Therefore, the vibration property of pad-2 is more important than that of the other two pads. The pressure distribution is symmetric about the x-O-z plane. Thus, only the vertical bearing force is produced in these conditions.

The comparison of the time-average dimensionless pressure distribution of the mid-plane ($z = L/2$) in the z-direction between the rotor at rest and rotation speed n=20 krpm is shown in Fig. 3b. Setting the rotation speed to n=20 krpm, the pressure is simultaneously influenced by squeeze and aerodynamic effects. Thus, the pressure distribution turns asymmetric, which is different from the situation under the pure squeeze effect. Both, vertical and horizontal bearing forces will be generated. While the pressure in pad-1 increases, it decreases in pad-3. The pressure in pad-2 hardly changes compared to the state with the rotor at rest.

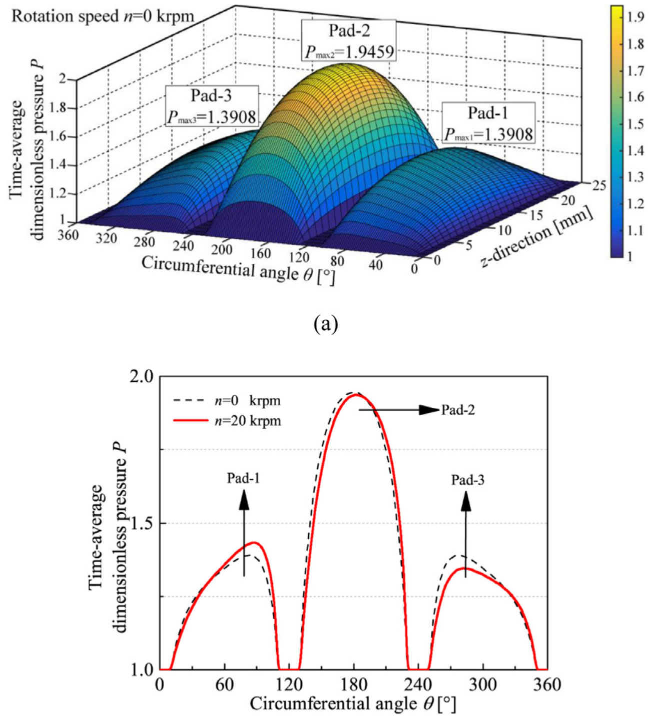

(a)

(b)

Fig. 3. (a) Time-average dimensionless pressure distribution of one period, computed for n=0, e=0.2c and θ_0=0°, where the three crests correspond to the three pads. (b) The pressure distribution of the mid-plane in z-direction at two different rotation speeds, computed for e=0.2c and θ_0=0°, where the solid and dashed lines represent n=20 and 0 krpm, respectively.

By integrating the pressure over the area of all pads in one period, the transient vertical bearing force F_x *and the horizontal bearing force* F_y *are determined when the rotor is at rest and the rotation speed n=20 krpm, as shown in Fig. 4a and b, respectively.* With the rotor at rest, the mean bearing force in the x-direction $\bar{F}_x = -37.4335$N. The negative sign of the bearing force means the direction of $\bar{F}_x$ is opposite to the positive direction of the x-axis. In y-direction, the mean bearing force $\bar{F}_y = 0$N. The total bearing force $\bar{F}$ results from the squeeze effect and is equal to the mean bearing force $\bar{F}_x$. This corresponds to the results presented in Fig. 3a.

When the rotation speed n=20 krpm, the bearing force F_x is slightly lower than for the case of the rotor at rest. Therefore, the mean bearing force in the x-direction $\bar{F}_x$ is slightly decreased and equals -36.9127 N. The mean bearing force in the y-direction $\bar{F}_y$ is generated by the aerodynamic effect and equals 1.5643 N. However, the value of the bearing force $\bar{F}$ in this condition is 36.9458 N and hence, lower than the value for the resting rotor (37.4335 N). Thus, the load-carrying capacity is weakened by the aerodynamic effect given the design parameters of the bearing and the corresponding operating conditions. This contradicts the results that suggest the aerodynamic effect could enhance the bearing load-carrying capacity in other SFBs [42,44]. One possible reason for the contradictory impact of the aerodynamic effect could be the increased magnitude of the vibration amplitude, compared to the results given in [42,44]. In these studies, the change in pressure is mainly caused by the aerodynamic effect. However, Fig. 3b shows that the squeeze effect is the main reason for the high pressure at high vibration amplitudes. Another type of a hybrid air-lubricated bearing, namely the aerostatic bearing, shows similar characteristics. In the case of low

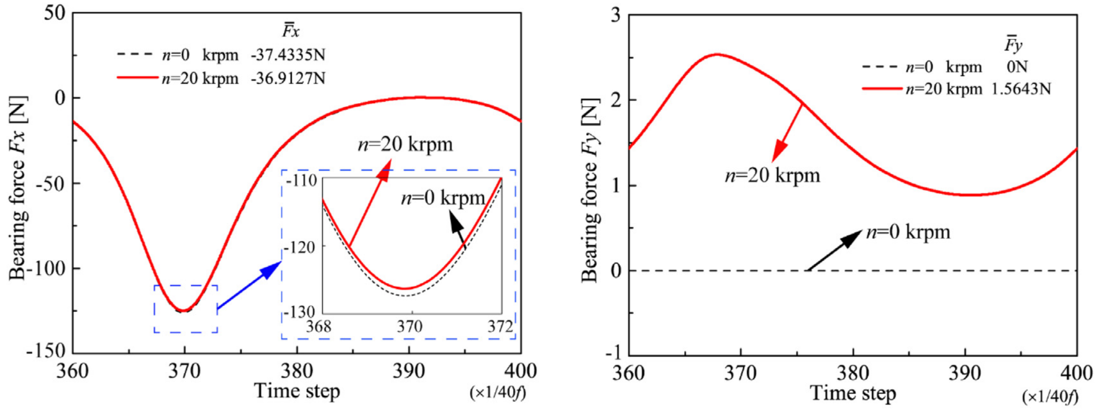

(a) (b)

Fig. 4. Transient bearing forces over one period at two different rotation speeds, computed for e=0.2c and θ_0=0°, where the solid and dashed lines represent n=20 and 0 krpm, respectively. (a) vertical force; (b) horizontal force.

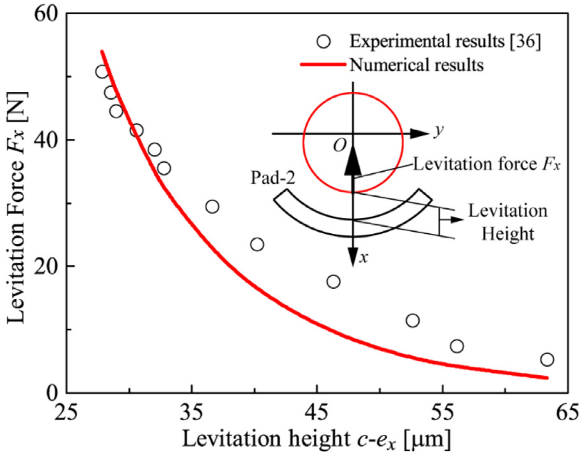

Fig. 5. Comparison between the numerical and the published experimental [36] results, where the solid line represents the numerical results and the circles are the published experimental data.

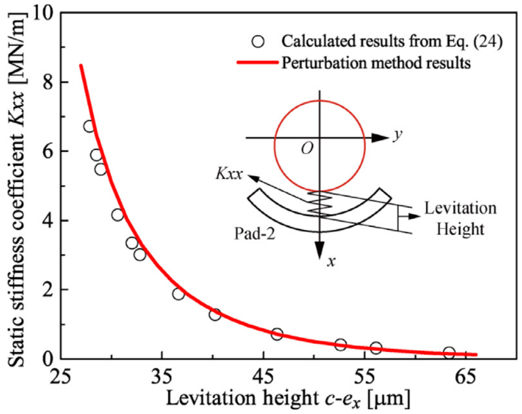

Fig. 6. Comparison between the static stiffness coefficient K_{xx} calculated by the perturbation method and Eq. (24), where the solid line represents the perturbation method results and the circles are the results calculated by Eq. (24).

supply pressure, the aerodynamic effect could enhance the bearing capacity [1]. In the case of high supply pressure, the increment in rotation speed could promote the aerodynamic effect that weakens the bearing capacity [62].

4.2. Validation with experimental data

To validate the proposed static analysis method, the experimental operating parameters from [36] are adopted and used to calculate the static levitation force. The maximum vibration amplitude of the pad and the rotation speed are set to 20 μm and 0 krpm, respectively. All other parameters remain the same as listed in Table 1. Meanwhile, only one transducer (corresponding to pad-2 in this study) was working during the experimental measurement. The comparison between the numerical results from this study and the experimental results from [36] is shown in Fig. 5. The solid line represents the numerical results, while the circles stand for the published experimental data. The levitation force decreases with the increment in levitation height. This phenomenon is commonly found in NFAL [33,63]. The numerical results match well with the experimental data, although there are small deviations at large levitation heights. To conclude, the proposed static analysis method proves to be a viable tool for the prediction of the bearing force.

When the rotor is not rotating, the static stiffness coefficient K_{xx} can be calculated using the proposed perturbation method (Section 3.4). *Alternatively, the static stiffness coefficient can also be calculated from the validated static analysis method, i.e., on behalf of a finite perturbation method [58] actually being a central finite difference scheme, which is expressed by*

$$K_{xx} = \frac{\partial \bar{F}_x}{\partial x} \approx \frac{\bar{F}_x\left(e_x + \Delta e_x\right) - \bar{F}_x\left(e_x - \Delta e_x\right)}{2\Delta e_x}, \tag{24}$$

where Δe_x is a small displacement value and equals 0.01c. The results for the stiffness coefficient K_{xx} are shown in Fig. 6 for both methods. It is clearly shown that the two results are very close to each other. Therefore, the validity of the dynamic analysis method has been proven.

4.3. Parametric analysis of static performance

4.3.1. External load

In this subsection, the vibration amplitude and the nominal clearance are set to 15 μm and 30 μm, respectively. The relationship between the external load and the equilibrium position of the rotor at three different rotation speeds is shown in Fig. 7. The eccentricity ratio of the rotor increases with the increment of the external load for all three rotation speeds. The relationship between them is clearly non-linear. Given a heavier load, the film thickness becomes thinner leading to a higher

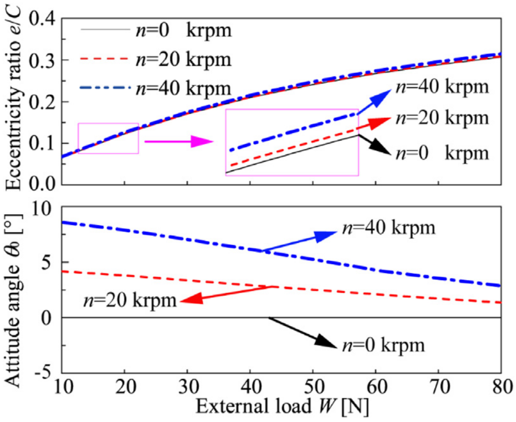

Fig. 7. Eccentricity ratio and attitude angle versus external load at three rotation speeds, computed for ξ=15 μm and c=30 μm, where the solid, dashed and dashed-dot lines represent the rotation speed n=0, 20 and 40 krpm, respectively.

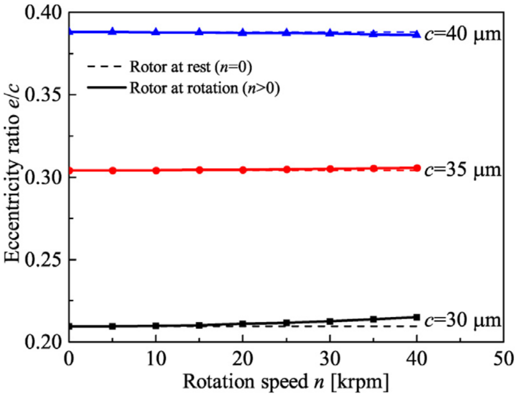

Fig. 8. Eccentricity ratio versus rotation speed at three nominal clearances, computed for ξ=15 μm and W=40 N, where the solid and dashed lines represent n>0 and =0 krpm, respectively.

pressure. A reduction of the air film thickness is equivalent to an increase in eccentricity. This variation trend is common for NFAL [33]. In the meantime, the attitude angle decreases as the external load increases. This is due to the increase in the ratio between the squeeze effect and the aerodynamic effect for thinner film thicknesses. In this situation, the position of the rotor is close to the x-axis. It is also found that the eccentricity ratio as well as the attitude angle increase as the rotation speed increases. This result is also observed in other hybrid air-lubricated bearings [62]. For light loads, the influence of the rotation speed on the eccentricity ratio is not evident.

4.3.2. Rotation speed and nominal clearance

Now, the vibration amplitude and external load are set to 15 μm and 40 N, respectively. Fig. 8 presents the effect of the rotation speed on the eccentricity ratio under three different bearing nominal clearances. It is shown that the eccentricity ratio decreases as the clearance decreases. This is because the squeeze effect is weakened by increasing the clearance. The same tendency can be found in other SFBs [26]. When the clearance c=40 μm, it is observed that the eccentricity ratio decreases when the rotation speed increases. In this condition, both, the aerodynamic and squeeze effects have a positive impact on the bearing capacity [44]. However, when the clearance c=35 μm and c=30 μm, the aerodynamic effect has a negative influence on the bearing capacity as mentioned in Section 4.1. Thus, the eccentricity ratio increases with the increment in rotation speed. However, the eccentricity ratio difference between pure squeeze effect ($n = 0$rpm) and both aerodynamic and squeeze effect ($n > 0$rpm) is very small as shown in Fig. 8. The eccentricity ratio difference in the case of a clearance of c=30 μm is slightly higher than for c=35 μm. Therefore, the influence of the rotation speed on the eccentricity ratio can be reduced by a reasonable design of the bearing clearance.

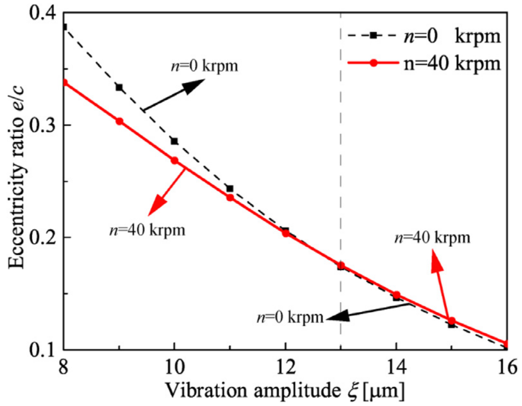

Fig. 9. Eccentricity ratio versus vibration amplitude at two rotation speeds, computed for c=30 μm and W=20 N, where the solid and dashed lines represent n=40 and 0 krpm, respectively.

4.3.3. Vibration amplitude

In this subsection, the nominal clearance and the external load are set to 30 μm and 20 N, respectively. *The vibration frequency remains unchanged in order to keep the same vibration mode shape of the Langevin transducer. The vibration amplitude is adjusted by changing the peak-to-peak value of the driving voltage* [28,36]. Fig. 9 depicts the relationship between the vibration amplitude of the pad and the eccentricity ratio of the rotor at two different rotation speeds. The eccentricity ratio decreases as the vibration amplitude increases. This is because the vibration amplitude has a remarkably positive effect on the levitation force in NFAL [34]. This phenomenon was also observed by experimental investigations on SFBs [28,64]. When the amplitude is set to a critical value, such as 13 μm in this study, the aerodynamic and squeeze effects are balanced. The variation of the eccentricity ratio with respect to the rotational speed is very small. If the amplitude is lower than the critical value, the importance of the aerodynamic effect increases. The eccentricity ratio of the rotor decreases as the rotational speed increases as described for other SFBs [44]. However, if the amplitude is higher than the critical value, the increment in rotation speed could lead to the increment in eccentricity ratio as discussed in Section 4.1.

4.4. Parametric analysis of dynamic performance

There are many factors that influence the dynamic performance of the bearing, such as rotation speed, external load and vibration amplitude of the pad, etc. As the SFB is put in operation, the vibration amplitude and the rotation speed are the most common parameters that can be varied. Thus, the impact of these two parameters on the dynamic performance of the bearing will be investigated. In addition, the effect of each pad on the dynamic performance of the bearing is discussed.

4.4.1. Rotation speed

In this subsection, the vibration amplitude of the pad and the nominal clearance are assumed to be 15 μm and 30 μm, respectively. The external load is 40 N. The calculated synchronous dynamic coefficients versus the rotation speed are shown in Fig. 10. It is clearly shown that the direct stiffness, i.e., K_{xx} and K_{yy}, slightly decreases with respect to the increase of the rotation speed. Since the squeeze effect is prominent in the x-direction and the bearing structure is not symmetric about both the x- and y-axis, the value for direct stiffness in the x-direction K_{xx} is greater than that in the y-direction K_{yy}. The direct damping C_{xx}

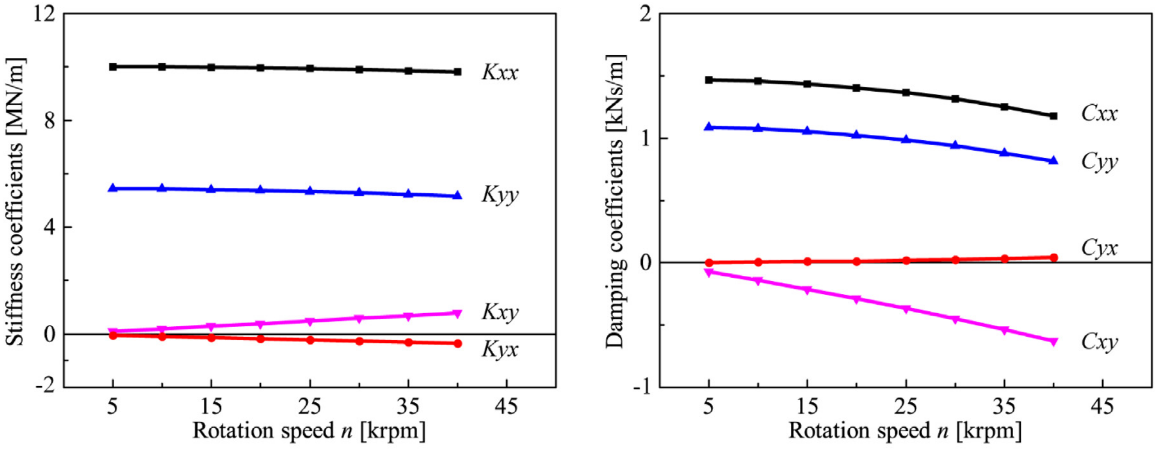

(a) (b)

Fig. 10. Calculated synchronous dynamic coefficients of the SFB versus rotation speed, computed for ξ=15 μm, c=30 μm and W=40 N. (a) stiffness coefficients; (b) damping coefficients.

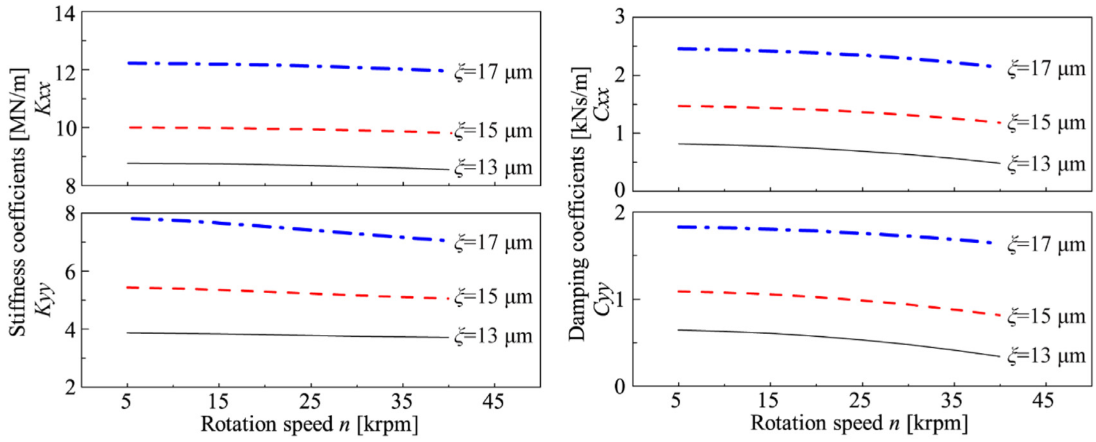

(a) (b)

Fig. 11. Calculated synchronous direct coefficients versus rotation speed at three different amplitudes, computed for c=30 μm and W=40 N, where the solid, dashed and dashed-dot lines represent the vibration amplitude ξ=13, 15 and 17 μm, respectively. (a) stiffness coefficients; (b) damping coefficients.

and C_{yy} have the same variation trend. The values of all cross-coupled stiffness and damping coefficients (K_{xy}, K_{yx}, C_{xy} and C_{yx}) increase as the rotation speed increases. These trends match with the results presented in [62]. Furthermore, the magnitude of the cross-coupled stiffness and damping coefficients are lower than those of their corresponding direct coefficients, which is obviously observed at a low rotation speed and is expected for the bearing design [2,65]. This trend is observed for other air-lubricated journal bearings [2,66].

4.4.2. Vibration amplitude

Now, the nominal clearance and the external load are set to 30 μm and 40 N, respectively. Fig. 11 shows the synchronous direct stiffness and damping coefficients versus rotation speed at three vibration amplitudes. Since the squeeze effect could be enhanced by increasing the vibration amplitude, the value for direct stiffness increases with increasing vibration amplitude. Increasing the amplitude makes the velocity of air squeezed out faster than the velocity of air compressed out from the air film. This leads to an increase in the amount of viscous damping in the air film [67]. Therefore, the direct damping coefficient increases with the increment in vibration amplitude. Further, the growth gradient of the direct stiffness and the direct damping coefficients increases with the increase in vibration amplitude. This is because that the squeeze effect is more evident in high vibration amplitude.

4.4.3. Bearing pad

Although the structure of the SFB consists of three separate pads, every pad works individually. Therefore, the trajectory of the rotor is easily controlled by adjusting the vibration amplitude of each pad. The effects of the vibration amplitude of each pad on the synchronous direct stiffness and damping coefficients are shown in Fig. 12. The nominal clearance, the rotation speed, and the external load are set to 30 μm, 20 krpm and 40 N, respectively. Only the vibration amplitude of one pad is changed while the vibration amplitudes of the other two pads remain unchanged and equal 15 μm. It is observed that the values for direct stiffness and damping coefficients increase with an increasing vibration amplitude. This phenomenon corresponds to the results of Section 4.4.2. For the direct coefficients in x-direction, i.e., K_{xx} and C_{xx}, the influence of Pad-3 on the change rate of these coefficients is more evident than that of the other two pads. This indicates that the effect of Pad-3 on the dynamic performance is vital. For the direct coefficients in y-direction, i.e., K_{yy} and C_{yy}, the change rates of these coefficients caused by Pad-1 and Pad-3 are very close, and higher than that caused by Pad-2. This

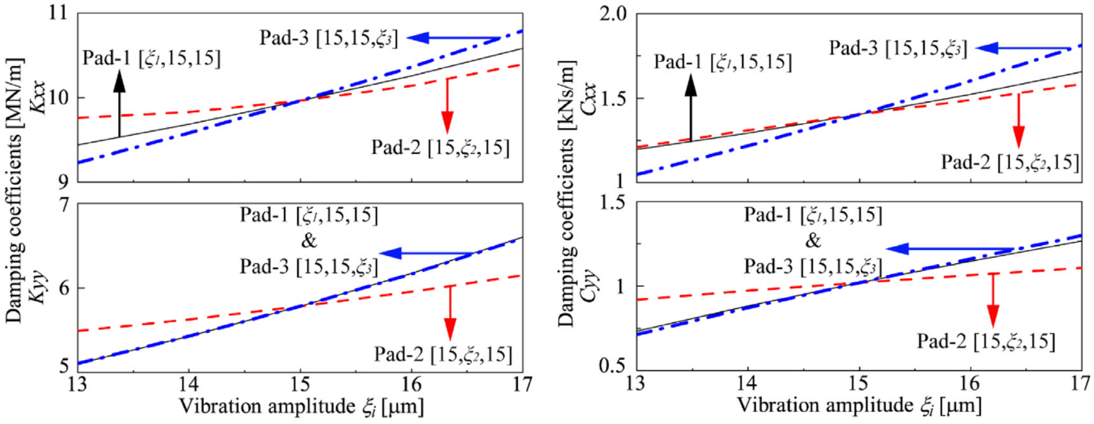

(a)

(b)

Fig. 12. Calculated synchronous direct coefficients versus vibration amplitudes of each pad, computed for c=30 μm, n=20 krpm and W=40 N, where the solid, dashed and dashed-dot lines represent Pad-1, Pad-2 and Pad-3, respectively. (a) Stiffness coefficients; (b) damping coefficients.

is because Pad-1 and Pad-3 are symmetric with respect to the x-axis. In conclude, Pad-1 and Pad-3 exhibit an important effect on the direct stiffness and damping coefficients than Pad-2.

5. Conclusions

This paper studied the static and dynamic characteristics of a three-pad squeeze film bearing. First, a simplified theoretical model was described and the governing equations introduced to describe the pressure distribution in the gas film of the bearing. Secondly, the stable equilibrium position of the rotor was calculated by the Newton-Raphson method. Substituting the film thickness and pressure which are updated by the perturbation method into the Reynolds equation, four differential equations were derived. This system of differential equations was then used to calculate all eight dynamic coefficients. The static and dynamic calculation methods were validated against the experimental results taken from [19]. Finally, the effects of external load, rotation speed, nominal clearance and vibration amplitude of the pad on the static performance of the squeeze film bearing were studied. Some conclusions were obtained from the calculated results, which are described as follows:

(1) The eccentricity of the rotor increases as the external load of the rotor increases or the vibration amplitude of the pad decreases.
(2) For given bearing parameters, there exists a critical value for the bearing clearance and the vibration amplitude. At this condition, the aerodynamic and squeeze effects are balanced. Therefore, the variation in eccentricity with respect to the rotational speed is quite small.
(3) The aerodynamic effect could enhance the bearing capacity if the bearing clearance is higher or the amplitude lower than the critical value. Otherwise, the bearing capacity is weakened by increasing the rotation speed.

The predicted dynamic performances of the bearing have also been presented for different rotation speeds and vibration amplitudes. Higher direct stiffness and damping coefficients are obtained for lower rotation speeds or higher amplitudes. All the three pads have a positive effect on the direct stiffness and damping coefficients. However, Pad-1 and Pad-3 play a more important role than Pad-2. This study has guiding significance in determining the parameters of squeeze film bearings. In addition, this study provides the theoretical basis for trajectory control of a rotor in the future.

Declaration of Competing Interest

The authors declare that they have no known competing financial interests or personal relationships that could have appeared to influence the work reported in this paper.

CRediT authorship contribution statement

Yuanyuan Liu: Conceptualization, Methodology, Data curtion, Validation, Writing – original draft. **Xiaodong Sun:** Methodology, Writing – review & editing. **Kian K. Sepahvand:** Supervision, Writing – review & editing. **Steffen Marburg:** Supervision, Writing – review & editing.

Acknowledgement

The first author acknowledges the support from China Scholarship Council (CSC) (grant number 201808340068). The authors acknowledge Dr. Zhao Su, Professor at Ningbo Institute of Materials Technology and Engineering, Chinese Academy of Sciences, for providing the experimental data in this paper.

References

[1] Andrés LS. Hybrid flexure pivot-tilting pad gas bearings: analysis and experimental validation. ASME J Tribol 2006;128:551–8.
[2] Feng K, Liu WH, Zhang ZM, Zhang T. Theoretical model of flexure pivot tilting pad gas bearings with metal mesh dampers in parallel. Tribol Int 2016;94:26–38.
[3] Hamrock BJ, Schmid SR, Jacobson BO. Fundamentals of fluid film lubrication. Boca Raton: CRC Press; 2004. p. 85–7.
[4] Heshmat H, Hermel P. Compliant foil bearings technology and their application to high speed turbomachinery. Tribol Ser 1993;25:559–75. doi:10.1016/S0167-8922(08)70411-5.
[5] Andrés LS, Rodríguez B. Experiments with a rotor-hybrid gas bearing system undergoing maneuver loads from its base support. ASME J Eng Gas Turbines Power 2020;142:111004.
[6] Sternlicht B. Gas-bearing turbomachinery. ASME J Lubr Tech 1968;90:665–78.
[7] Angantyr A, Aidanpaa JO. Constrained optimization of gas turbine tilting pad bearing designs. ASME J Eng Gas Turbines Power 2006;128:873–8.
[8] Feng K, Huang Z, Guo ZY. Design of spherical spiral groove bearings for a high-speed air lubricated gyroscope. Tribol Trans 2015;58:1084–95.
[9] Smolík L, Hajžman M, Byrtus M. Investigation of bearing clearance effects in dynamics of turbochargers. Int J Mech Sci 2017;127:62–72.
[10] Gu L, Guenat E, Schiffmann J. A review of grooved dynamic gas bearings. ASME Appl Mech Rev 2020;72:010802.
[11] Ford GW, Harris DM, Pantall D. Principles and applications of hydrodynamic-type gas bearings. Proc IMechE 1957;171:93–128.
[12] Heshmat H. Advancements in the performance of aerodynamic foil journal bearings: high speed and load capability. ASME J Tribol 1994;116:287–94.
[13] Yu YL, Pu G, Jiang TC, Jiang K. A dragonfly wing inspired biomimetic aerodynamic thrust bearing for increased load capacity. Int J Mech Sci 2020;176:105550.

[14] Xu FC, Sun Y, Zhang GH, Liu ZS. Effect of bump structural friction on the performance of bump foil bearing and rotor dynamic behavior: experimental study. Proc IMechE Part J 2019;233:702–11.
[15] Lee CC, You HI. Characteristics of externally pressurized porous gas bearings considering structure permeability. Tribol Trans 2009;52:768–76.
[16] Kim D, Lee D. Design of three-pad hybrid air foil bearing and experimental investigation on static performance at zero running speed. ASME J Eng Gas Turbine Power 2010;132:122504.
[17] Charki A, Diop K, Champmartin S, Ambari A. Numerical simulation and experimental study of thrust air bearings with multiple orifices. Int J Mech Sci 2013;72:28–38.
[18] Ueha S, Hashimoto Y, Koike Y. Non-contact transportation using near-field acoustic levitation. Ultrasonics 2000;38:26–32.
[19] Vandaele V, Lambert P, Delchambre A. Non-contact handling in microassembly: acoustical levitation. Precis Eng 2005;29:491–505.
[20] Liu YY, Shi MH, Feng K, Sepahvand KK, Marburg S. Stabilizing near-field acoustic levitation: Investigation of non-linear restoring force generated by asymmetric gas squeeze film. J Acoust Soc Am 2020;148:1468–77.
[21] Salbu E. Compressible squeeze films and squeeze bearings. ASME J Basic Eng 1964;86:355–64.
[22] Pan, C. Squeeze-film gas bearing technology. https://ntrs.nasa.gov/citations/19680000180, 1968 [accessed 4 August, 2013].
[23] Yoshimoto S. Floating characteristics of squeeze-film gas bearings with vibration absorber for linear motion guide. ASME J Tribol 1997;119:531–6.
[24] Gupta JL, Deheri GM. Effect of roughness on the behavior of squeeze film in a spherical bearing. Tribol Trans 1996;39:99–102.
[25] Ha D, Stolarski TA, Yoshimoto S. An aerodynamic bearing with adjustable geometry and self-lifting capacity. Part 1: self-lift capacity by squeeze film. Proc IMechE Part J 2004;219:33–9.
[26] Stolarski TA, Xue Y, Yoshimoto S. Air journal bearing utilizing near-field acoustic levitation stationary shaft case. Proc IMechE Part J 2011;225:120–7.
[27] Guo P, Gao H. An active non-contact journal bearing with bi-directional driving capability utilizing coupled resonant mode. CIRP Ann Manuf Technol 2018;67:405–8.
[28] Feng K, Shi MH, Gong T, Liu YY, Zhu J. A novel squeeze-film air bearing with flexure pivot-tilting pads: numerical analysis and measurement. Int J Mech Sci 2017;134:41–50.
[29] Stolarski TA, Gawarkiewicz R, Tesch K. Acoustic journal bearing—a search for adequate configuration. Tribol Int 2015;92:387–94.
[30] Wang C, Au YJ. Comparative performance of squeeze film air journal bearings made of aluminium and copper. Int J Adv Manuf Technol 2013;65:57–66.
[31] Shi MH, An L, Feng K, Guo ZY, Liu WH. Numerical and experimental study on the influence of material characteristics on the levitation performance of squeeze-film air bearing. Tribol Int 2018;126:307–16.
[32] Wang C, Au YJ. Levitation characteristics of a squeeze-film air journal bearing at its normal modes. Int J Adv Manuf Technol 2012;60:1–10.
[33] Hashimoto Y, Koike Y, Ueha S. Near-field acoustic levitation of planar specimens using flexural vibration. J Acoust Soc Am 1996;100:2057–61.
[34] Li WJ, Liu YY, Feng K. Modelling and experimental study on the influence of surface grooves on near-field acoustic levitation. Tribol Int 2017;116:138–46.
[35] Zhao S, Twiefel J, Wallaschek J. Design and experimental investigations of high power piezoelectric transducers for a novel squeeze film journal bearing. Proc SPIE 2009;7288:72881G. doi:10.1117/12.815724.
[36] Zhao S, Mojrzisch S, Wallaschek J. An ultrasonic levitation journal bearing able to control spindle center position. Mech Syst Signal Process 2013;36:168–81.
[37] Li H, Deng ZQ. Prediction of load-carrying capacity in the radial direction for piezoelectric-driven ultrasonic bearings. IEEE Access 2019;7:30599–614.
[38] Brunetière N, Wodtke M. Considerations about the applicability of the Reynolds equation for analyzing high-speed near field levitation phenomena. J Sound Vib 2020;483:115496.
[39] Stolarski TA, Gawarkiewicz R, Tesch K. Acoustic journal bearing–performance under various load and speed conditions. Tribol Int 2016;102:297–304.
[40] Shou T, Yoshimoto S, Stolarski TA. Running performance of an aerodynamic journal bearing with squeeze film effect. Int J Mech Sci 2013;77:184–93.
[41] Li H, Deng ZQ. Experimental study on friction characteristics and running stability of a novel ultrasonic levitating bearing. IEEE Access 2018;6:21719–30.
[42] Shi MH, Liu XJ, Feng K, Zhang K, Huang M. Running performance of a squeeze film air bearing with flexure pivot tilting pad. Tribol Trans 2020;63:704–17.
[43] Stolarski TA. Running characteristics of aerodynamic bearing with self-lifting capability at low rotational speed. Adv Tribol 2011;2011:973740. doi:10.1155/2011/973740.
[44] Feng K, Shi MH, Gong T, Huang Z. Integrated numerical analysis on the performance of a hybrid gas-lubricated bearing utilizing near-field acoustic levitation. Tribol Trans 2018;61:482–93.
[45] Beck JV, Strodtman CL. Stability of a squeeze-film journal bearing. ASME J of Lubr Tech 1967;89:369–73.
[46] Lund JW. Calculation of stiffness and damping properties of gas bearings. ASME J Lubr Technol 1968;90:793–803.
[47] Peng JP, Carpino M. Calculation of stiffness and damping coefficients for elastically supported gas foil bearings. ASME J Tribol 1993;115:20–7.
[48] Hassini MA, Arghir M, Frocot M. Comparison between numerical and experimental dynamic coefficients of a hybrid aerostatic bearing. ASME J Eng Gas Turbines Power 2012;134:921–31.
[49] Li LL, Zhang D, Xie YH. Effect of misalignment on the dynamic characteristic of MEMS gas bearing considering rarefaction effect. Tribol Int 2019;139:22–35.
[50] Czolczynski K. Rotordynamics of gas-lubricated journal bearing systems. New York: Springer; 1999. p. 11–14.
[51] Chen SK, Chou HC, Kang Y. Stability analysis of hydrodynamic bearing with herringbone grooved sleeve. Tribol Int 2012;55:15–28.
[52] Stolarski TA, Chai W. Load-carrying capacity generation in squeeze film action. Int J Mech Sci 2006;48:736–41.
[53] Feng K, Guan HQ, Zhao ZL, Liu TY. Active bump-type foil bearing with controllable mechanical preloads. Tribol Int 2018;120:187–202.
[54] Feng K, Zhao XY, Huo CJ, Zhang ZM. Analysis of novel hybrid bump-metal mesh foil bearings. Tribol Int 2016;103:529–39.
[55] Heshmat H, Walowit JA, Pinkus O. Analysis of gas-lubricated foil journal bearings. ASME J Lubr Technol 1983;105:647–55.
[56] Gero LR, Ettles C. An evaluation of finite difference and finite element methods for the solution of the Reynolds equation. ASLE Trans 1986;29:166–72.
[57] Kreyszig E, Kreyszig H, Norminton EJ. Advanced engineering mathematics. New York: John Wiley & Sons; 2011. p. 801–5.
[58] Qiu ZL, Tieu AK. The effect of perturbation amplitudes on eight force coefficients of journal bearings. Tribol Trans 1996;39:469–75.
[59] Li Q, Zhang S, Ma L, Xu WW, Zheng SY. Stiffness and damping coefficients for journal bearing using the 3D transient flow calculation. J Mech Sci Technol 2017;31:2083–91.
[60] Merelli CE, Barilá DO, Vignolo GG, Quinzani LM. Dynamic coefficients of finite length journal bearing. Evaluation using a regular perturbation method. Int J Mech Sci 2019;151:251–62.
[61] Lund JW. Review of the concept of dynamic coefficients for fluid film journal bearings. ASME J Tribol 1987;109:37–41.
[62] Feng K, Wu YH, Liu WH, Zhao XY, Li WJ. Theoretical investigation on porous tilting pad bearings considering tilting pad motion and porous material restriction. Precis Eng 2018;53:26–37.
[63] Liu PK, Li J, Ding H, Cao WW. Modeling and experimental study on near-field acoustic levitation by flexural mode. IEEE Trans Ultrason Ferroelectr Freq Control 2009;56:2679–85.
[64] Ono Y, Yoshimoto S, Miyatake M. Impulse-load dynamics of squeeze film gas bearings for a linear motion guide. ASME J Tribol 2009;131:041706.
[65] Ertas BH. Compliant hybrid journal bearings using integral wire mesh dampers. ASME J Eng Gas Turbines Power 2009;131:022503.
[66] Rudloff L, Arghir M, Bonneau O, Guingo S, Chemla G, Renard E. Experimental analysis of the dynamic characteristics of a hybrid aerostatic bearing. ASME J Eng Gas Turbines Power 2012;134:082503.
[67] Carpino M, Talmage G. Prediction of rotor dynamic coefficients in gas lubricated foil journal bearings with corrugated sub-foils. Tribol Trans 2006;49:400–9.

Publication C

Reproduced from

Yuanyuan Liu, Martin Eser, Xiaodong Sun, Kian K. Sepahvand, and Steffen Marburg

Theoretical analysis of a contactless transportation system for cylindrical objects based on ultrasonic levitation

in The Journal of the Acoustical Society of America, Volume 150, Issue 3, 2021, pp. 1682-1690, DOI: https://doi.org/10.1121/10.0006208, with the permission of the Acoustical Society of America.

AIP PUBLISHING LICENSE
TERMS AND CONDITIONS

Jul 01, 2022

This Agreement between Technical University of Munich -- Yuanyuan Liu ("You") and AIP Publishing ("AIP Publishing") consists of your license details and the terms and conditions provided by AIP Publishing and Copyright Clearance Center.

License Number	5340261048046
License date	Jul 01, 2022
Licensed Content Publisher	Acoustical Society of America
Licensed Content Publication	The Journal of the Acoustical Society of America
Licensed Content Title	Theoretical analysis of a contactless transportation system for cylindrical objects based on ultrasonic levitation
Licensed Content Author	Yuanyuan Liu, Martin Eser, Xiaodong Sun, et al
Licensed Content Date	Sep 1, 2021
Licensed Content Volume	150
Licensed	3

Content Issue	
Type of Use	Thesis/Dissertation
Requestor type	Author (original article)
Format	Print and electronic
Portion	Excerpt (> 800 words)
Will you be translating?	No
Title	Theoretical Analysis on Applications of Near-field Acoustic Levitation: Positioning, Bearing, and Transportation Systems
Institution name	Techincal University of Munich
Expected presentation date	Jul 2022
Portions	Full article
Requestor Location	Technical University of Munich Boltzmannstraße 15 Munich, 85748 Germany Attn: Technical University of Munich
Total	0.00 EUR

Terms and Conditions

Acoustic Society of America -- Terms and Conditions: Permissions Uses

Acoustic Society of America ("ASA") hereby grants to you the non-exclusive right and license to use and/or distribute the Material according to the use specified in your order, on a one-time basis, for the specified term, with a maximum distribution equal to the number that you have ordered. Any links or other content accompanying the Material are not the subject of this license.

1. You agree to include the following copyright and permission notice with the reproduction of the Material:"Reprinted with permission from [FULL CITATION]. Copyright [PUBLICATION YEAR], Acoustic Society of America." For an article, the copyright and permission notice must be printed on the first page of the article or book chapter. For photographs, covers, or tables, the copyright and permission notice may appear with the Material, in a footnote, or in the reference list.
2. If you have licensed reuse of a figure, photograph, cover, or table, it is your responsibility to ensure that the material is original to ASA and does not contain the copyright of another entity, and that the copyright notice of the figure, photograph, cover, or table does not indicate that it was reprinted by ASA, with permission, from another source. Under no circumstances does ASA, purport or intend to grant permission to reuse material to which it does not hold copyright.
3. You may not alter or modify the Material in any manner. You may translate the Material into another language only if you have licensed translation rights. You may not use the Material for promotional purposes. ASA reserves all rights not specifically granted herein.
4. The foregoing license shall not take effect unless and until ASA or its agent, Copyright Clearance Center, receives the Payment in accordance with Copyright Clearance Center Billing and Payment Terms and Conditions, which are incorporated herein by reference.
5. ASA or the Copyright Clearance Center may, within two business days of granting this license, revoke the license for any reason whatsoever, with a full refund payable to you. Should you violate the terms of this license at any time, ASA, Acoustic Society of America, or Copyright Clearance Center may revoke the license with no refund to you. Notice of such revocation will be made using the contact information provided by you. Failure to receive such notice will not nullify the revocation.
6. ASA makes no representations or warranties with respect to the Material. You agree to indemnify and hold harmless ASA, Acoustic Society of America, and their officers, directors, employees or agents from and against any and all claims arising out of your use of the Material other than as specifically authorized herein.
7. The permission granted herein is personal to you and is not transferable or assignable without the prior written permission of ASA. This license may not be amended except in a writing signed by the party to be charged.
8. If purchase orders, acknowledgments or check endorsements are issued on any forms containing terms and conditions which are inconsistent with these provisions, such inconsistent terms and conditions shall be of no force and effect. This document, including the CCC Billing and

Payment Terms and Conditions, shall be the entire agreement between the parties relating to the subject matter hereof.

This Agreement shall be governed by and construed in accordance with the laws of the State of New York. Both parties hereby submit to the jurisdiction of the courts of New York County for purposes of resolving any disputes that may arise hereunder.

Questions? customercare@copyright.com or +1-855-239-3415 (toll free in the US) or +1-978-646-2777.

JASA ARTICLE

Theoretical analysis of a contactless transportation system for cylindrical objects based on ultrasonic levitation

Yuanyuan Liu,[a] Martin Eser, Xiaodong Sun, Kian K. Sepahvand, and Steffen Marburg
Chair of Vibroacoustics of Vehicles and Machines, Technical University of Munich, Boltzmann Strasse 15, 85748 Garching, Germany

ABSTRACT:
Contactless transportation systems based on near-field acoustic levitation have the benefit of compact design and easy control which are able to meet the cleanliness and precision demands required in precision manufacturing. However, the problems involved in contactless positioning and transporting cylindrical objects have not yet been addressed. This paper introduces a contactless transportation system for cylindrical objects based on grooved radiators. A groove on the concave surface of the radiator produces an asymmetrical pressure distribution which results in a thrusting force to drive the levitator horizontal movement. The pressure distribution between the levitator and the radiator is acquired by solving the Reynolds equation. The levitation and the thrusting forces are obtained by integrating the pressure and the pressure gradient over the concave surface, respectively. The predicted results of the levitation force agree well with experimental observations from the literature. Parameter studies show that the thrusting force increases and converges to a stable value as the groove depth increases. An optimal value for the groove arc length is found to maximize the thrusting force, and the thrusting force increases as the groove width, the radiator vibration amplitude, and the levitator weight increase.
https://doi.org/10.1121/10.0006208

(Received 31 May 2021; revised 16 August 2021; accepted 19 August 2021; published online 8 September 2021)

[Editor: Nail A. Gumerov] Pages: 1682–1690

I. INTRODUCTION

Handling and transporting micro-electromechanical systems components or semiconductors is a challenging task due to their fragility and surface-sensitive characteristics.[1] Therefore, contactless manipulation is necessary in many situations.[2] Near-field acoustic levitation (NFAL) is a contactless technology that has attracted widespread attention in recent years. Compared to other contactless technologies, such as air cushion[3] or magnetic levitation,[4] the NFAL has two distinct advantages: (1) compact operation system and (2) no material restrictions for the levitator.[5] In 1975, when Whymark[6] investigated the ultrasonic levitation trapping small objects at the nodal positions of the standing wave field, he also found that a planar disk made of brass hovers above a piston operating at a vibration frequency of 20 kHz. This levitation phenomenon is referred to as NFAL. Hereafter, many researchers studied the mechanism and application of the NFAL. Hashimoto *et al.*[7] presented a numerical model in which the radiation surface vibrates harmonically in the in-phase mode. Based on this model, they derived a relationship between the levitation distance, the vibration amplitude, and the weight per unit area. Later, Hu *et al.*[8] pointed out that the sound field between the radiator and the levitator produces two forces which act on the bottom of the levitator. The first one is the acoustic radiation force that levitates the object. The second one is the acoustic viscous force that transports or rotates the object. These two forces play different roles in various applications. The acoustic radiation force is the main concerning force in contactless positioning or squeeze film bearing.[9,10] In these applications, the acoustic viscous force is unwanted in order to guarantee stability of the levitator. However, in contactless transportation[11] or ultrasonic motor[12] applications, both forces are important.

The NFAL is mainly categorized based on the property of the vibration wave. Two major types of the NFAL are (1) the traveling wave type levitation and (2) the standing wave type levitation. Correspondingly, two methods are generally used to generate an acoustic viscous force in the NFAL.[13] The first method uses a traveling wave sound field in the fluid between the vibrator and the levitator. This corresponds to the traveling wave type acoustic levitation. For example, Hashimoto *et al.*[14] used two longitudinal vibration systems to excite the traveling wave along a beam. A 7.6 g duralumin plate was able to be transported along this beam. Based on this transportation system, other investigators studied its transportation characteristics[15,16] or expanded its application field, e.g., for different cross-sections of the levitator.[17] In order to acquire a better transportation performance, Li *et al.*[18] introduced several engraved grooves on the surface of the levitator. An obvious characteristic of these traveling wave type-based transportation systems[14–18] is that they require a guide rail to produce vibration. Therefore, Koyama *et al.*[19] proposed a self-running sliding stage that produces a traveling wave vibration by itself. This stage not only produces self-levitation but also generates a thrusting force that produces forward motion.

---

[a] Electronic mail: yuanyuan.liu@tum.de, ORCID: 0000-0003-1916-0349.

The second method uses the asymmetric standing wave field to produce a gradient in the sound pressure field in the fluid domain. This corresponds to the standing wave type acoustic levitation. For instance, Hu *et al.*[20] used a wedge-shaped stator to generate the standing wave vibration. The levitator can be driven to move in the horizontal direction due to the gradient in the stator vibration amplitude along the stator's length. Based on the structure from this study, Hu *et al.*[21] developed a plate-shaped stator with triangular grooves to build a transportation system for long distance contactless transportation. These transportation systems[20,21] with a single vibration source cannot ensure the consistent motion velocity of the levitator because the vibration distribution is not uniform. Wei *et al.*[22] employed two longitudinal vibration sources to build a transportation system based on the standing wave type. These two vibration sources generate two non-parallel squeeze films with a pressure gradient between them. Similar to Ref. 19, Chen *et al.*[23] reported a self-running and self-floating actuator based on the standing wave type. This actuator uses its coupled resonant vibration mode to produce an asymmetric standing wave field. Aono *et al.*[24] proposed inserting the levitator between two opposing vibration sources to increase the levitator's holding force. This method can be used to acquire a high thrusting force for standing wave type transportation systems. Yet, this method decreases the load-carrying capacity of the transportation system since the two levitation forces oppose each other. Thus, this method is only suitable for light objects. However, the abovementioned transportation systems[14–23] can only carry levitators with planar surfaces. Since some precision components, e.g., in microsystems, exhibit cylindrical surfaces, the problem of contactless transport and positioning remains.

Previous investigation[25] regarding the NFAL stability problem revealed that an engraved groove on the levitator can break the symmetry of the sound field, which produces a restoring force. Therefore, this study deals with introducing a groove on the concave surface of the radiator and its stabilizing effect on the problem of contactless transport of cylindrical components. This modified radiator generates the levitation force and the thrusting force simultaneously. A transportation system composed of multiples of these modified radiators can levitate and move a cylindrical object. The pressure distribution between the radiator and the levitator is described by the non-linear Reynolds equation, which considers the horizontal movement of the levitator. The eight-point discrete method is used to solve the discontinuous film thickness problem, which arises due to the groove. The levitation force and the thrusting force are calculated by integrating the pressure and the pressure gradient, respectively. Numerical predictions of the levitation force agree well with experimental results from the literature.[26] Finally, the effects of the groove parameters, the radiator vibration amplitude, and the levitator weight on the thrusting force are studied.

This paper is organized as follows. Section II describes the working principle and the transportation system design. Section III presents the governing equations and the solution process for the pressure distribution. Sections IV and V discuss the pressure distribution of the squeeze film and the parameter study, respectively.

II. WORKING PRINCIPLE

In the NFAL, increasing the vibration amplitude enhances the load-carrying capacity of the levitation system.[27] The Langevin transducer is suitable for heavy loads since it produces high intensity vibration.[28] A typical Langevin transducer[26] mainly consists of five parts: the bolt, the back mass, the four piezoelectric transducer (PZT) plates, the horn, and the radiator with the concave surface, as shown in Fig. 1(a). Owing to the piezoelectric effect, the four PZT plates will generate the same frequency vibration along the through-thickness direction when a sinusoidal voltage with frequency f is applied. The horn transmits and amplifies the vibration produced by the PZT plates to the radiator. Since the radiator with the concave surface vibrates continuously, the air film between the concave surface and the outer surface of the cylindrical object is squeezed. Thus, the levitation force is generated by the squeeze film.

In the case of a smooth concave surface, there is a symmetric pressure distribution in the axial direction.[29] Therefore, no axial transport velocity is generated and the levitator's hovering position remains unchanged. Symmetry of the pressure distribution is broken by introducing a

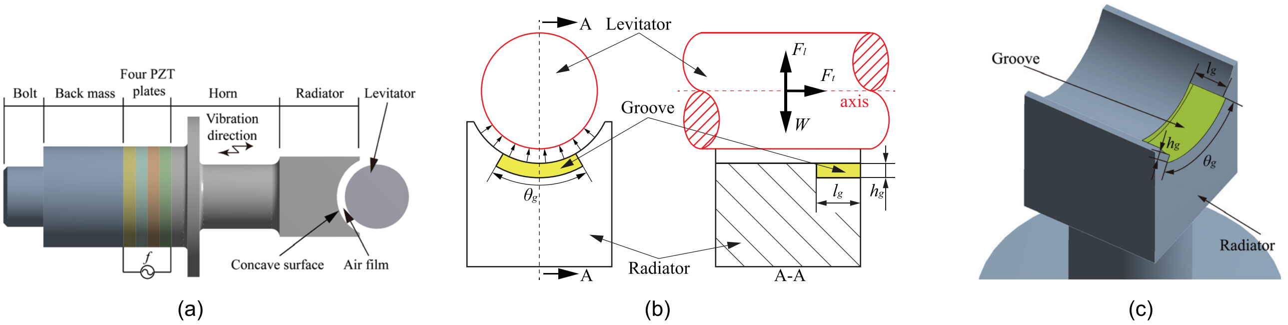

(a) (b) (c)

FIG. 1. (Color online) (a) Schematic diagram of the Langevin transducer (Ref. 26) used to produce the vibration, (b) the engraved groove on the radiator, which is used to produce the asymmetric pressure distribution in the axis direction, and (c) three-dimensional diagram of the location of the groove within the concave radiator.

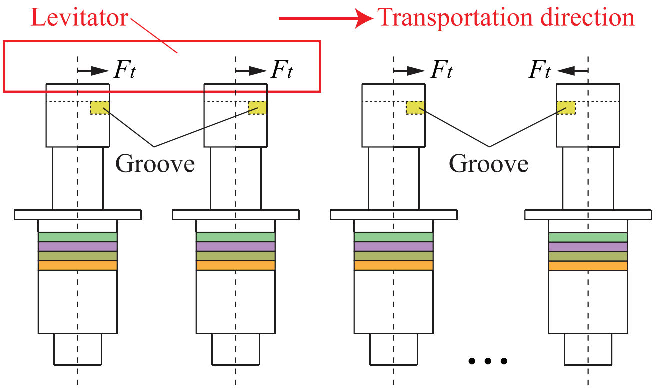

FIG. 2. (Color online) Schematic configuration of the contactless transportation system, which contains multiple Langevin transducers.

groove on the concave surface,[25] as shown in Fig. 1(b). The groove's geometric parameters are prescribed by its width l_g, its depth h_g, and its arc length θ_g. Figure 1(c) is presented to clearly depict the location of the groove within the radiator. According to the gas-film lubrication theory,[30] the established pressure gradient in the axial direction produces thrusting force F_t. Furthermore, levitation force F_l caused by the squeeze effect counteracts the weight of levitator W. Therefore, this method not only realizes the levitator suspension, but also drives its horizontal movement without any additional equipment.

Using multiple Langevin transducers creates a contactless transportation system for cylindrical objects, as shown in Fig. 2. This system can meet the demands for long-distance transportation. The levitator's transportation trajectory can be controlled by distributing transducers, by adjusting the radiator vibration amplitude, and by the orientation of the grooved surface. Changing the position of the groove can, for example, be used to slow down or stop the levitator at the end of the transportation system, cf. Fig. 2.

III. GOVERNING EQUATIONS AND NUMERICAL SOLUTION

A. Reynolds equation

The analytic model for one radiator is shown in Fig. 3. The center point, inner radius, and width of the radiator are denoted as O, R, and L, respectively. The center point and outer radius of the levitator are defined as O_l and r, respectively. Since the air film between the levitator and the radiator is symmetric in the circumferential direction and no other force exists to drive a rotation of the levitator, the levitator rotation is not considered. Further, the aerodynamic effect is neglected and therefore, only the squeeze effect exists in the air film. Hence, both center points are located on the x axis. The eccentricity displacement e is defined as the distance between O and O_l. The difference between R and r is denoted as the nominal clearance c. Since the levitator is simultaneously supported by several radiators (cf. Fig. 2), the levitator's inclination in the xOz-plane is neglected. In addition, the levitator is assumed to be a rigid body and well balanced.

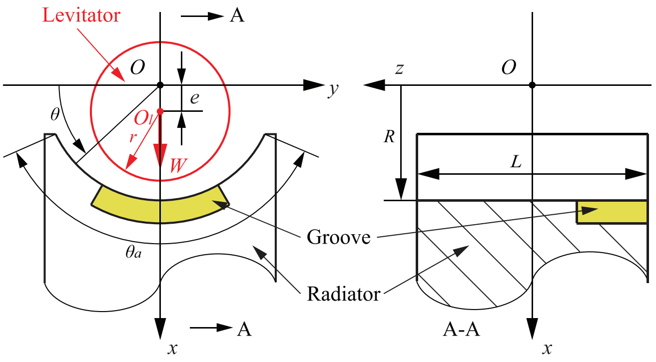

FIG. 3. (Color online) Analytic model for one radiator and corresponding coordinate systems.

The Reynolds equation is widely used to describe the pressure distribution of the squeeze film in the NFAL.[9,31] Some assumptions are introduced here to deduce the Reynolds equations. First, air is assumed to behave in a compressible manner and is treated as Newtonian fluid.[32] Second, since the film thickness is much smaller than the radiator's radius, the squeeze film is assumed to function an isothermal film[33] and the pressure gradient in film thickness direction is neglected.[15] Third, since the transportation speed is usually low, around several centimeters per second,[20,34] the Reynolds number is lower than the upper limit value for laminar flow.[33] Therefore, the airflow in the squeeze film is treated as laminar flow. Finally, the magnitude of fluid inertia and body forces are smaller than the viscous force[32] and they are neglected. The axial displacement of the levitator relative to its initial position is denoted as u. Based on these assumptions, the expression of the dimensionless Reynolds equation considering the movement of the levitator in the z-direction is[25,29]

$$\frac{\partial}{\partial\theta}\left(PH^3\frac{\partial P}{\partial\theta}\right)+\frac{\partial}{\partial Z}\left(PH^3\frac{\partial P}{\partial Z}\right)$$
$$=\sigma\frac{\partial(PH)}{\partial T}+\Lambda\frac{\partial(PH)}{\partial Z}-\alpha\frac{\partial(P^2H^3)}{\partial Z}, \tag{1}$$

in which $P = p/p_a$ and $H = h/c$ are the dimensionless air film pressure and air film thickness, respectively. $T = \omega\cdot t = 2\pi f\cdot t$ is the dimensionless form of time t and the dimensionless width position is $Z = z/R$. p_a denotes the pressure of the ambient air, h is the thickness of the air film, and the squeeze number is $\sigma = 12\mu_a\omega R^2/p_a c^2$. The coefficients $\Lambda = 6\mu_a\dot{u}R/p_a c^2$ and $\alpha = \rho_a\ddot{u}R/2p_a$ represent the effects of the levitator movement speed $\dot{u}$ and its acceleration $\ddot{u}$ on the pressure. μ_a and ρ_a are the viscosity coefficient and the density of air.

B. Boundary conditions and film thickness

As shown in Fig. 3, the arc length of the concave surface of the radiator is defined as θ_a. Due to the continuity of the pressure at the interface to the ambient air, the pressure on the boundary of the squeeze film meets the following conditions:

$$P(\theta, z = \pm L/2) = 1, \tag{2}$$

$$P(\theta = \pi/2 \pm \theta_a/2, z) = 1. \tag{3}$$

Since the radial displacement of the radiator can be treated as uniform,[26] the normalized mode shape $V(\theta, z)$ equals 1. It is assumed that the existence of the groove does not affect the radiator's vibration amplitude distribution in order to conveniently conduct the parameter study. This assumption is reasonable if the dimension of the groove is much smaller than that of the radiator. Referring to Figs. 1(b) and 3, the grooved domain includes the front ($z = L/2$), the rear ($z = L/2 - l_g$), the right ($\theta = \pi/2 + \theta_g/2$), and the left ($\theta = \pi/2 - \theta_g/2$) boundaries. Thus, the squeeze film thickness is expressed as

$$h = \begin{cases} c - e \cdot \sin(\theta) + \xi \cdot V(\theta, z) \cdot \sin(T) + h_g \\ \quad \text{(groove domain)}, \\ c - e \cdot \sin(\theta) + \xi \cdot V(\theta, z) \cdot \sin(T) \\ \quad \text{(remaining domain)}, \end{cases} \tag{4}$$

where ξ is the maximum value of the radial vibration displacement.

C. Solution process

The computational domain is the area of the radiator's concave surface, as shown on the left in Fig. 4. This domain is divided into a grid of $m \times n$ sections, in which m defines the discretization in θ- and n in z-directions, i.e., $\Delta\theta = \theta_a/m$ and $\Delta z = L/n$. The film thickness becomes discontinuous at the edges of the groove domain. Therefore, the partial differentials $(\partial H/\partial\theta)_{i,j}$ and $(\partial H/\partial Z)_{i,j}$ in Eq. (1) are unsolvable.

In the field of gas lubrication, the eight-point discrete method is adopted to solve this discontinuous film thickness problem.[35,36] All nodes on the four boundary lines (i.e., $z = \pm L/2$ and $\theta = \pi/2 \pm \theta_a/2$) meet the boundary conditions in Eqs. (2) and (3). The inside node $G_{i,j}$ is surrounded by the area Ω_{ij}, which is spanned by the four red dashed lines $\Gamma_{ij,1-4}$, as seen on the right in Fig. 4. The adjacent eight points $N_{ij,1-8}$ in the eight-point discrete grid are evenly distributed on the four perimeter lines $\Gamma_{ij,1-4}$.

By integrating Eq. (1) over Ω_{ij}, the dimensionless rate of airflow passing through Ω_{ij} can be expressed as

$$\begin{aligned} &\iint_{\Omega_{ij}} \left\{ \frac{\partial}{\partial\theta}\left(PH^3 \frac{\partial P}{\partial\theta} \right) + \frac{\partial}{\partial Z}\left[PH^3 \frac{\partial P}{\partial Z} \right] \right\} d\theta dZ \\ &\quad = \iint_{\Omega_{ij}} \left[\sigma \frac{\partial(PH)}{\partial T} \right] d\theta dZ \\ &\quad + \iint_{\Omega_{ij}} \left[\Lambda \frac{\partial(PH)}{\partial Z} - \alpha \frac{\partial(P^2H^3)}{\partial Z} \right] d\theta dZ. \end{aligned} \tag{5}$$

The surface integral on the left side and the second term on the right side of Eq. (5) can be transformed to a closed line integral by using Green's theorem,

$$\begin{aligned} &\oint_{\Gamma_{ij}} \left[-\left(PH^3 \frac{\partial P}{\partial Z} \right) d\theta + \left(PH^3 \frac{\partial P}{\partial\theta} \right) dZ \right] \\ &\quad = \iint_{\Omega_{ij}} \left[\sigma \frac{\partial(PH)}{\partial T} \right] d\theta dZ \\ &\quad + \oint_{\Gamma_{ij}} \left[\alpha\partial(P^2H^3) - \Lambda\partial(PH) \right] d\theta. \end{aligned} \tag{6}$$

The path of line integration runs counterclockwise, which means from $\Gamma_{ij,1}$ to $\Gamma_{ij,4}$. Since the projections of $\Gamma_{ij,2}$ and $\Gamma_{ij,4}$ on the θ-axis equal zero, the first term on the left side of Eq. (6) reduces to

$$\begin{aligned} \oint_{\Gamma_{ij}} -\left(PH^3 \frac{\partial P}{\partial Z} \right) d\theta = &-\int_{\Gamma_{ij,1}} \left(PH^3 \frac{\partial P}{\partial Z} \right) d\theta \\ &-\int_{\Gamma_{ij,3}} \left(PH^3 \frac{\partial P}{\partial Z} \right) d\theta. \end{aligned} \tag{7}$$

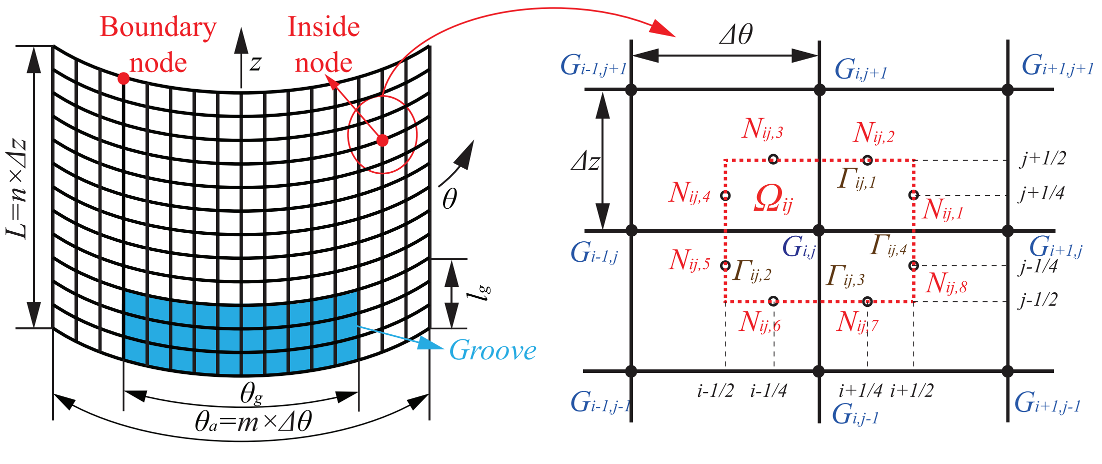

FIG. 4. (Color online) The mesh system of the computational domain, where the detailed eight-point discrete grid is presented on the right side.

The film thickness of each perimeter line is approximately equal to the arithmetic average film thickness of the two corresponding points which lie on the perimeter line[35] such as $H^3(\Gamma_{ij,1}) = (H^3_{i-1/4,j+1/2} + H^3_{i+1/4,j+1/2})/2$. Subsequently, using the center difference method and the trapezoidal rule, the right side of Eq. (7) can be expressed as

$$\begin{aligned}
&-\int_{\Gamma_{ij,1}} \left(PH^3 \frac{\partial P}{\partial Z}\right) d\theta - \int_{\Gamma_{ij,3}} \left(PH^3 \frac{\partial P}{\partial Z}\right) d\theta \\
&\quad = (P_{i,j} + P_{i,j+1})(P_{i,j+1} - P_{i,j}) \\
&\qquad \times \left(H^3_{i-1/4,j+1/2} + H^3_{i+1/4,j+1/2}\right) \frac{\Delta\theta}{4\Delta Z} \\
&\qquad -(P_{i,j} + P_{i,j-1})(P_{i,j} - P_{i,j-1}) \\
&\qquad \times \left(H^3_{i-1/4,j-1/2} + H^3_{i+1/4,j-1/2}\right) \frac{\Delta\theta}{4\Delta Z}. \qquad (8)
\end{aligned}$$

All terms in Eq. (6) can be expanded in the same form as Eq. (8). Thus, the nonlinear differential equation that describes the relation between the pressure and the film thickness over time is stated as

$$f(P_{i-1,j}, P_{i,j}, P_{i+1,j}, P_{i,j-1}, P_{i,j+1}, H, T) = 0. \qquad (9)$$

The Newton–Raphson method is used to linearize Eq. (9),[37] which acquires the pressure distribution in the computational domain. The mean levitation force $\bar{F}_l$ and the mean thrusting force $\bar{F}_t$ in one vibration period follow as[11]

$$\begin{bmatrix} \bar{F}_l \\ \bar{F}_t \end{bmatrix} = \frac{1}{2\pi} \int_0^{2\pi} \int_{\pi/2-\theta_a/2}^{\pi/2+\theta_a/2} \int_{-L/2}^{L/2} \begin{bmatrix} (p - p_a)\sin(\theta) \\ \dfrac{h}{2}\dfrac{\partial p}{\partial z} + \mu_a \dfrac{\dot{u}}{h} + \dfrac{\rho_a h \ddot{u}}{3} \end{bmatrix} dz d\theta dT. \qquad (10)$$

Under the steady conditions, the mean levitation force counterbalances the weight of the levitator, i.e., $\bar{F}_l = W$. The mean thrusting force is mainly influenced by four variables: film thickness h, pressure gradient in z-direction $\partial p/\partial z$, levitator movement speed $\dot{u}$, and its acceleration $\ddot{u}$.

IV. PRESSURE DISTRIBUTION AND VALIDATION

A basic design of this radiator is used to quantify the effect of the groove on the pressure distribution. The parameters for the basic design and its operating condition are listed in Table I. In addition to this basic setup, transportation velocity $\dot{u}$ and acceleration $\ddot{u}$ are assumed to be zero to conveniently analyze the effect of the groove parameters on the thrusting force by using control variates. The influence of the mesh size on the numerical results has been checked in previous studies,[25,29] which is not displayed here for the sake of brevity. A mesh resolution of $m \times n = 60 \times 40$ has been identified for sufficient results with respect to calculation time and convergence. All parameters remain as listed in Table I, if not specified elsewhere throughout the following studies.

Since the radiator vibrates continuously, the film thickness and pressure vary over time. When the squeeze system reaches a steady condition, the transient film thickness and pressure are periodic functions in time with vibration frequency f. The dimensionless pressure distributions of the radiator's basic configurations with a smooth and a grooved surfaces at the onset time of one steady period are shown in Fig. 5(a). The corresponding distributions of the dimensionless pressure gradient are displayed in Fig. 5(b).

For the radiator configuration with a smooth surface, the pressure distribution is symmetric with respect to the xOz- and the xOy-planes, see top of Fig. 5(a). Therefore, only levitation force F_l is produced and no thrusting force acts on the levitator. For the grooved configuration, corresponding to the bottom of Fig. 5(a), the pressure value in the groove domain equals the ambient pressure, i.e., $P = 1$. This results from the contact between groove domain and ambient air such that the squeeze effect is not evidenced in the groove domain. Hence, symmetry of the pressure distribution about the xOy-plane is broken due to the existence of the groove. The asymmetric pressure distribution in the z-direction produces thrusting force F_t, and the available domain with squeeze effect is smaller than for the smooth surface configuration. Thus, given the same weight of the levitator, the dimensionless maximum pressure value in the grooved condition ($P_{\max} = 1.1443$) is higher than that in the smooth condition ($P_{\max} = 1.1333$).

Figure 5(b) shows that the pressure gradient value is antimetric in the z-direction for the smooth surface configuration. Since the positive part and the negative part are of equal magnitude [$\boldsymbol{\Sigma}(\partial P/\partial Z) = 0$], the thrusting force equals zero, which corresponds to the results presented in Fig. 5(a). However, the balance between the positive part and the negative part is changed by the groove. The pressure gradient value in the groove domain equals zero. The negative part

TABLE I. Parameters of the radiator's basic design and its operating condition.

Parameter	Value	Parameter	Value
Vibration amplitude ξ	9 μm	Vibration frequency f	20 kHz
Radiator concave radius R	10 mm	Levitator outer radius r	9.96 mm
Nominal clearance c	40 μm	Radiator width L	20 mm
Radiator arc length θ_a	120°	Groove width l_g	3 mm
Groove depth h_g	1 mm	Groove arc length θ_g	80°
Air dynamic viscosity μ_a	1.81×10^{-5} Pa s	Air pressure p_a	1.013×10^5 Pa
Air density ρ_a	1.204 kg/m^3	Weight of the levitator W	0.5 N

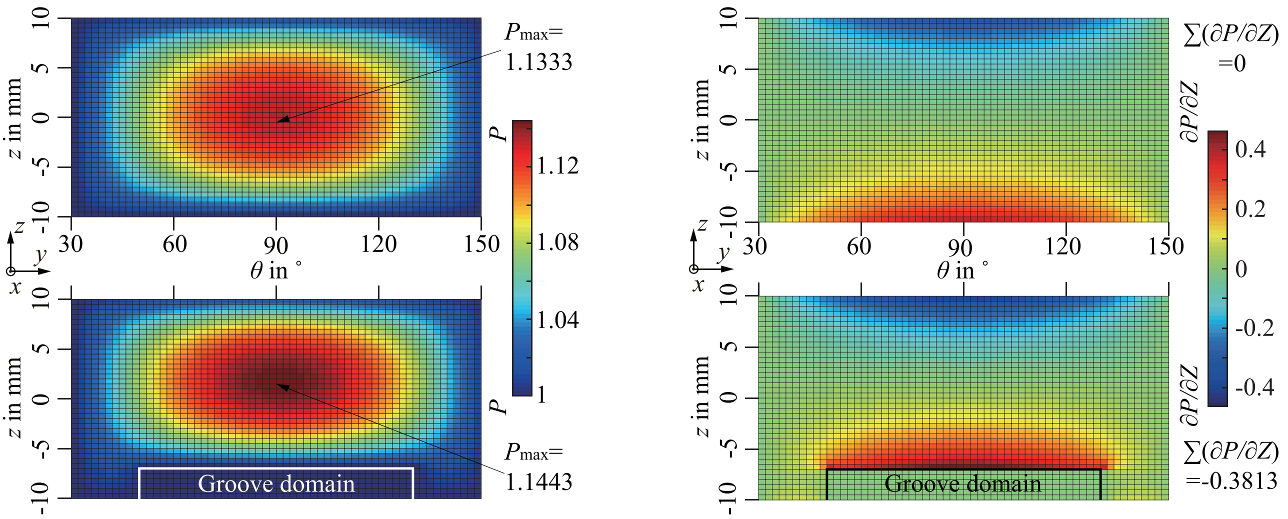

(a) (b)

FIG. 5. (Color online) Comparison of the dimensionless pressure (a) and pressure gradient (b) for configurations with a smooth and a grooved surfaces at the onset of one steady period, computed for W=0.5 N and ξ=9 μm.

dominates in this case $[\Sigma(\partial P/\partial Z) = -0.3813]$, which means that the thrusting force points toward the negative z-direction.

The variation in thrusting force F_t in one steady period is shown in Fig. 6. The value of the thrusting force alternates between negative and positive. The maximum negative thrusting force absolute value is 1.6355 mN, which is larger than the positive absolute value 1.3341 mN. Therefore, a mean thrusting force of $\bar{F}_t$ $\bar{F}_t = -0.1182$ mN is generated, since negative contributions for the thrusting force dominate.

The measurement method of the levitation force stated in Ref. 26 is represented by the simplified diagram shown in Fig. 7(a). When the levitation system reaches a steady condition, the levitation force generated by the squeeze film is counteracting the external load which contains the weight of the levitator and two objects. Therefore, the value of the levitation force is adjusted by changing the weight of the two objects. At the same time, the levitation height is measured by the displacement sensor. Consequently, experimental data which describes the relationship between the levitation height and the levitation force is obtained. In order to validate the proposed calculation method, numerical calculation results are compared to with these experimental data from Ref. 26. Some calculation parameters are adjusted compared to the basic configuration. The adjusted parameters are listed in Table II. All other parameters remain as prescribed for the basic configuration.

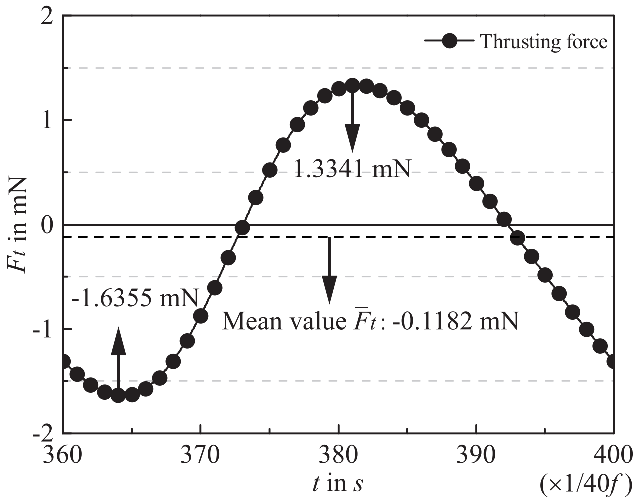

FIG. 6. Temporal variation of the thrusting force in one steady period, where the dashed line represents the mean thrusting force of one period, computed for W=0.5 N, ξ=9 μm, h_g=1 mm, θ_g=80°, and l_g=3 mm.

Figure 7(b) shows the comparison between numerical calculation and experimental results in terms of the levitation force. The levitation force decreases with increasing levitation height $c - e$. This is due to the weakening of the squeeze effect for higher levitation heights.[7] The calculated results match well with the experimental data.

V. PARAMETRIC ANALYSIS

For a given radiator, the thrusting force is mainly determined by four variables as mentioned in Sec. III C. The first two variables, i.e., the film thickness and the pressure gradient, are mainly affected by the groove parameters, the radiator vibration amplitude, and the levitator weight. The other two variables, i.e., levitator movement velocity and its acceleration, are assumed to be zero as mentioned in Sec. IV. In the following parametric study, only the absolute values of the forces are presented, since the directions of the thrusting forces are the same.

A. Groove depth

According to Li *et al.*,[38] the groove depth has an obvious influence on the squeeze effect. In order to determine the effect of the groove depth on the thrusting force, a

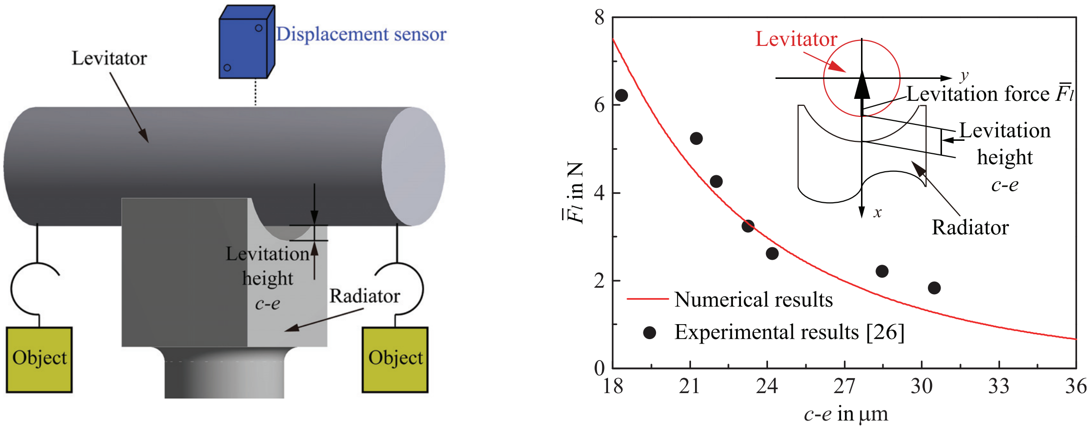

(a)

(b)

FIG. 7. (Color online) (a) Measuring principle of levitation force stated in Ref. 26 and (b) comparison between numerical and the experimental results from the literature (Ref. 26), where the solid line represents the numerical results, and the dots are the published experimental data.

configuration with three different radiator vibration amplitudes (ξ=8, 9, and 10 μm) is analyzed for varying groove depths. Figure 8 displays the variation of the thrusting force with the groove depth for all three vibration amplitude configurations. The thrusting force obviously increases when the groove depth is lower than 0.9 mm. This phenomenon occurs because the magnitude of the groove depth approximates the magnitude of the nominal clearance in low groove depth. Thus, the squeeze effect still exists in the groove domain, which in turn leads to a deviation in the pressure in the groove domain from the ambient pressure. The squeeze effect weakens with increasing groove depth. Finally, the thrusting force converges to a constant value when the groove depth exceeds 0.9 mm. Therefore, the groove depth is set to 1 mm in this study to acquire a high thrusting force. This trend is visible for different amplitudes. The relationship between the thrusting force and the amplitude will be discussed in Sec. V D.

B. Groove arc length

Figure 9 presents the relation between thrusting force and groove arc length for three different vibration amplitudes, namely, ξ = 8, 9, and 10 μm. The thrusting force initially increases and then decreases as the groove arc length increases. For a groove arc length of $\theta_g = 0°$, the concave surface is a smooth surface. In this case, the thrusting force equals zero as discussed in Sec. IV. For a groove arc length of $\theta_g = 120°$, the concave surface becomes a new smooth surface with the width $L - l_g$. This new surface is also symmetric in the z-direction. Thus, the thrusting force is also zero. As the groove arc length increases, the available domain with the squeeze effect decreases. At a constant levitation force, the maximum pressure value and the pressure gradient increase while the film thickness decreases. According to Eq. (10), the thrusting force is simultaneously affected by the pressure gradient and the film thickness. Therefore, there is an optimum value for the groove arc length. Since the high-pressure air is located in the area near the middle line $\theta = 90°$ in the θ-direction as shown in Fig. 5(a), the influence of the groove on the pressure gradient and the film thickness attenuates as the groove arc length increases. Thus, the variation of the thrusting force is steeper for small groove arc lengths ($\theta_g < 40°$) than for large groove arc lengths ($\theta_g > 40°$). The optimal groove arc length falls on the low-value side and is nearly 40° for the given parameters and operating condition.

TABLE II. Adjusted parameters of the radiator, according to Ref. 26.

Parameter	Value	Parameter	Value
Vibration amplitude ξ	10.8 μm	Vibration frequency f	16.11 kHz
Radiator concave radius R	10.015 mm	Levitator outer radius r	9.985 mm
Nominal clearance c	30 μm	Radiator arc length θ_a	110°
Total mesh grid number $m \times n$	55 × 40	Radiator width L	20 mm

C. Groove width

W θ_g h_g In this subsection, the groove arc length is set to $\theta_g = 40°$. Figure 10 shows the relationship between

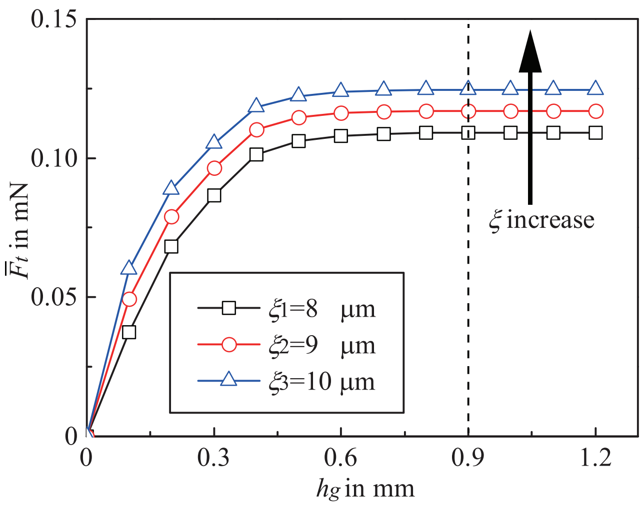

FIG. 8. (Color online) Thrusting force versus groove depth at three vibration amplitudes, computed for W=0.5 N, θ_g=80°, and l_g=3 mm.

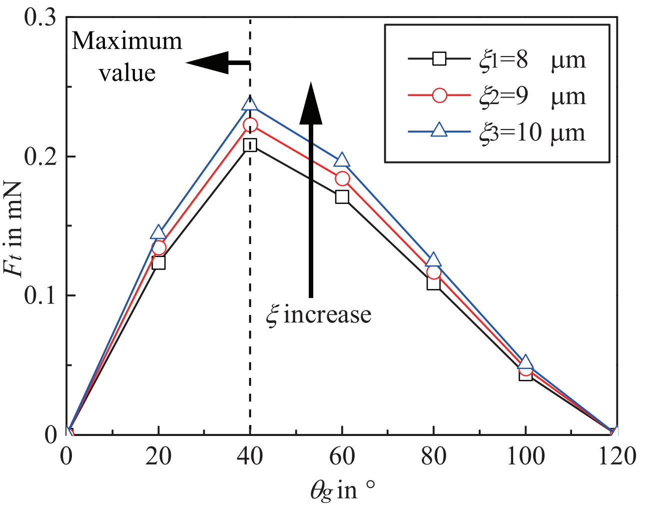

FIG. 9. (Color online) Thrusting force versus groove arc length at three vibration amplitudes, computed for $W = 0.5$ N, $h_g = 1$ mm, and $l_g = 3$ mm.

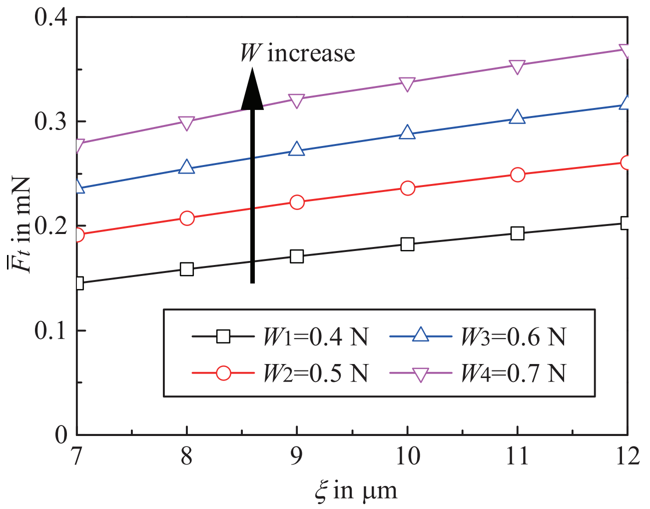

FIG. 11. (Color online) Thrusting force as a function of the vibration amplitude at four different levitator weights, computed for $h_g = 1$ mm, $\theta_g = 40°$, and $l_g = 3$ mm.

thrusting force and groove width for three different vibration amplitudes ($\xi = 8$, 9, and $10\,\mu$m). The thrusting force increases with increasing groove width. This result agrees with the numerical and experimental results presented by Liu *et al.*,[25] who used an engraved groove levitator to replace the levitator's misalignment. However, the available domain with the squeeze effect decreases if the groove width increases. Thus, the levitator cannot be suspended when the groove width is too great. Consequently, the study of the thrusting force is only meaningful within a small range of the groove width.

D. Vibration amplitude and levitator weight

The change in vibration amplitude is assumed to stem from changes in the driving voltage,[39] while the vibration frequency remains unchanged in order to keep the same vibration mode shape of the radiator. In this subsection, the groove arc length is set to $\theta_g = 40°$. Figure 11 depicts the thrusting force as a function of the vibration amplitude at four different weights of the levitator, namely, $W = 0.4$, 0.5, 0.6, and 0.7 N. The thrusting force increases as the weight increases, which is consistent with the results of Refs. 13 and 25. A higher levitator weight indicates a smaller levitation height at a constant vibration amplitude. According to Li *et al.*,[16] the thrusting force increases under these conditions. Additionally, the thrusting force follows a positive linear trend with increasing vibration amplitude. This is due to the fact that the squeeze effect is enhanced by increasing vibration amplitude.[25,40]

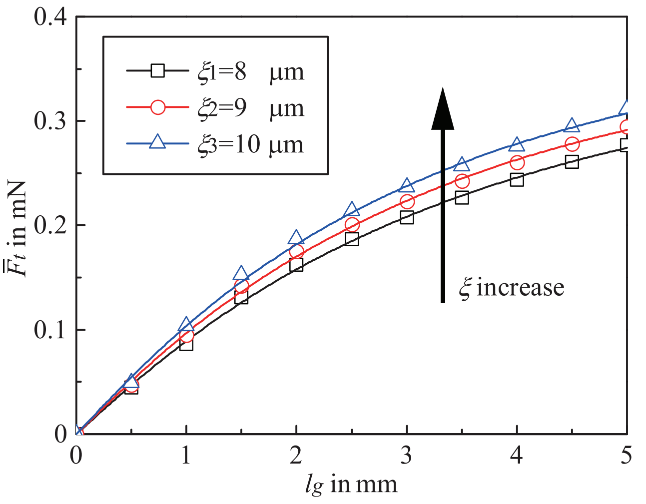

FIG. 10. (Color online) Relationship of the thrusting force and groove width at three vibration amplitudes, computed for $W = 0.5$ N, $\theta_g = 40°$, and $h_g = 1$ mm.

VI. CONCLUSIONS

This paper introduced the design of a contactless transportation system for cylindrical objects. The levitation and transport are based on near-field acoustic levitation. The thrusting force for the transported items is generated by the radiator that has an engraved groove. Theoretical analysis of the influence of the groove on the pressure distribution is also presented. The nonlinear Reynolds equation which describes the relationship between the pressure and the motion of the levitator has been solved by combining the eight-point discrete method and the Newton–Raphson method. The levitation force and the thrusting force are calculated from the solved pressure distribution. The calculated levitation force agrees well with similar results in the literature.[26] Moreover, the effects of groove depth, groove arc length, and groove width on the thrusting force have been investigated to determine suitable groove parameters. The predicted results yield the following conclusions:

(1) The thrusting force initially increases and then remains at a stable value as the groove depth increases.
(2) There is an optimal groove arc length to maximize the thrusting force.

(3) Increasing the groove width can improve the transportation performance within a small range of groove width.
(4) Increasing the vibration amplitude of the radiator can increase the thrusting force.
(5) A higher levitator weight can lead to higher thrusting forces.

Future work addresses the manufacture of a prototype for this transportation system. Furthermore, precisely controlling the motion trajectory of the levitator by adding a control algorithm is planned. This paper and our continuing research supply a helpful guide for designing a practical contactless transportation system for cylindrical objects in industrial applications.

ACKNOWLEDGMENT

The first author acknowledges the support provided by the China Scholarship Council (CSC) (Grant No. 201808340068).

[1] G. Reinhart and J. Hoeppner, "Non-contact handling using high-intensity ultrasonics," CIRP Ann. **49**(1), 5–8 (2000).
[2] P. Liu, J. Li, H. Ding, and W. Cao, "Modeling and experimental study on near-field acoustic levitation by flexural mode," IEEE Trans. Ultrason. Ferroelectr. Freq. Control **56**(12), 2679–2685 (2009).
[3] F. Erzincanli, J. Sharp, and S. Erhal, "Design and operational considerations of a non-contact robotic handling system for non-rigid materials," Int. J. Mach. Tool. Manuf. **38**(4), 353–361 (1998).
[4] O.-S. Kim, S.-H. Lee, and D.-C. Han, "Positioning performance and straightness error compensation of the magnetic levitation stage supported by the linear magnetic bearing," IEEE. Trans. Ind. Electron **50**(2), 374–378 (2003).
[5] V. Vandaele, P. Lambert, and A. Delchambre, "Non-contact handling in microassembly: Acoustical levitation," Precis. Eng. **29**(4), 491–505 (2005).
[6] R. Whymark, "Acoustic field positioning for containerless processing," Ultrasonics **13**(6), 251–261 (1975).
[7] Y. Hashimoto, Y. Koike, and S. Ueha, "Near-field acoustic levitation of planar specimens using flexural vibration," J. Acoust. Soc. Am. **100**(4), 2057–2061 (1996).
[8] J. Hu, K. Nakamura, and S. Ueha, "An analysis of a noncontact ultrasonic motor with an ultrasonically levitated rotor," Ultrasonics **35**(6), 459–467 (1997).
[9] T. Stolarski and W. Chai, "Load-carrying capacity generation in squeeze film action," Int. J. Mech. Sci. **48**(7), 736–741 (2006).
[10] D. Ha, T. Stolarski, and S. Yoshimoto, "An aerodynamic bearing with adjustable geometry and self-lifting capacity. Part 1: Self-lift capacity by squeeze film," Proc. Inst. Mech. Eng. J. Part J **219**(1), 33–39 (2005).
[11] K. Feng, Y. Liu, and M. Cheng, "Numerical analysis of the transportation characteristics of a self-running sliding stage based on near-field acoustic levitation," J. Acoust. Soc. Am. **138**(6), 3723–3732 (2015).
[12] Z. Dong, M. Yang, Z. Chen, L. Xu, F. Meng, and W. Ou, "Design and performance analysis of a rotary traveling wave ultrasonic motor with double vibrators," Ultrasonics **71**, 134–141 (2016).
[13] J. Hu, K. Nakamura, and S. Ueha, "Stability analysis of an acoustically levitated disk," IEEE Trans. Ultrason. Ferroelectr. Freq. Control **50**(2), 117–127 (2003).
[14] Y. Hashimoto, Y. Koike, and S. Ueha, "Transporting objects without contact using flexural traveling waves," J. Acoust. Soc. Am. **103**(6), 3230–3233 (1998).
[15] A. Minikes and I. Bucher, "Noncontacting lateral transportation using gas squeeze film generated by flexural traveling waves—Numerical analysis," J. Acoust. Soc. Am. **113**(5), 2464–2473 (2003).
[16] J. Li, W. Cao, and W. Zhang, "A nonlinear model for the layer between plates in acoustic noncontact transportation," J. Appl. Phys. **116**(21), 214905 (2014).
[17] T. Ide, J. Friend, K. Nakamura, and S. Ueha, "A non-contact linear bearing and actuator via ultrasonic levitation," Sens. Actuat. A Phys. **135**(2), 740–747 (2007).
[18] W. Li, Y. Zhu, K. Feng, and K. Zhang, "Effect of surface grooves on the characteristics of noncontact transportation using near-field acoustic levitation," Tribol. Trans. **61**(5), 960–971 (2018).
[19] D. Koyama, K. Nakamura, and S. Ueha, "A stator for a self-running, ultrasonically-levitated sliding stage," IEEE Trans. Ultrason. Ferroelectr. Freq. Control **54**(11), 2337–2343 (2007).
[20] J. Hu, G. Li, H. Chan, and C. Choy, "A standing wave-type noncontact linear ultrasonic motor," IEEE Trans. Ultrason. Ferroelectr. Freq. Control **48**(3), 699–708 (2001).
[21] J. Hu, K. Cha, and K. Lim, "New type of linear ultrasonic actuator based on a plate-shaped vibrator with triangular grooves," IEEE Trans. Ultrason. Ferroelectr. Freq. Control **51**(10), 1206–1208 (2004).
[22] B. Wei, R. Shaham, and I. Bucher, "Theoretical investigation and prototype design for non-parallel squeeze film movement platform driven by standing waves," Tribol. Int. **119**, 539–548 (2018).
[23] K. Chen, S. Gao, Y. Pan, and P. Guo, "Self-running and self-floating two-dimensional actuator using near-field acoustic levitation," Appl. Phys. Lett. **109**(12), 123503 (2016).
[24] K. Aono, M. Aoyagi, H. Kajiwara, H. Tamura, and T. Takano, "Increase of holding force in near-field acoustic levitation of tabular object inserted between opposing vibration sources," J. Appl. Phys. **58**, SGGD11 (2019).
[25] Y. Liu, M. Shi, K. Feng, K. Sepahvand, and S. Marburg, "Stabilizing near-field acoustic levitation: Investigation of non-linear restoring force generated by asymmetric gas squeeze film," J. Acoust. Soc. Am. **148**(3), 1468–1477 (2020).
[26] H. Li, Q. Quan, Z. Deng, Y. Hua, Y. Wang, and D. Bai, "A novel noncontact ultrasonic levitating bearing excited by piezoelectric ceramics," Appl. Sci. **6**(10), 280 (2016).
[27] Y. Hashimoto, Y. Koike, and S. Ueha, "Acoustic levitation of planar objects using a longitudinal vibration mode," J. Acoust. Soc. Jpn. E **16**(3), 189–192 (1995).
[28] S. Zhao, S. Mojrzisch, and J. Wallaschek, "An ultrasonic levitation journal bearing able to control spindle center position," Mech. Syst. Signal. Proc. **36**(1), 168–181 (2013).
[29] Y. Liu, X. Sun, K. Sepahvand, and S. Marburg, "Theoretical analysis on the static and dynamic performances of a squeeze film air journal bearing with three separate pads structure," Int. J. Mech. Sci. **200**, 106442 (2021).
[30] F. A. Morrison, *An Introduction to Fluid Mechanics* (Cambridge University Press, New York, 2013), Chap. 5, pp. 369–379.
[31] T. Stolarski, "Running characteristics of aerodynamic bearing with self-lifting capability at low rotational speed," Adv. Tribol. **2011**, 973740 (2011).
[32] T. Stolarski and W. Chai, "Self-levitating sliding air contact," Int. J. Mech. Sci. **48**(6), 601–620 (2006).
[33] K. Czolczynski, *Rotordynamics of Gas-Lubricated Journal Bearing Systems* (Springer, New York, 2012). Chap. 1, pp. 11–14.
[34] S. Ueha, Y. Hashimoto, and Y. Koike, "Non-contact transportation using near-field acoustic levitation," Ultrasonics **38**(1), 26–32 (2000).
[35] S. Chen, H. Chou, and Y. Kang, "Stability analysis of hydrodynamic bearing with herringbone grooved sleeve," Tribol. Int. **55**, 15–28 (2012).
[36] K. Feng, Z. Huang, and Z. Guo, "Design of spherical spiral groove bearings for a high-speed air lubricated gyroscope," Tribol. Trans. **58**(6), 1084–1095 (2015).
[37] H. Heshmat, J. Walowit, and O. Pinkus, "Analysis of gas-lubricated foil journal bearings," ASME J. Lubr. Technol. **105**(4), 647–655 (1983).
[38] W. Li, Y. Liu, and K. Feng, "Modelling and experimental study on the influence of surface grooves on near-field acoustic levitation," Tribol. Int. **116**, 138–146 (2017).
[39] K. Feng, M. Shi, T. Gong, Y. Liu, and J. Zhu, "A novel squeeze-film air bearing with flexure pivot-tilting pads: Numerical analysis and measurement," Int. J. Mech. Sci. **134**, 41–50 (2017).
[40] E. Matsuo, Y. Koike, K. Nakamura, S. Ueha, and Y. Hashimoto, "Holding characteristics of planar objects suspended by near-field acoustic levitation," Ultrasonics **38**(1–8), 60–63 (2000).